Final Report

Control of Molecular Architecture in the Synthesis of Novel Biodegradable Polyesters for Use in Biomedical Applications

By Assistant Professor Dr. Winita Punyodom

October/ 2014 (30)

Contract No. MRG4780109

Final Report

Control of Molecular Architecture in the Synthesis of Novel Biodegradable Polyesters for Use in Biomedical Applications

Researchers

1. **Assistant Professor Dr. Winita Punyodom**
   Chiang Mai University
2. **Associate Professor Dr. Taweechai Amornsakchai**
   Mahidol University
3. **Dr. Robert Molloy**
   Chiang Mai University

This project granted by the Thailand Research Fund

Abstract

Project Code : MRG4780109

Project Title: Control of Molecular Architecture in the Synthesis of Novel Biodegradable Polyesters for Use in Biomedical Applications

Investigator : Assistant Professor Dr. Winita Punyodom

E-mail Address : winitacmu@gmail.com

Project Period : 1 July 2004 – 30 Oct 2014

Abstract:

In this research, the novel pentaerythritol tetrakis(6′-hydroxyhexanoate), as a star-core macroinitiator was prepared by using ε-caprolactone (CL) caped with the hydroxyl groups of pentaerythritol (PTOL) in the ratio of 4:1, resulting in a colorless oil and moderate yield (43% in overall steps) of the final product. The chemical structure of star-core macroinitiator was identified by IR, NMR and ESI-mass spectroscopy. The well-defined star-shaped poly(ε-caprolactone), PCL could be synthesized using a 4-arm star-core macroinitiator via the ring-opening polymerization (ROP) of CL in bulk using stannous octoate as catalyst. The effects of differing molecular architectures on the polymer properties of linear and star-shaped PCLs are being investigated. Low molecular weight PCLs (PCL_hexanol, PCL_PTOL and PCL_macroinitiator) were synthesized and characterized to confirm their molecular architectures. The ^{1}H-NMR showed that the average number of OH groups initiating polymerization, as calculated from the average degree of the polymerization per arm (DP_n/arm), was close to the actual OH functionalities. The star-shaped PCLs had lower melting temperatures, degrees of crystallinity and decomposition temperatures than the linear PCL. This could be attributed to their shorter chain lengths and greater number of free chain ends which disrupts the orderly folded chain pattern in the crystal. This offers the possibility of being able to adjust the crystallinity by varying the shape of the polymer molecules, thus providing a useful means of controlling polymer properties and can be utilized and optimized for each application. Structure-property studies of

high molecular weight PCLs have shown that the molecular architecture can have effects on the mechanical and rheological properties and *in vitro* hydrolytic biodegradation. In conclusion, the problem of the insolubility of PTOL in CL monomer and steric hindrance could be overcome by using the novel star-core macroinitiator leading to the synthesis of star-shaped PCLs with interesting properties which were different to linear PCL.

Keywords : Star-core macroinitiator, novel pentaerythritol tetrakis(6′-hydroxyhexanoate), star-shaped poly(ε-caprolactone), mechanical and rheological properties, *in vitro* hydrolytic degradation

บทคัดย่อ

ในงานวิจัยนี้ เพนทะอีรีทรีทอลเตตระคีซ(6'-ไฮดรอกซีเฮกซะโนเอท) ตัวริเริ่มชนิดแมกโครที่มีแกนเป็นรูปดาวตัวใหม่ ถูกเตรียมขึ้นโดยใช้เอปไซลอน-คาโพรแลคโทนจับกับหมู่ไฮดรอกซิลของเพนทะอีรีทรีทอล (พีทีโอแอล) ในอัตราส่วนสี่ต่อหนึ่ง ได้ผลิตภัณฑ์สุดท้ายเป็นของเหลวหนืดไม่มีสี เปอร์เซ็นต์ผลผลิตปานกลางประมาณ 43 เปอร์เซ็นต์จากขั้นตอนการสังเคราะห์ทั้งหมด สามารถพิสูจน์โครงสร้างทางเคมีของตัวเริ่มชนิดแมกโครที่มีแกนรูปดาวได้โดยไออาร์ เอ็นเอ็มอาร์ และอีเอสไอ-แมสสเปกโทรสโกปี สารประกอบที่ได้ถูกนำไปใช้สังเคราะห์พอลิเอปไซลอน-คาโพรแลคโทน (พีซีแอล) รูปร่างแบบดาว ผ่านปฏิกิริยาการพอลิเมอไรเซชันแบบเปิดวงในบัลค์โดยใช้สแตนนัส ออกโทเอทเป็นตัวเร่งปฏิกิริยา หลังจากนั้นได้ทำการศึกษาผลของโครงสร้างโมเลกุลที่แตกต่างกันที่มีต่อสมบัติของพีซีแอลที่มีรูปร่างเป็นโซ่ตรงและรูปดาว พีซีแอลน้ำหนักโมเลกุลต่ำที่มีโครงสร้างแตกต่างกันได้ถูกสังเคราะห์และวิเคราะห์ลักษณะเฉพาะเพื่อยืนยันโครงสร้างโมเลกุลจากเทคนิคโปรตอน เอ็นเอ็มอาร์แสดงว่าจำนวนหมู่ไฮดรอกซิลที่ริเริ่มปฏิกิริยาพอลิเมอไรเซชันซึ่งคำนวณจากดีกรีการพอลิเมอไรเซชันเฉลี่ยต่อแขน มีค่าใกล้เคียงกับหมู่ไฮดรอกซิลที่แท้จริง พีซีแอลที่มีโครงสร้างรูปดาวมีค่าอุณหภูมิการหลอมเหลว ดีกรีความเป็นผลึกและอุณหภูมิการสลายตัวต่ำกว่าโครงสร้างแบบโซ่ตรง แสดงให้เห็นว่าสายโซ่ที่สั้นลงและการเพิ่มของจำนวนปลายสายโซ่จะขัดขวางการจัดเรียงตัวของผลึก จึงสามารถปรับความเป็นผลึกโดยการเปลี่ยนแปลงรูปร่างโมเลกุลของพอลิเมอร์ได้ ทั้งนี้มีความเป็นไปได้ที่จะปรับความเป็นผลึกโดยการเปลี่ยนรูปร่างโมเลกุลของพอลิเมอร์ ซึ่งจะให้ข้อมูลที่เป็นประโยชน์ในการควบคุมสมบัติของพอลิเมอร์ให้เหมาะสมในการนำไปใช้ประโยชน์ จากการศึกษาความสัมพันธ์ระหว่างโครงสร้างและสมบัติของพีซีแอลที่มีน้ำหนักโมเลกุลสูง แสดงให้เห็นว่าโครงสร้างโมเลกุลมีผลต่อสมบัติเชิงกล สมบัติรีโอโลยี และสมบัติการสลายตัวทางชีวภาพแบบไฮโดรไลติกภายนอกร่างกาย จากผลการศึกษาทั้งหมดสามารถสรุปได้ว่าปัญหาการละลายของพีทีโอแอลในซีแอลมอนอเมอร์และผลของความเกะกะ ทำให้สามารถใช้ตัวริเริ่มชนิดแมกโครที่มีแกนเป็นรูปดาวตัวใหม่เพื่อสังเคราะห์พีซีแอลที่มีโครงสร้างรูปดาวที่มีสมบัติที่น่าสนใจแตกต่างจากพีซีแอลที่มีโครงสร้างเป็นโซ่ตรง

Content

1. Abstract

Abstract

In this research, the novel pentaerythritol tetrakis(6′-hydroxyhexanoate), as a star-core macroinitiator was prepared by using ε-caprolactone (CL) caped with the hydroxyl groups of pentaerythritol (PTOL) in the ratio of 4:1, resulting in a colorless oil and moderate yield (43% in overall steps) of the final product. The chemical structure of star-core macroinitiator was identified by IR, NMR and ESI-mass spectroscopy. The well-defined star-shaped poly(ε-caprolactone), PCL could be synthesized using a 4-arm star-core macroinitiator via the ring-opening polymerization (ROP) of CL in bulk using stannous octoate as catalyst. The effects of differing molecular architectures on the polymer properties of linear and star-shaped PCLs are being investigated. Low molecular weight PCLs (PCL_hexanol, PCL_PTOL and PCL_macroinitiator) were synthesized and characterized to confirm their molecular architectures. The ^{1}H-NMR showed that the average number of OH groups initiating polymerization, as calculated from the average degree of the polymerization per arm (DP_n/arm), was close to the actual OH functionalities. The star-shaped PCLs had lower melting temperatures, degrees of crystallinity and decomposition temperatures than the linear PCL. This could be attributed to their shorter chain lengths and greater number of free chain ends which disrupts the orderly folded chain pattern in the crystal. This offers the possibility of being able to adjust the crystallinity by varying the shape of the polymer molecules, thus providing a useful means of controlling polymer properties and can be utilized and optimized for each application. Structure-property studies of high molecular weight PCLs have shown that the molecular architecture can have effects on the mechanical and rheological properties and *in vitro* hydrolytic biodegradation. In conclusion, the problem of the insolubility of PTOL in CL monomer and steric hindrance could be overcome by using the novel star-core macroinitiator leading to the synthesis of star-shaped PCLs with interesting properties which were different to linear PCL.

บทคัดย่อ

ในงานวิจัยนี้ เพนทะอีรีทรีทอลเตตระคีซ(6'-ไฮดรอกซีเฮกซะโนเอท) ตัวริเริ่มชนิดแมกโครที่มีแกนเป็นรูปดาวตัวใหม่ ถูกเตรียมขึ้นโดยใช้เอปไซลอน-คาโพรแลคโทนจับกับหมู่ไฮดรอกซิลของเพนทะอีรีทรีทอล (พีทีโอแอล) ในอัตราส่วนสี่ต่อหนึ่ง ได้ผลิตภัณฑ์สุดท้ายเป็นของเหลวหนืดไม่มีสี เปอร์เซ็นต์ผลผลิตปานกลางประมาณ 43 เปอร์เซ็นต์จากขั้นตอนการสังเคราะห์ทั้งหมด สามารถพิสูจน์โครงสร้างทางเคมีของตัวเริ่มชนิดแมกโครที่มีแกนรูปดาวได้โดยไออาร์ เอ็นเอ็มอาร์ และอีเอสไอ-แมสสเปกโทรสโกปี สารประกอบที่ได้ถูกนำไปใช้สังเคราะห์พอลิเอปไซลอน-คาโพรแลคโทน (พีซีแอล) รูปร่างแบบดาว ผ่านปฏิกิริยาการพอลิเมอไรเซชันแบบเปิดวงในบัลค์โดยใช้สแตนนัส ออกโทเอทเป็นตัวเร่งปฏิกิริยา หลังจากนั้นได้ทำการศึกษาผลของโครงสร้างโมเลกุลที่แตกต่างกันที่มีต่อสมบัติของพีซีแอลที่มีรูปร่างเป็นโซ่ตรงและรูปดาว พีซีแอลน้ำหนักโมเลกุลต่ำที่มีโครงสร้างแตกต่างกันได้ถูกสังเคราะห์และวิเคราะห์ลักษณะเฉพาะเพื่อยืนยันโครงสร้างโมเลกุลจากเทคนิคโปรตอน เอ็นเอ็มอาร์แสดงว่าจำนวนหมู่ไฮดรอกซิลที่ริเริ่มปฏิกิริยาพอลิเมอไรเซชันซึ่งคำนวณจากดีกรีการพอลิเมอไรเซชันเฉลี่ยต่อแขน มีค่าใกล้เคียงกับหมู่ไฮดรอกซิลที่แท้จริง พีซีแอลที่มีโครงสร้างรูปดาวมีค่าอุณหภูมิการหลอมเหลว ดีกรีความเป็นผลึกและอุณหภูมิการสลายตัวต่ำกว่าโครงสร้างแบบโซ่ตรง แสดงให้เห็นว่าสายโซ่ที่สั้นลงและการเพิ่มของจำนวนปลายสายโซ่จะขัดขวางการจัดเรียงตัวของผลึก จึงสามารถปรับความเป็นผลึกโดยการเปลี่ยนแปลงรูปร่างโมเลกุลของพอลิเมอร์ได้ ทั้งนี้มีความเป็นไปได้ที่จะปรับความเป็นผลึกโดยการเปลี่ยนรูปร่างโมเลกุลของพอลิเมอร์ ซึ่งจะให้ข้อมูลที่เป็นประโยชน์ในการควบคุมสมบัติของพอลิเมอร์ให้เหมาะสมในการนำไปใช้ประโยชน์ จากการศึกษาความสัมพันธ์ระหว่างโครงสร้างและสมบัติของพีซีแอลที่มีน้ำหนักโมเลกุลสูง แสดงให้เห็นว่าโครงสร้างโมเลกุลมีผลต่อสมบัติเชิงกล สมบัติรีโอโลยี และสมบัติการสลายตัวทางชีวภาพแบบไฮโดรไลติกภายนอกร่างกาย จากผลการศึกษาทั้งหมดสามารถสรุปได้ว่าปัญหาการละลายของพีทีโอแอลในซีแอลมอนอเมอร์และผลของความเกะกะ ทำให้สามารถใช้ตัวริเริ่มชนิดแมกโครที่มีแกนเป็นรูปดาวตัวใหม่เพื่อสังเคราะห์พีซีแอลที่มีโครงสร้างรูปดาวที่มีสมบัติที่น่าสนใจแตกต่างจากพีซีแอลที่มีโครงสร้างเป็นโซ่ตรง

2. Executive summary

The main aim of this study is concerned with the synthesis of novel biodegradable polymers and the effect of molecular structure on the polymer properties by controlled molecular architectures. The aliphatic polyesters of particular interest are homopolymers (poly(*ε*-caprolactone), PCL and poly(L-lactide), PLL) and copolymer (poly(L-lactide-*co*-caprolactone-*co*-glycolide), PLCG). Special attention has been paid to indicate their biomedical applications.

Two parts of this work including

1. To synthesize star-shaped biodegradable polymers using a novel pentaerythritol tetrakis(6'-hydroxyhexanoate) star-core macroinitiator *via* the ring-opening polymerization (ROP) of *ε*-caprolactone (CL). The effects of different molecular architecture on the thermal, morphological, rheological properties and *in vitro* hydrolytic degradation studies of high molecular weight linear and star-shaped polyesters are investigated.
2. To synthesize high molecular weight poly(L-lactide-*co*-caprolactone-*co*-glycolide), PLCG 75:20:5 mol% with different molecular architectures using 1-hexanol, 2,2-dimethyl-1,3-propanediol (DMP), 1,1,1-tris(hydroxymethyl)propane (TMP) and pentaerythritol (PTOL) as initiators and stannous octoate ($SnOct_2$) as catalyst *via* ROP. The effect of molecular architectures on the thermal, morphological, mechanical, rheological and properties and *in vitro* hydrolytic degradation properties are investigated.

On the basis of all of these results, it was concluded that the polymer properties can be effectively controlled by varying the molecular architecture to suit a different applications.

The knowledge that we have learned from this research work under supported by TRF has helped us to continue the basic science and applications in *"Biodegradable polymer for use in biomedical and bioplastic industries"*. During the past 5 years, I have produced 25 papers published in peer-reviewed international journals; 4 Thai patents; 1 US patent; obtained 25 principal investigator research grants with a total budget of more than 1 million USD; initiated 6 joint projects with industry; and completed 6 Ph.D. and 15 M.S. student research projects. I am currently supervising a research group of 15 including 5 PhDs. The TRF and CHE grant has given a great opportunity to young researchers and also graduate students in Thailand.

3. Objective

The main aim of this research project is concerned with the synthesis of a novel pentaerythritol tetrakis(6′-hydroxyhexanoate) star-core macroinitiator as initiator for use in the ROP of cyclic esters and studies the polymer properties with different molecular architectures. The structure of the polymer will be controlled by using different number of hydroxyl end group of initiators. 1-Hexanol yields linear polymer, while PTOL and pentaerythritol tetrakis(6′-hydroxyhexanoate) give star-shaped polymers. The structures of initiators used in this research are shown below.

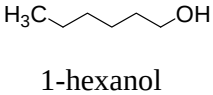

1-hexanol

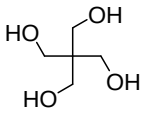

PTOL

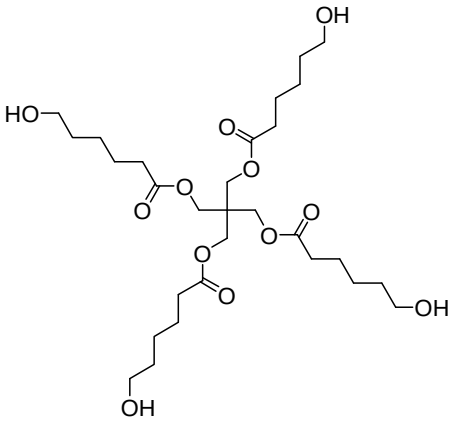

pentaerythritol tetrakis(6'-hydroxyhexanoate)

The detail of this study as follow:

1. To synthesize pentaerythritol tetrakis(6'-hydroxyhexanoate), as a novel star- core macroinitiator for use in the ROP of cyclic esters. This star-core macroinitiator is to be prepared by using CL to cap the OH groups of PTOL as shown below.

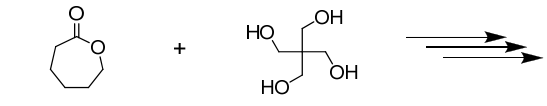

ε-caprolactone PTOL

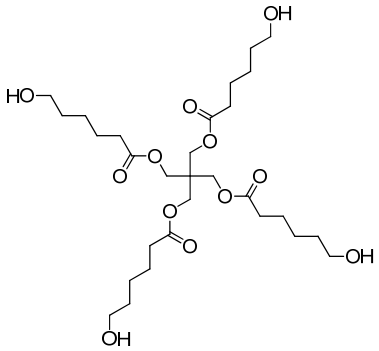

pentaerythritol tetrakis(6'-hydroxyhexanoate)

2. To synthesized low molecular weight polyesters using 1-hexanol, PTOL and novel star-core macroinitiator as initiators and $SnOct_2$ as catalyst *via* ROP in bulk. The low molecular weight polyesters were characterized and confirmed their microstructures.

3. To synthesized high molecular weight polyesters using 1-hexanol, PTOL and novel star-core macroinitiator as initiators and $SnOct_2$ as catalyst *via* ROP in bulk. The effects of different molecular architecture on the thermal, morphological, rheological properties and *in vitro* hydrolytic degradation studies of high molecular weight linear and star-shaped polyesters will be investigated.

4. Research Methodology

4.1 Chemicals, Apparatus and Instruments

4.1.1 Chemicals

The chemicals used in this research project were as listed in Table 4.1.

Table 4.1 Chemicals used in this research project.

CHEMICAL	USAGE	GRADE	SUPPLIER
1. Acetone*	Solvent	Commercial	BDH Chemicals
2. Ammonium chloride	Adjust pH	99.8%	Scharlau
3. Antimony trioxide	Catalyst	99%	BDH
4. Calcium hydride	Drying agent	≥ 97.0%	Fluka
5. ε-Caprolactone**	Monomer	99%	Acros organics
6. Chloroform	Solvent	AR	Lab Scan
7. Chloroform-d_1	Solvent	≥ 99.8%	Wilmad
8. Dichloromethane*	Solvent	Commercial	BDH Chemicals
9. *N,N'*-Dicyclohexylcarbo-Diimide	Reagent	≥ 99.0%	Fluka
10. Diethylamine**	Catalyst Precursor	99.5 %	PS, Panreac Fluka
11. 3,4-Dihydro-2*H*-pyran	Reagent	97%	CarloErba
12. *N,N'*-Dimethyl formamide**	Solvent	99.8%	ICI
13. Ethyl acetate*	Solvent	Commercial	
14. 1-Hexanol	Initiator	GC	Merck
15. Hydrochloric acid	Adjust pH	37%	BDH
16. L(+)-Lactic acid	Monomer Precursor	88%	CarloErba
17. Magnesium sulphate	Drying agent	≥ 98.0%	Fluka
18. Methanol*	Solvent	Commercial	BDH Chemicals
19. Montmorillonite K10	Catalyst	-	Fluka
20. Pentaerythritol	Initiator	Purum, HPLC	Fluka
21. Silica gel 60, GE0030	Stationary phase	-	Scharlau
22. Silica gel 60 PF_{254}	Stationary phase	-	Merck
23. Silicone oil	Heating bath	Commercial	Fluka
24. Stannous octoate**	Catalyst	95%	Sigma
25. Sulfuric acid	Catalyst	96.0%	CarloErba
26. Tetrahydrofuran	Solvent	≥ 99.5%	Merck
27. *p*-Toluene sulfonic acid	Catalyst	98.0%	Sigma

Note * Purified by simple distillation
** Purified by distilled under reduce pressure

4.1.2 Apparatus and Instruments

The main items of apparatus and instruments used were as listed in Table 4.2.

Table 4.2 Apparatus and instruments used in this research project.

APPARATUS AND INSTRUMENTS	COMPANY	MODEL
1. Automatic Viscosity Measuring System	Schott-Geräte	AVS 300
2. Controlled Atmosphere Glove Box	Labconco	50004
3. Differential Scanning Calorimeter (DSC)	Perkin-Elmer	DSC7
4. Gel Permeation Chromatograph (GPC)	Waters	717 Plus
5. High Vacuum Pump	Edwards	Edwards 18
6. Infrared Spectrometer (FT-IR)	Bruker	Tensor 27
7. High Resolution Mass Spectrometer (HR-MS)	Waters	Micromass-Q-Tof-2^{Tm}
8. Mechanical Testing Machine	Lloyd Instruments	LRX+
9. Nuclear Magnetic Resonance Spectrometer (NMR)	Bruker	Avace 400
10. Rotational Rheometer	Malvern	Bohlin Germini HR^{nano}
11. Rotary Evaporator	Büchi	R-200
12. Thermogravimetric Analyzer (TGA)	Perkin-Elmer	TGA7
13. UV-Lamp 254	-	-
14. Vacuum Oven	Eyela	VOS-300SD
15. Weight Balances (2 and 4 positions)	Mettler Toledo	PG802-S and AB204-S

4.2 Monomer Preparation and Purification

The cyclic ester monomers used in this research project were L-lactide (LL) and ε-caprolactone (CL). Since LL is prohibitively expensive to buy (4,320 baht/25g), it was synthesized in our laboratory from its much cheaper than precursor, L-lactic acid. ε-Caprolactone is more readily available and is purchased for use in this research project. The methods of synthesis and purification are described in the following sections 4.2.1 and 4.2.2. The purity of monomers has an important influence on its subsequent polymerizability.

4.2.1 Synthesis of L-Lactide

The synthesis of LL is a two-step reaction involving, firstly the linear polycondensation of L-lactic acid to low molecular weight poly(L-lactic acid) (PLLA) followed, secondly by thermal decomposition of the PLLA to yield LL as the primary decomposition product, as shown in Figure 4.1.

In a typical synthesis reaction in this experiment, approximately 1000 g of L-lactic acid were added into a 1000 ml round-bottomed flask which contained about 1.0 g of tin(II) *n*-butoxide ($Sn(O\textit{n}Bu)_2$) as catalyst (0.1% by weight) [1]. The flask was then heated at 180-200°C (using heating mantle and vary AC scale 120) in an air condenser connected with short path distillation apparatus as shown in Figure 4.2.

Heating and stirring were continued until the water ceased to distill from the reaction flask under atmosphere for about 3 hours. Then, heated at 120-130°C (using heating mantle and vary AC scale 270) before a gentle vacuum (about 4-5 mmHg) was applied to the system for 2 hours to facilitate further removal of water and to increase the polymer molecular weight. The product at this stage was low molecular weight PLLA.

Finally, for an additional period of about 2 hours, the reaction temperature was heated about 220-240°C (using heating mantle and vary AC scale 270) under reduced pressure of about 4-5 mmHg in order to thermally degrade the low molecular weight PLLA to yield LL as a primary product. Crude LL began to distill out of the flask to a receiving flask as light yellow crystalline solid. This crude product was obtained in approximately 99% yield.

Step 1:

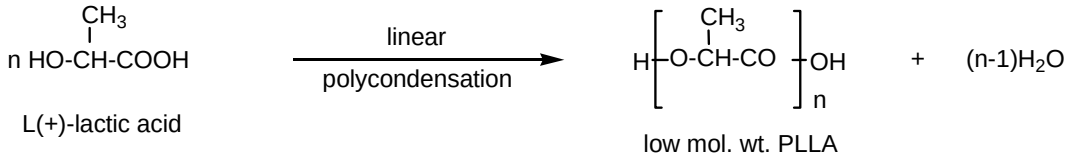

Step 2:

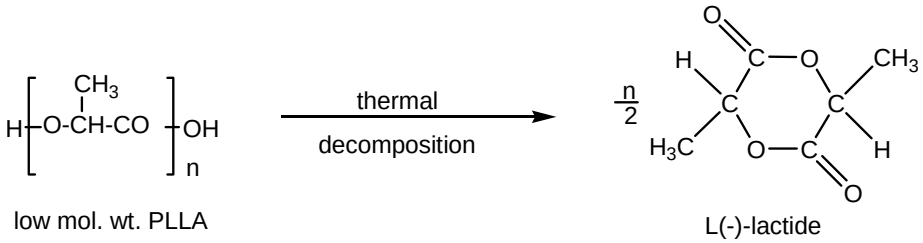

Figure 4.1 Two-step process used for synthesizing LL from L(+)-lactic acid.

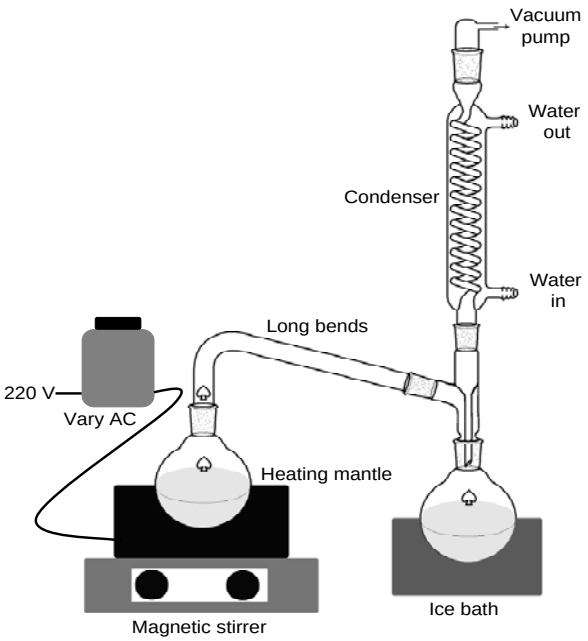

Figure 4.2 The apparatus used in the synthesis of LL [1].

4.2.2 Purification and Purity Analysis of L-Lactide

The crude LL was purified by recrystallisation three times from distilled ethyl acetate. The purified LL was filtered through sintered glass porosity no.4, washed several times with cold ethyl acetate and dried to constant weight at 55°C in a vacuum oven (about 3 mmHg). The purified LL was obtained as a white needle-like solid with approximately 60-70% yield.

Purity analysis by differential scanning calorimetry (DSC) showed that the purified LL had a sharp DSC melting peak from 91 to 92ºC, as shown in Figure 4.3. In order to determine the actual purity of the recrystallized LL by the DSC technique, the instrument's Purity Analysis Software Program was employed [2]. To obtain the best results from purity analysis, a slow scanning rate of 2ºC/min and a small sample size in the range of 1-3 mg were used. From its DSC

melting peak, a purity of 99.95% was obtained. These results served to show that the LL synthesized and purified in this work was of a sufficiently high purity (> 99.9%) to produce high molecular weight polymers. Impurities such as moisture, L-lactic acid and L-lactoyl lactate can act either as initiators or chain terminators during ROP leading to a decrease in the molecular weight of the final product.

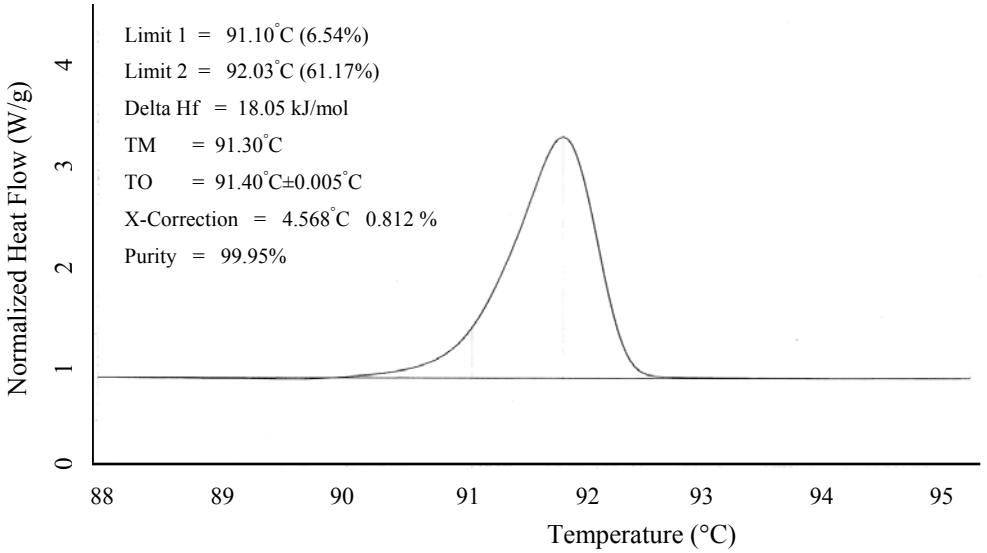

Figure 4.3 DSC melting peak of synthesized LL (after 3rd recrystallisation) (sample size = 2.850 mg, heating rate = 2°C/min).

4.2.3 Purification of ε-Caprolactone by Vacuum Distillation

Commercial CL (Acros Organics, assay 99%) was purified by vacuum distillation as shown in Figure 2.4, the constant boiling fraction from 72°C/0.8 torr (cf. boiling point = 80°C/0.75 torr [3]) pressure being collected. Pure ε-caprolactone was obtained as a clear colorless liquid at room temperature and was stored over molecular sieves 4 Å in a refrigerator in a tightly sealed container until required for use in polymerization.

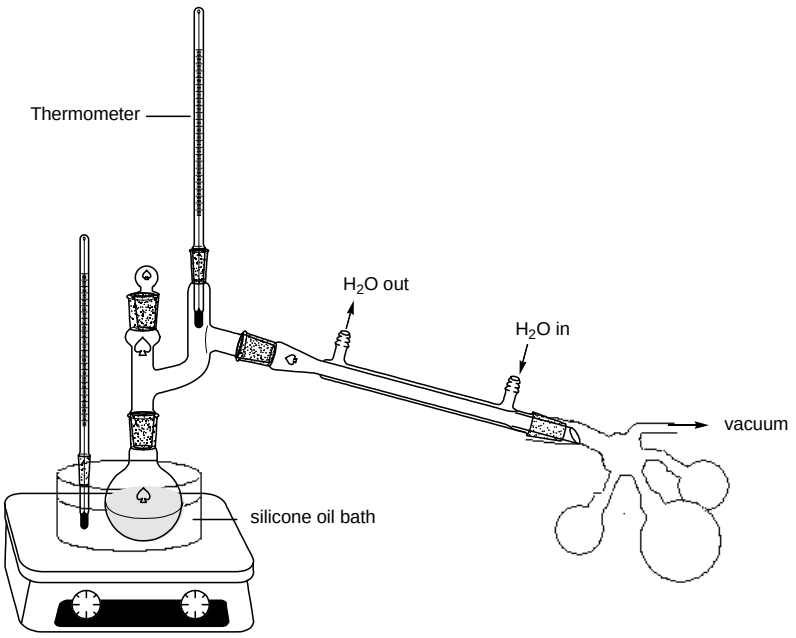

Figure 4.4 Vacuum distillation apparatus used for the purification of ε-caprolactone.

4.3 Catalyst and Initiator Purification

Because trace amounts of water and other impurities could be presented in the catalyst and various initiators used in this research project, they required further purification. Since moisture can have a serious effect on the polymer molecular weight obtained. In general, the method used was followed from references with appropriate drying agent employed.

4.3.1 Stannous Octoate

Commercial stannous octoate, $SnOct_2$ typically 95% pure as received, commonly contains 2-ethylhexanoic acid and water as impurities. $SnOct_2$ used in this research project was purified by bulb-to-bulb vacuum distillations. The first is the distillation under vacuum at room temperature for removing residual water, and then distilled under vacuum at 120-126°C/15 torr for removing 2-ethyl hexanoic acid (cf. 2-ethyl hexanoic acid boiling point = 140°C/23 torr [4]). Purified $SnOct_2$ remaining in the heating flask was obtained as a colorless viscous liquid and was stored in vacuum desiccator.

4.3.2 1-Hexanol

1-Hexanol, monofunctional hydroxyl initiator used for the preparation of linear polymers was purified by vacuum distillation. The distilled 1-hexanol was collected as the constant boiling fraction at 47ºC/4.0 torr (cf. boiling point = 156ºC/1.0 torr [4]) and then stored over molecular sieves 4 Å in vacuum desiccator.

4.3.3 Pentaerythritol

Pentaerythritol, PTOL multifunctional initiator was dried to constant weight in a vacuum oven at 120ºC to remove any residual moisture traces. It was stored in a vacuum desiccator at room temperature. The melting peak of purified PTOL from DSC is 252-260ºC.

4.4 Characterization Methods

In this research project, the monomer, initiators, catalyst and polymer products obtained were characterized by the following combination of instrumental methods.

4.4.1 Fourier Transform Infrared Spectroscopy (FT-IR)

Fourier transform infrared (FT-IR) spectroscopy is the most extensively used method for the analysis of functional groups. In this research project, FT-IR was used, mainly for the structural characterization of the catalyst. A Bruker Fourier transform Infrared Spectrometer was used for the recording of FT-IR spectra with the range 400-4000 cm^{-1}. The samples were prepared in the form of neat liquid on a sodium chloride plate.

4.4.2 High Resolution Mass Spectroscopy (HR-MS)

In this research project, high resolution mass spectroscopy (HR-MS) was used for the structural identification of star-core macroinitiator. The samples were analyzed on micromass Q-Tof-2^{Tm} (Waters) spectrometer**.** The GC was equipped with a 19091S-433 capillary column. Nitrogen was used as carrier gas. The samples were analyzed utilizing the following temperature program of the column: the temperature was allowed to rise from 100 to 250ºC at a heating rate of 10ºC min^{-1} and then held at 250ºC for 25 minutes.

4.4.3 Nuclear Magnetic Resonance Spectroscopy (NMR)

Nuclear magnetic resonance (^{1}H-NMR and ^{13}C-NMR) spectroscopy was used to analyze the chemical structures and number-average molecular weight ($\overline{M}_n$) and microstructure of the polymer formed in this research project. For NMR measurement, the samples were dissolved in deuterated-

chloroform ($CDCl_3$) in 5 mm NMR tubes. The sample concentration was about 5% by weight. Chemical shifts were relative to tetramethylsilane (TMS) (internal standard at $\delta = 0$ ppm). Both ^{1}H-NMR and ^{13}C-NMR spectra were obtained from MestRe-C data processing software and recorded on a Bruker Avace spectrometer working at 400 MHz ^{1}H and 100 MHz ^{13}C respectively.

4.4.4 Gel Permeation Chromatography (GPC)

Molecular weight ($\overline{M}_n$, $\overline{M}_w$ and $\overline{M}_v$) and polydispersities ($\overline{M}_w/\overline{M}_n$) were determined by gel permeation chromatography (GPC). The Waters associated system equipped with a Waters 717 plus autosampler injector, a Waters 515 HPLC solvent pump with styragel HR 4E, 5E column (pore size; 5 μm) connected a Waters 2414 Refractive Index and Viscotex 270 Dual detectors at 40ºC and a TriSEC Version 3.00 as data processing software was used. Narrow polydispersities polystyrene standards were used for calibration, range 1,100-186,000 g mol^{-1}. Tetrahydrofuran (THF) was used as the eluent at the flow rate of 1 ml min^{-1}. The samples were dissolved in THF at a concentration of 3-5% (w/v).

4.4.5 Differential Scanning Calorimetry (DSC)

The purities, temperature transitions (T_g, T_c and T_m) and morphology (% crystallinity) were investigated by differential scanning calorimetry (DSC). DSC measurement was made on a Perkin-Elmer DSC7 instrument with Pyris software. Pure indium and tin were used as reference material to calibrate the temperature. The thermal properties measurements were run from 0ºC to 200ºC at a heating rate of 10ºC min^{-1}. The samples with a typical mass of 3-5 mg were encapsulated in sealed aluminium pans and were heated and cooled under nitrogen atmosphere.

4.4.6 Thermogravimetric Analysis (TGA)

Thermogravimetry (TG) was used as a method for the investigation of the thermal stability and decomposition profile of a polymer. TG analysis was carried out on a Perkin-Elmer Pyris instrument with a TGA7 model. Nitrogen gas was used as the purge gas at pressure of 30 Ibs in^{-2} for the sample zone and 50 Ibs in^{-2} for the balance zone. The heating rate used was 20ºC min^{-1} and the sample was heat from 50ºC to 600ºC with initial sample weights in the range of 5-10 mg. Data was recorded as a thermogram of % weight versus temperature.

4.4.7 Dilute-Solution Viscometry

The intrinsic viscosity, [η] and viscosity average molecular weight ($\overline{M}_v$) of the polymers were determined from dilute solution viscometry. The viscosities were measured at concentration of 0-1.0% (m/v) in solvent with Schott-Geräte Ubbelohde type viscometer (type No. 532 00, capillary No. 0_c) in conjunction with Schott-Geräte AVS300 Automatic Viscosity Measuring System. The results were plotted between reduced and inherent viscosity versus concentration and the viscosity-average molecular weight were calculated from intrinsic viscosity and constant as the Mark-Houwink Sakurada Equation.

4.4.8 Mechanical Tensile Testing

The mechanical tests perform on Lloyds LRX+ Universal Mechanical Testing Machine were used for determining the mechanical properties such as tensile strength, % elongation at break, and Young's modulus. Thin film samples were prepared by a simple solvent casting method. The polymer was dissolved in ethyl acetate to form solutions with concentrations of 20% (w/v). The solution was spread over a glass mold (10 cm × 15 cm). The solvent was evaporated slowly in air at room temperature over three days and the obtained films were further dried under vacuum at room temperature for 48 hours. Each film was cut into 1.0 cm widths and 15.0 cm lengths and kept in a vacuum desiccator until use. The test conditions were followed as ASTM D882-91 with a

sample grips, load cell of 100 N (preload = 0.1 N) at a crosshead speed of 10 mm min^{-1}. The tests were required at least five samples from each polymer at 23±2ºC and 50±5% relative humidity.

4.4.9 Melt Rheology Measurements

Rheology is defined as the science of the deformation and flow of matter. In an ideal viscous liquid, the energy of deformation is dissipated in the form of heat and cannot be recovered just by releasing the external forces; whereas, in an ideal solid, the deformation is fully recovered when the stresses are released. Due to the dependence of rheology on the structure and the basic inherent chemistry of the polymers, rheological data can be used effectively to control material parameters like molecular weight, molecular weight distribution, branching, crosslinking and so forth so that the right choice of the polymer to be processed can be made under a given set of processing conditions.

Figure 4.5 Bohlin Gemini HR^{nano} Rotational Rheometer apparatus; (a) parallel plate geometry and (b) the gap between the plates.

Measurements on PCL homopolymer in this study were performed using Bohlin Gemini HR^{nano} Rotational Rheometer, Malvern as shown in Figure 4.5. The diameter of the plates was 25 mm and the gap between the plates was set to 0.5 mm. The rheological behaviors of all samples were analyzed by shear rate range of 0.01 to 100 (1/s) under isothermal condition at 80ºC. The zero shear rate viscosity, $[\eta_0]$ measurements were performed by measuring viscosity as a function of shear rate.

4.5 Synthesis of Pentaerythritol tetrakis(6'-hydroxyhexanoate) Star-Core Macroinitiator

4.5.1 Synthesis of Methyl 6-hydroxyhexanoate (2)

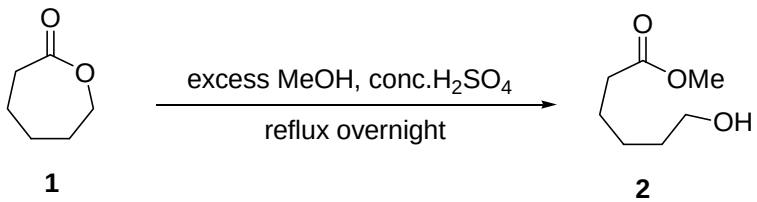

1 **2**

A mixture of ε-caprolactone (**1**) (20.00 g, 0.1752 mol) and conc. sulfuric acid (10 ml) in anhydrous methanol (1600 ml) was heated to reflux overnight. The reaction mixture was quenched with saturated aqueous sodium hydrogen carbonate solution at 0°C and the crude mixture was extracted several times with CH_2Cl_2. The combined organic extracts were washed with H_2O, dried over $MgSO_4$, filtered, and evaporated to dryness.

The crude product was purified by flash column chromatography on silica gel using EtOAc : hexane = 1 : 9 as eluent to give hydroxyl ester **2**, *methyl 6-hydroxyhexanoate* in 79% yield (20.22 g) and 100% conversion from the starting material.

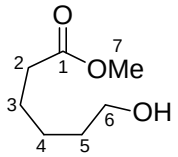

2

Table 4.3 Data of compound **2**.

Physical property	
Colorless oil	
IR spectroscopy (evaporated thin film)	
Frequency (v, cm^{-1})	Type of vibrations
3403 2937, 2865 1732 1436, 1356 1182 1051	O-H stretching of hydroxyl CH_2, CH_3 stretching C=O stretching of ester CH_2, CH_3 bending C-O stretching of ester O-H bending of hydroxyl
NMR spectroscopy	
^{1}H NMR (400 MHz) in $CDCl_3$	
Chemical shift (δ, ppm)	Type of protons
1.41 1.60 1.67 2.34 3.66 3.68	2H, *m*, CH_2-4 2H, *m*, CH_2-3 2H, *m*, CH_2-5 2H, *t* (J = 7.4 Hz), CH_2-2 2H, *t* (J = 6.6 Hz), CH_2-6 3H, *s*, $COOCH_3$-7
^{13}C NMR (100 MHz) in $CDCl_3$	
Chemical shift (δ, ppm)	Type of carbons
24.58 25.24	CH_2-4 CH_2-3

^{13}C NMR (100 MHz) in $CDCl_3$	
Chemical shift (δ, ppm)	Chemical shift (δ, ppm)
32.25	CH_2-5
33.94	CH_2-2
51.49	CH_3-7
62.58	CH_2-6
174.19	C_q-1

4.5.2 Synthesis of Methyl 6-(tetrahydro-2*H*-pyran-2-yloxy)hexanoate (3)

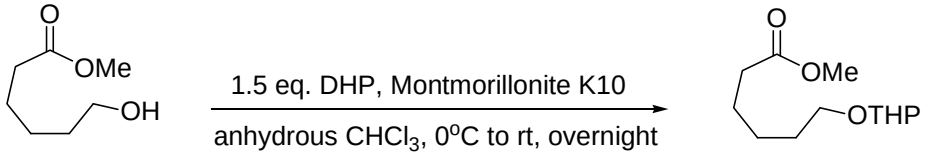

2 **3**

Montmorillonite K10 was added into a solution of **2** (20.00 g, 0.1369 mol), in anhydrous chloroform (500 ml) followed by 3,4-dihydro-2*H*-pyran (DHP) (17.27 g, 0.2054 mol) at 0°C over 15 min. The reaction mixture was stirred at room temperature overnight and then passed through Celite 545, washed with CH_2Cl_2. The organic phase was evaporated to dryness.

The crude product was purified by flash column chromatography on silica gel using EtOAc : hexane = 1 : 9 as eluent to give the protected hydroxyl ester **3**, *methyl 6-(tetrahydro-2H-pyran-2-yloxy)hexanoate* in 92% yield (22.68 g) and 72% conversion from starting material.

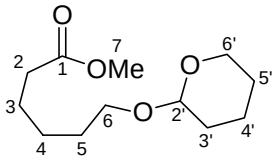

3

Table 4.4 Data of compound **3**.

Physical property	
Colorless oil	
IR spectroscopy (evaporated thin film)	
Frequency (ν, cm^{-1})	Type of vibrations
2945, 2871	CH_2, CH_3 stretching
1735	C=O stretching of ester
1445, 1356	CH_2, CH_3 bending
1167	C-O stretching of ester
1074, 1035	C-O stretching of ether

NMR spectroscopy	
^{1}H-NMR (400 MHz) in $CDCl_3$	
Chemical shift (δ, ppm)	Type of protons
1.36-1.48 1.48-1.91 2.34 3.41 3.76 3.52, 3.88 3.69	2H, *m*, CH_2-4 10H, *m*, CH_2-3, 5, 3', 4', 5' 2H, *t* (J = 7.47 Hz), CH_2-2 1H, *dt* (J = 9.61, 6.53 Hz), CH_2-6' 1H, *dt* (J = 9.61, 6.73 Hz), CH_2-6' 2H, *m*, CH_2-6 3H, *s*, $COOCH_3$-7
^{1}H-NMR (400 MHz) in $CDCl_3$	
Chemical shift (δ, ppm)	Chemical shift (δ, ppm)
4.59	1H, *dd* (J = 2.74 Hz), CH-2'
^{13}C-NMR (100 MHz) in $CDCl_3$	
Chemical shift (δ, ppm)	Type of carbons
19.67, 25.84, 29.38 24.78 25.46 30.74 34.02 51.47 62.37 67.32 98.88 174.19	CH_2-3', 4', 5' CH_2-4 CH_2-3 CH_2-5 CH_2-2 CH_3-7 CH_2-6 CH_2-6' CH-2' C_q-1
Mass spectroscopy (HR-MS)	
Molecular weight	m/z
Calc. for $C_{12}H_{22}O_4$ Lock mass of $C_9H_{10}N_4O_2S_2$ Calc. for $C_{12}H_{22}O_4Na$ Found for $C_{12}H_{22}O_4Na$	231.1596 $(M + H)^+$ 293.0143 $(M + Na)^+$ 253.1416 $(M + Na)^+$ 253.1416 $(M + Na)^+$

4.5.3 Synthesis of 6-(Tetrahydro-2*H*-pyran-2-yloxy)hexanoic acid (4)

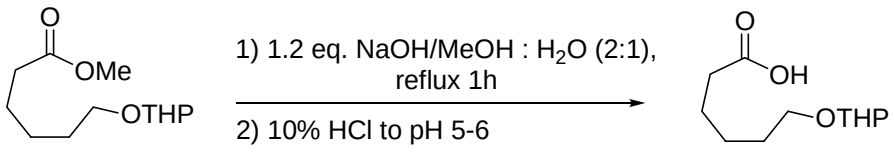

3 **4**

A solution of NaOH (3.13 g, 0.0782 mol) in H_2O (150 ml) was added to a solution of **3** (15.00 g, 0.0652 mol) in MeOH (300 ml) and heated to reflux for 1 h. The mixture was acidified with 10% HCL (pH 5-6) followed by extraction several times with CH_2Cl_2. The organic phase was dried over $MgSO_4$, filtered and evaporated to dryness to give the ether acid **4**, *6-(tetrahydro-2H-pyran-2-yloxy)hexanoic acid* in 75% yield (10.56 g) and 100% conversion from the starting material.

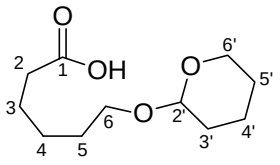

4

Table 4.5 Data of compound **4**.

Physical property	
Colorless oil	
IR spectroscopy (evaporated thin film)	
Frequency (v, cm^{-1})	Type of vibrations
3698-2319 2949, 2875	O-H stretching of hydroxyl CH_2 stretching
IR spectroscopy (evaporated thin film)	
Frequency (v, cm^{-1})	Type of vibrations
1711 1450 1370 1065, 1029	C=O stretching of carboxylic acid CH_2 bending C-O stretching and O-H deformation of carboxylic acid C-O stretching of ether
NMR spectroscopy	
^{1}H-NMR (400 MHz) in $CDCl_3$	
Chemical shift (δ, ppm)	Type of protons
1.39-1.92 2.39 3.41 3.76 3.52, 3.88 4.60	12H, *m*, CH_2-3, 4, 5, 3', 4', 5' 2H, *t* (J = 7.4 Hz), CH_2-2 1H, *dt* (J = 9.6, 6.5 Hz), CH_2-6'$_{ax}$ 1H, *dt* (J = 9.6, 6.7 Hz), CH_2-6'$_{eq}$ 2H, *m*, CH_2-6 1H, *m*, CH-2'
^{13}C-NMR (100 MHz) in $CDCl_3$	
Chemical shift (δ, ppm)	Type of carbons
19.61, 25.74, 29.34	CH_2-3', 4', 5'

24.49 25.43 30.70 33.87 62.33	CH_2-4 CH_2-3 CH_2-5 CH_2-2 CH_2-6
^{13}C-NMR (100 MHz) in $CDCl_3$	
Chemical shift (δ, ppm)	Type of carbons
67.27 98.85 179.22	CH_2-6' CH-2' C_q-1
Mass spectroscopy (HR-MS)	
Molecular weight	m/z
Calc. for $C_{11}H_{20}O_4$	217.1440 $(M + H)^+$
Lock mass of $C_9H_{10}N_4O_2S_2$	293.0143 $(M + Na)^+$
Calc. for $C_{11}H_{20}O_4Na$	239.1259 $(M + Na)^+$
Found for $C_{11}H_{20}O_4Na$	239.1259 $(M + Na)^+$

4.5.4 Synthesis of Pentaerythritol tetrakis(6'-hydroxyhexanoate) (7)

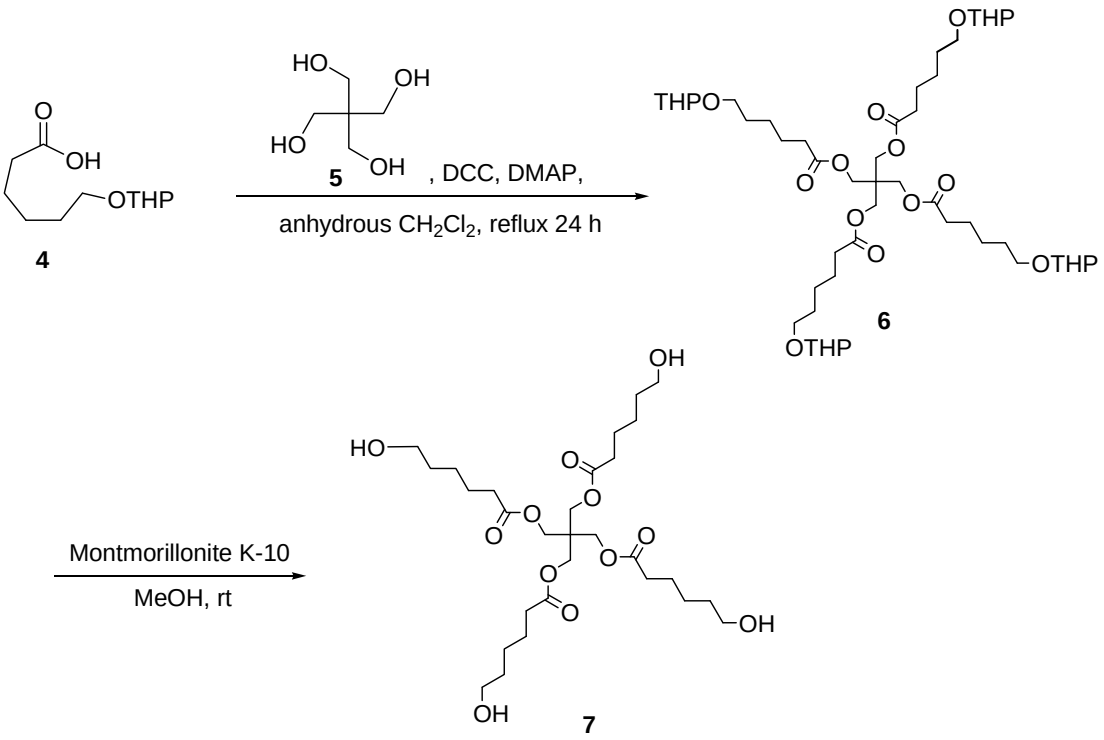

To a 250 ml, three necks, round-bottomed flask equipped with a magnetic stirred with a septum cap and nitrogen inlet was added anhydrous CH_2Cl_2 (100 ml) and dry compound **4** (6.98 g, 0.0323 mol). The mixture was cooled down to 0ºC followed by addition of 4-dimethylaminopyridine (DMAP) (5.83 g, 0.0477 mol) and pentaerythritol (PTOL) (1.00 g, 0.0073 mol in *N,N*-dimethylformamide (DMF)). After stirring at 0ºC for few min, then *N,N'*-

dicyclohexylcarbodiimide (DCC) (9.85 g, 0.0477 mol in anhydrous CH_2Cl_2) was added. The reaction mixture was heated to reflux for 24 h. The crude product was filtrated, washed with CH_2Cl_2 and evaporated to dryness.

The crude product **6**, *pentaerytritol (6-(tetrahydro-2H-pyran-2-yloxy)hexanoate))* and montmorillonite K10 (as a catalyst) in MeOH (100 ml) were stirred at room temperature for 7 h, then filtrated through celite 545 and evaporated to dryness. The crude product was purified by flash column chromatography on silica gel using acetone : EtOAc : hexane = 1 : 1 : 8 as eluent to give the star-core macroinitiator **7**, *pentaerythritol tetrakis(6'-hydroxyhexanoate)* in 43% yield (1.87 g), and 100% conversion from the starting material.

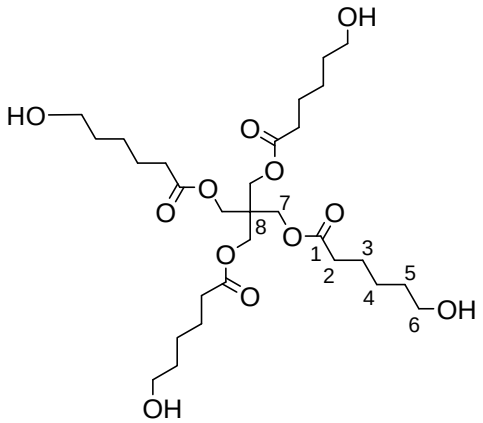

7

Table 4.6 Data of compound **7**.

Physical property	
Colorless oil	
IR spectroscopy (evaporated thin film)	
Frequency (ν, cm^{-1})	Type of vibrations
3381	O-H stretching of hydroxyl
2946, 2871	CH_2 stretching
1747	C=O stretching of ester
1407	CH_2 bending
1153	C-O stretching of ester
1065	O-H bending of hydroxyl
NMR spectroscopy	
^{1}H-NMR (400 MHz) in $CDCl_3$	
Chemical shift (δ, ppm)	Type of protons
1.38	8H, *m*, CH_2-4
1.55	8H, *m*, CH_2-3
1.64	8H, *m*, CH_2-5
2.35	8H, *m*, CH_2-2

3.61 4.10	8H, *t* (*J* = 6.3 Hz), CH_2-6 8H, *s*, CH_2-7
^{13}C-NMR (100 MHz) in $CDCl_3$	
Chemical shift (δ, ppm)	Type of carbons
24.55 25.17 32.09	CH_2-4 CH_2-3 CH_2-5
^{13}C-NMR (100 MHz) in $CDCl_3$	
Chemical shift (δ, ppm)	Type of carbons
34.05 43.56 62.21 77.00 173.30	CH_2-2 C_q-8 CH_2-6 CH_2-7 C_q-1
Mass spectroscopy (HR-MS)	
Molecular weight	m/z
Calc. for $C_{29}H_{52}O_{12}$	593.3537 $(M + H)^+$
Lock mass of $C_{33}H_{40}N_2O_9$	609.2812 $(M + H)^+$
Calc. for $C_{29}H_{52}O_{12}Na$	615.3356 $(M + Na)^+$
Found for $C_{29}H_{52}O_{12}Na$	615.3356 $(M + Na)^+$

4.6 Polymer Synthesis and Purification

All ring-opening polymerization (ROP) were carried out in bulk at 120°C in a round-bottomed flask with ground-glass joints with a magnetic stirring bar. All glassware was dried in a vacuum oven at 120ºC for 12 hours.

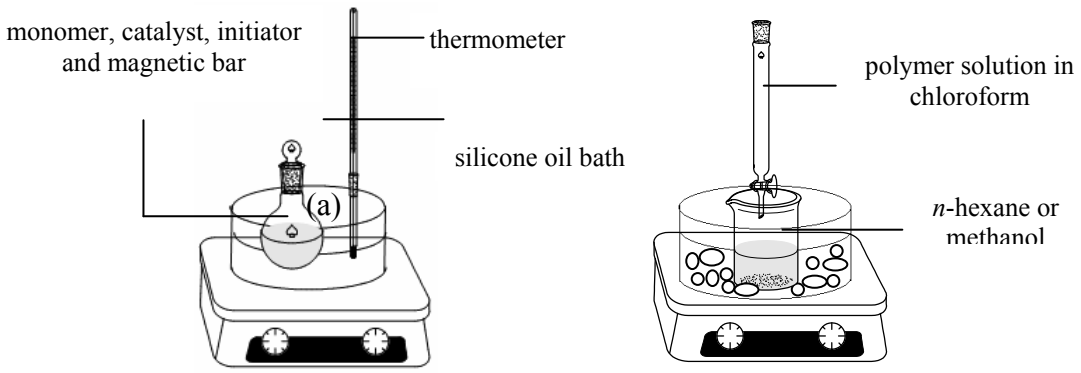

Figure 2.6 Apparatus used in (a) the ring-opening bulk polymerization and (b) polymer purification by re-precipitation from solution.

The catalyst, initiators and monomers were weight and added to the reaction flask under nitrogen in a controlled-atmosphere glove box at room temperature. After removing the flask from the glove box, it was immersed in a silicone oil bath at a constant temperature and for given period of time as shown in Figure 4.6 (a). At the end of the polymerization period, the flask was rapidly cooled at room temperature. The polymers were purified by dissolving in chloroform then re-precipitating in iced-cold *n*-hexane for low molecular weight polymers and in methanol for high molecular weight polymers as shown in Figure 4.6 (b). Then, the purified homopolymer products were dried in a vacuum oven until constant weight.

4.6.1 Synthesis of Low Molecular Weight Poly(*ε*-caprolactone), PCL Model Compounds with Different Molecular Architectures

Linear and star-shaped low molecular weight PCLs were synthesized by ROP at 120°C for 48 hours using 0.1 mole% $SnOct_2$ as a catalyst and 4 mole% 1-hexanol, PTOL and pentaerythritol tetrakis(6'-hydroxyhexanoate) as initiators. The conditions used in the polymerization are shown in Table 4.7. The polymers were purified by dissolving in chloroform then re-precipitating in iced-cold *n*-hexane and drying in a vacuum oven at room temperature until constant weight.

Table 4.7 Polymerization conditions of low molecular weight PCLs with different molecular architectures synthesis at 120°C for 48 hours.

Homopolymer	Initiator	Monomer feed CL (g)	$SnOct_2$: Initiator 0.1 : 4 mole% (g)
PCL_1-hexanol	1-hexanol	2.0062	0.0077 : 0.0710
PCL_PTOL	PTOL	2.0073	0.0087 : 0.0940
PCL_macroinitiator	macroinitiator	2.0100	0.0079 : 0.4989

4.6.2 Synthesis of High Molecular Weight Poly(*ε*-caprolactone), PCL with Different Molecular Architectures

Linear and star-shaped high molecular weight PCLs were synthesized by ROP at 120ºC for 72 hours using 0.1 mole% $SnOct_2$ as a catalyst and 0.05 and 0.005 mole% mono- and multifunctional alcohol (1-hexanol, PTOL and pentaerythritol tetrakis(6'-hydroxyhexanoate)) as initiators respectively. The conditions used in the polymerization are shown in Tables 4.8 and 4.9.

The polymers were purified by dissolving in chloroform then re-precipitating in iced-cold methanol and drying in a vacuum oven at room temperature until constant weight.

Table 4.8 Polymerization conditions for high molecular weight PCLs with different molecular architectures synthesis at 120^{o}C for 72 hours (10 g).

Homopolymer	Initiator	Monomer feed CL (g)	$SnOct_2$: Initiator 0.1 : 0.05 mole% (g)
PCL_1-hexanol	1-hexanol	10.0183	0.0871 : 0.0019
PCL_PTOL	PTOL	10.0443	0.0981 : 0.0021
PCL_macroinitiator	macroinitiator	10.0851	0.0899 : 0.0069

Table 2.9 Polymerization conditions for high molecular weight PCLs with different molecular architectures synthesis at 120ºC for 72 hours (25 g).

Homopolymer	Initiator	Monomer feed CL (g)	$SnOct_2$: Initiator 0.1 : 0.005 mole% (g)
PCL_1-hexanol	1-hexanol	25.0112	0.1391 : 0.0019
PCL_PTOL	PTOL	25.0283	0.1434 : 0.0028
PCL_macroinitiator	macroinitiator	25.0098	0.1429 : 0.0114

4.6.3 Synthesis of High Molecular Weight Poly(L-lactide), PLL with Different Molecular Architectures

Linear and star-shaped high molecular weight PLLs were synthesized by ROP at 120ºC for 48 hours using 1 mole% and for 72 hours using 0.005 mole% mono- and multifunctional alcohol (1-hexanol, PTOL and pentaerythritol tetrakis(6'-hydroxyhexanoate)) as initiators respectively and 0.1 mole% $SnOct_2$ as a catalyst. The conditions used in the polymerization are shown in Tables 4.10-4.11. The polymers were purified by dissolving in chloroform then re-precipitating in iced-cold methanol and drying in a vacuum oven at 55ºC until constant weight.

Table 4.10 Polymerization conditions for low molecular weight PLLs with different molecular architectures synthesis at 120ºC for 48 hours (10 g).

Homopolymer	Initiator	Monomer feed LL (g)	$SnOct_2$: Initiator 0.1 : 1 mole% (g)
PLL_1-hexanol	1-hexanol	10.0686	0.0289 : 0.9674
PLL_PTOL	PTOL	10.0916	0.0293 : 0.9696
PLL_macroinitiator	macroinitiator	10.4113	0.0304 : 1.0004

Table 4.11 Polymerization conditions for high molecular weight PLLs with different molecular architectures synthesis at 120ºC for 72 hours (25 g).

Homopolymer	Initiator	Monomer feed LL (g)	$SnOct_2$: Initiator 0.1 : 0.005 mole% (g)
PLL_1-hexanol	1-hexanol	25.0019	0.1221 : 0.0020
PLL_PTOL	PTOL	25.0103	0.1184 : 0.0025
PLL_macroinitiator	macroinitiator	25.0202	0.1199 : 0.0085

4.7 *In Vitro* Hydrolytic Biodegradation Studies

In vitro experiments were conducted in order to evaluate the potential biodegradability of the high molecular weight PCL and PLL homopolymer with different molecular architectures (PCL_1-hexanol, PCL_PTOL, PCL_macro, PLL_1-hexanol, PLL_PTOL and PLL_macro)

4.7.1 Preparation of Phosphate Buffer Saline (PBS)

The preparation phosphate buffer saline (PBS) followed European Pharmacopoeia [5]. A 0.2 M PBS solution of pH 7.40 was prepared from anhydrous disodium hydrogen orthophosphate (Na_2HPO_4) 2.38 g, potassium dihydrogen phosphate (KH_2PO_4) 0.19 g and sodium chloride (NaCl) 8.00 g dissolved in 1000 ml deionized water. The pH of the solution, which was almost 7.40, was adjusted to exactly 7.40±0.01 with 1 M sodium hydroxide (NaOH).

4.7.2 Preparation of Polymer Samples and Glassware

The PCL and PLL films with different molecular architecture were prepared by solvent casting method using chloroform as solvent (2.4g/30 ml) in mold (12×15 cm^2) and then the solvent allowed to evaporate for 48 hours and further dried under vacuum at room temperature for 48 hours. The films were cut by puncture into circular discs with a diameter 10 mm and thickness 0.15 mm. A total of 216 samples (6 sets) were dried in vacuum oven at 40°C (Figure 4.7) to constant weight and their weight accurately recorded (±0.0001 g). The experiments were divided into 6 sets.

Set 1: PCL_1-hexanol	36	bottles
Set 2: PCL_PTOL	36	bottles
Set 3: PCL_macroinitiator	36	bottles
Set 4: PLL_1-hexanol	36	bottles
Set 5: PLL_PTOL	36	bottles
Set 6: PLL_macroinitiator	36	bottles

All glassware items were sterilized before use by stream autoclaving at 120ºC for 90 minutes. The dried film was then immersed individually in a 50 ml screw-top glass bottles, each containing 10 ml of PBS. The bottles were then immediately placed in an incubator, thermostatically controlled at 37±1ºC, for the *in vitro* hydrolytic biodegradation experiments (zero time). The experiments lasted for a total of 20 weeks.

Figure 4.7 Incubator for *in vitro* hydrolytic degradation studies.

4.7.3 Sampling Procedure

At time intervals (0, 1, 2, 3, 5, 7, 9, 11, 13, 15, 17 and 20 weeks), the bottles were removed from the incubator and samples filtered off by sintered glass (porosity no.3), washed carefully with deionized water and dried to constant weight in vacuum oven at room temperature. Their weights were accurately recorded. Various properties of the samples were then tested, *e.g.* % weight loss, % weight retention and DSC. The pH of the medium was also re-measured since the hydrolytic mechanism of polyester biodegradation is well- known to be pH-dependent.

5. Results and Discussion

5.1 Synthesis of Pentaerythritol tetrakis(6'-hydroxyhexanoate)

The retrosynthetic analysis of compound **7** could be derided from pentarythritol (**5**) and *ε*-caprolactone (**1**) as shown in Scheme 5.1.

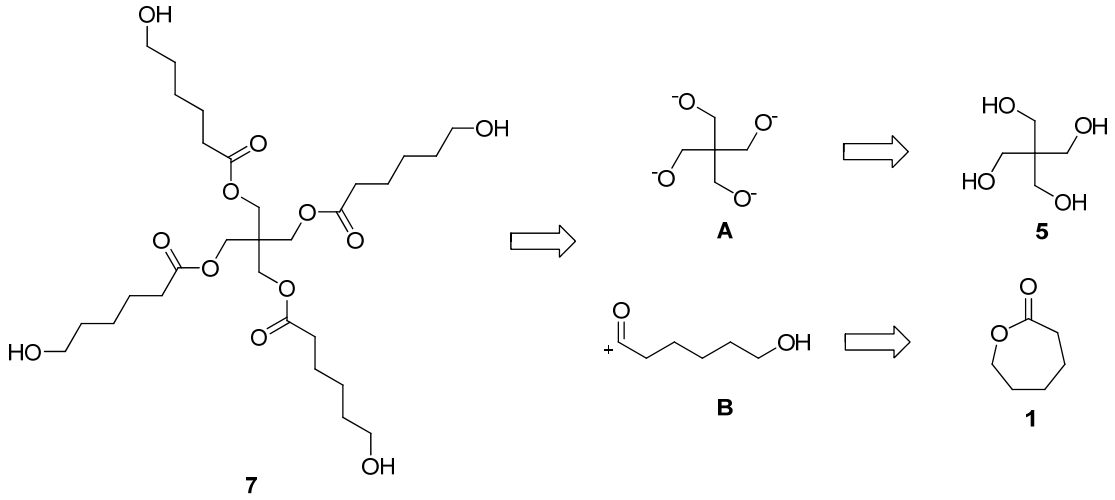

Scheme 5.1 Retrosynthesis of pentaerythritol tetrakis(6'-hydroxyhexanoate)

The star-core macroinitiator **7**, pentaerythritol tetrakis(6'-hydroxyhexanoate) could be synthesized from *ε*-caprolactone (**1**) as shown in Scheme 5.2, *via* transmethylation, alcohol protection, hydrolysis, esterification and deprotection respectively.

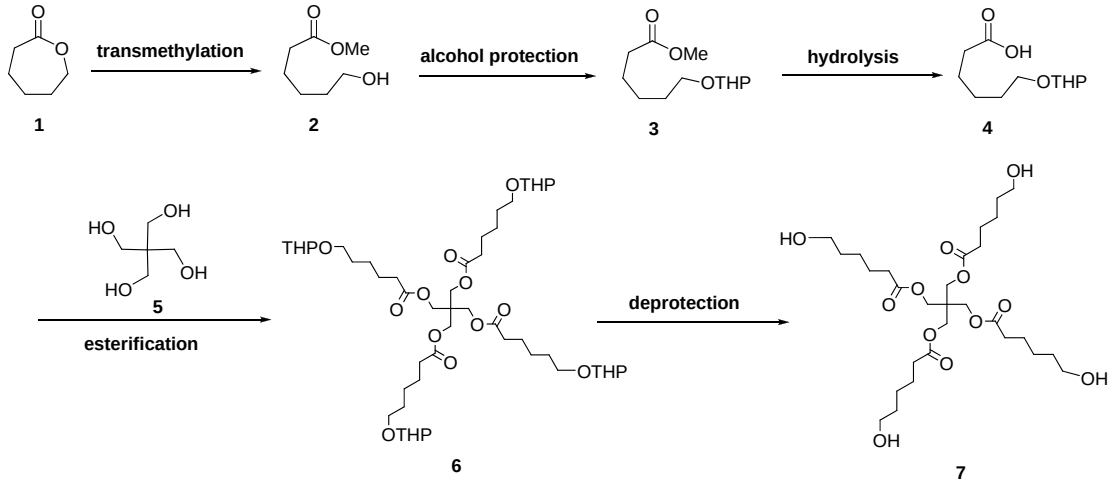

Scheme 5.2 Synthesis of pentaerythritol tetrakis(6'-hydroxyhexanoate) (**7**)

Synthesis of pentaerythritol tetrakis(6'-hydroxyhexanoate) (**7**) was started from transmethylation reaction of *ε*-caprolactone (**1**) as shown in Scheme 5.3. A mixture of compound **1** and conc. H_2SO_4 in excess anhydrous methanol was heated to reflux overnight. Compounds **2** in 79% yield were obtained by flash column chromatography (silica gel) using ethyl acetate (EtOAc) : hexanol = 1 : 9 as eluent.

Compound **2** was identified by spectroscopic techniques, ^{1}H NMR data of methyl ester of **2** appeared singlet *δ* at 3.68 ppm, the proton at 2-position appeared triplets *δ* at 2.34 ppm and the

proton at 6-position appeared triplets δ at 3.66 ppm as shown in Figure 5.1. IR data displayed broad peak of O-H stretching of hydroxyl at 3403 cm^{-1} and C=O stretching of ester at 1732 cm^{-1}.

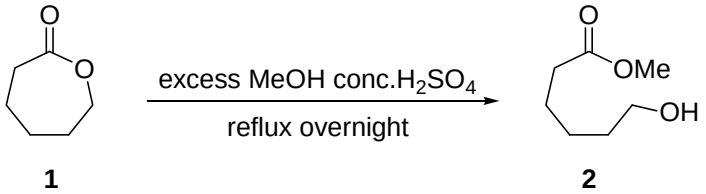

1 **2**

Scheme 5.3 Translation of methyl 6-hydroxyhexanoate (**2**)

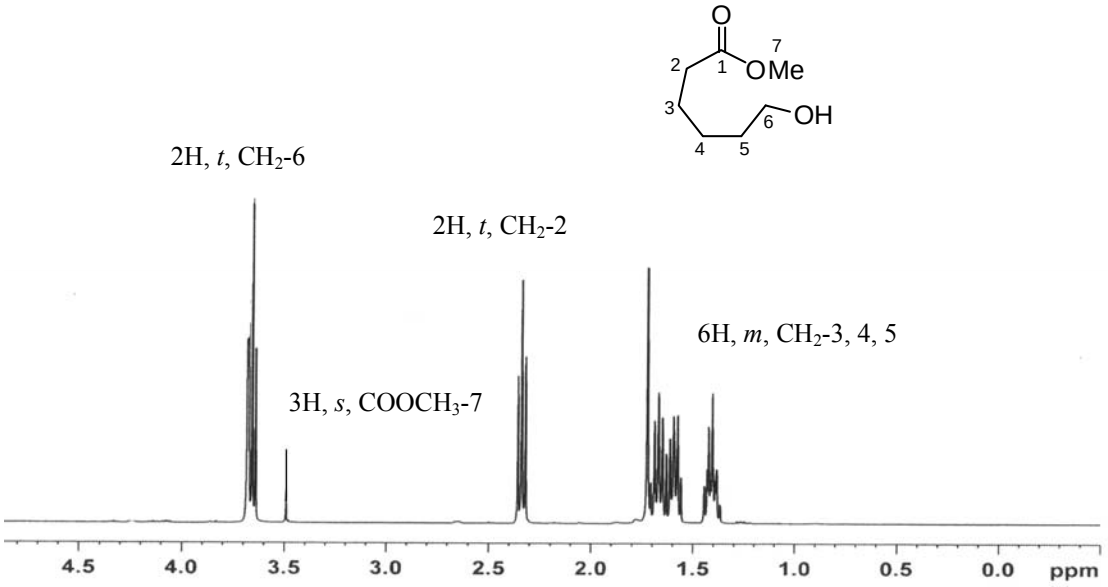

Figure 5.1 ^{1}H-NMR spectra data of compound **2**.

The protection of active hydroxyl group was success by using 3,4-dihydro-2*H*-pyran (1.5 eq.) in the $CHCl_3$ solution and present of montmorillonite K10 as a catalyst gave compound **3** as shown in Scheme 5.4.

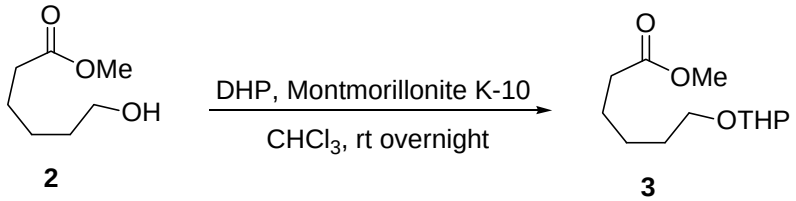

2 **3**

Scheme 5.4 Protection of alcohol by using DHP and M-K10

Compound **3** was identified by spectroscopic techniques, ^{1}H NMR data of methyl ester of **3** appeared singlet δ at 3.69 ppm and CH–O triplet δ at 4.59 ppm as shown in Figure 5.2. IR data displayed peak of C–O stretching of ether at 1074, 1035 cm^{-1} and ESI-MS data revealed 253.1416 m/z $(M + Na)^{+}$ of $C_{12}H_{22}O_4Na$.

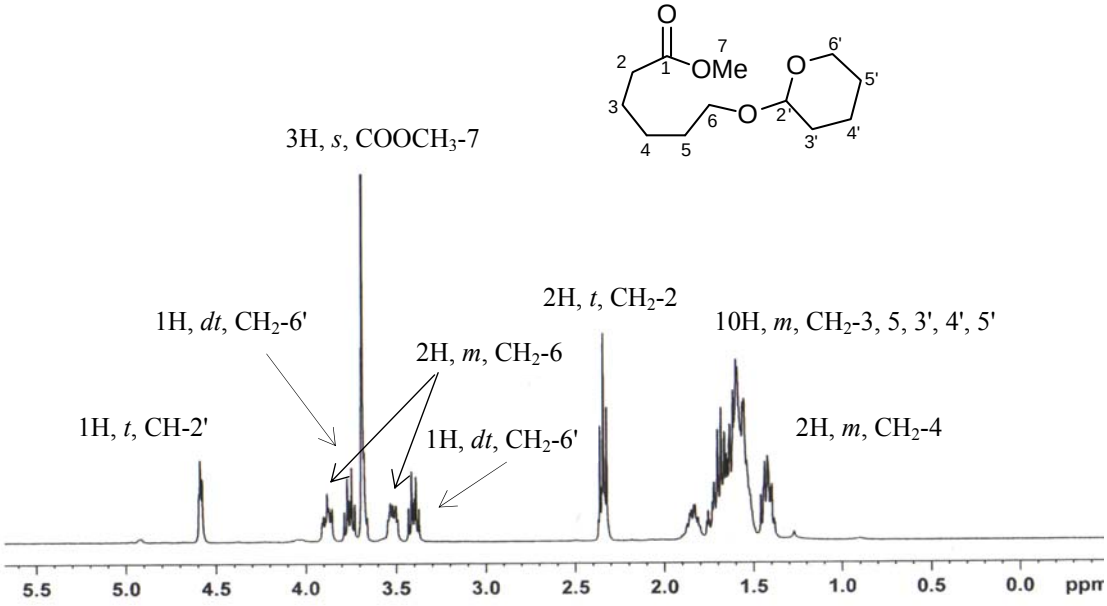

Figure 5.2 ^{1}H-NMR spectra data of compound **3**.

Subsequently, the methyl protected hydroxyl ester **3**, was hydrolyzed by NaOH to reflux in methanol and water for 1 h to give the ether acid **4** as shown in Scheme 5.5.

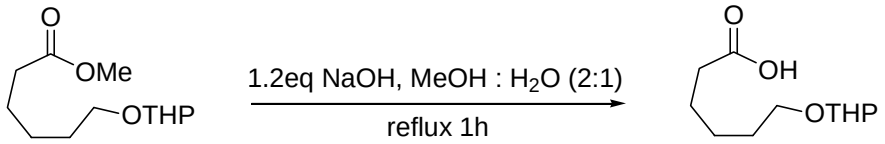

3 **4**

Scheme 5.5 Hydrolysis of compound **3**

Compound **4** was identified by spectroscopic techniques, ^{1}H NMR data of CH–O at 2'-position of **4** appeared triplrts δ at 4.60 ppm, the proton at 6'-position appeared double of doublets δ at 3.41 ppm (J = 9.63, 6.48 Hz), 3.76 ppm (J = 9.62, 6.71 Hz) and the proton at 6-position appeared multiplets δ at 3.52, 3.88 ppm as shown in Figure 5.3. IR data displayed peak of C=O stretching of carboxylic acid at 1711 cm^{-1} and ESI-MS data revealed 239.1259 m/z $(M + Na)^{+}$ of $C_{11}H_{20}O_4Na$.

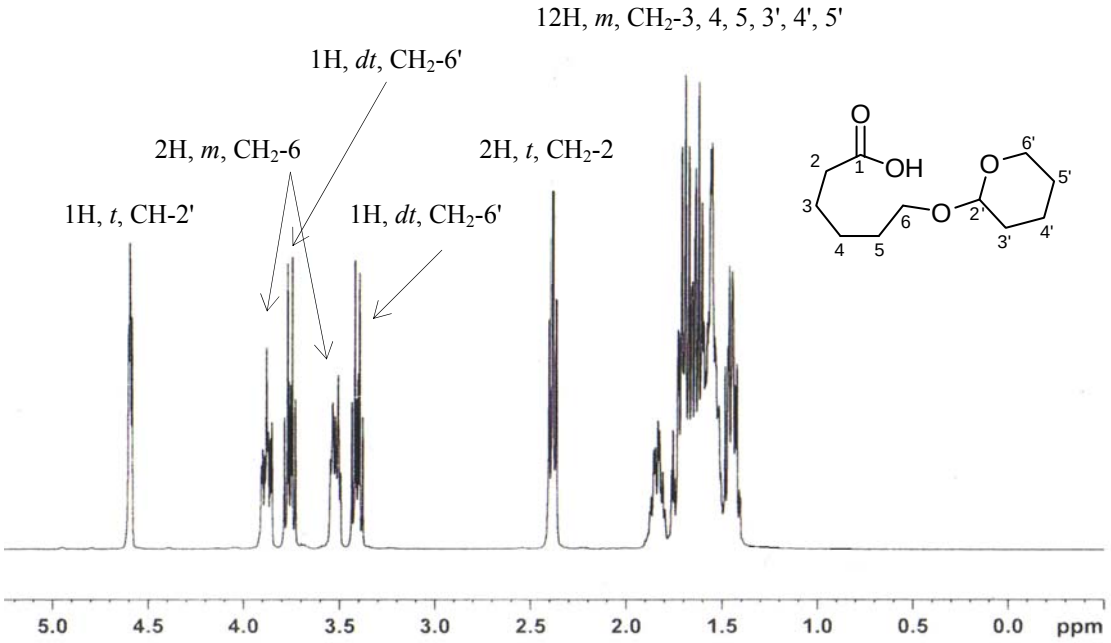

Figure 5.3 ^{1}H-NMR spectra data of compound **4**.

Final step, compound **4** reacted with pentaerythritol (**5**) in the presence of *N,N'*-dicyclohexylcarbodiimide (DCC) and 4-dimethlaminopyridine (DMAP) to yield compound **6** and then the THP group of **6** was removed by stirring with montmorillonite K-10 in methanol to yield the star-core macroinitiator (**7**) as shown in Scheme 5.6.

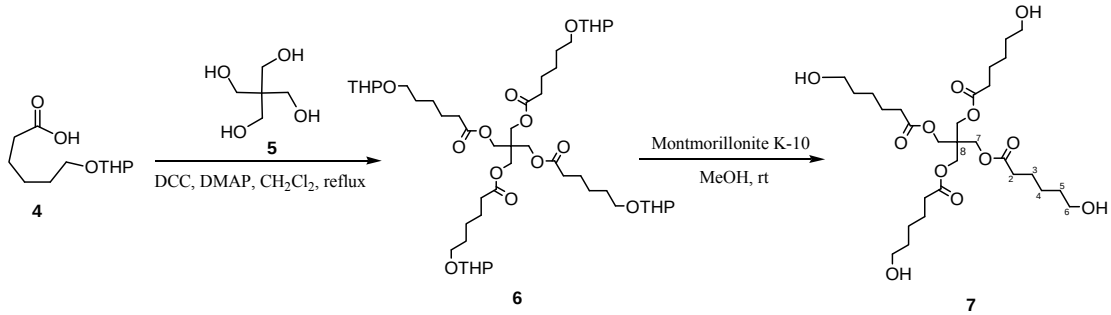

Scheme 5.6 Esterification and deprotection of compound **7**

The final product **7** was identified by spectroscopic techniques, ^{1}H NMR spectra data shown the proton at 7-position appeared singlet δ at 4.10 ppm, the proton at 6-position appeared triplets δ at 3.61 ppm (J = 6.32 Hz) and the proton at 2-position appeared triplets δ at 2.35 ppm as shown in Figure 5.4.

The IR spectrum shown absorption peaks at 1153 cm^{-1} of C-O stretching of ester, at 1407 cm^{-1} of CH_2 bending, at 1747 cm^{-1} of C=O stretching of ester, 2946 and 2871 cm^{-1} of CH_2 stretching and at 3381 cm^{-1} of O–H stretching of alcohol as shown in Figure 5.5. ESI-MS data revealed 615.3356 m/z $(M + Na)^+$ of $C_{29}H_{52}O_{12}Na$.

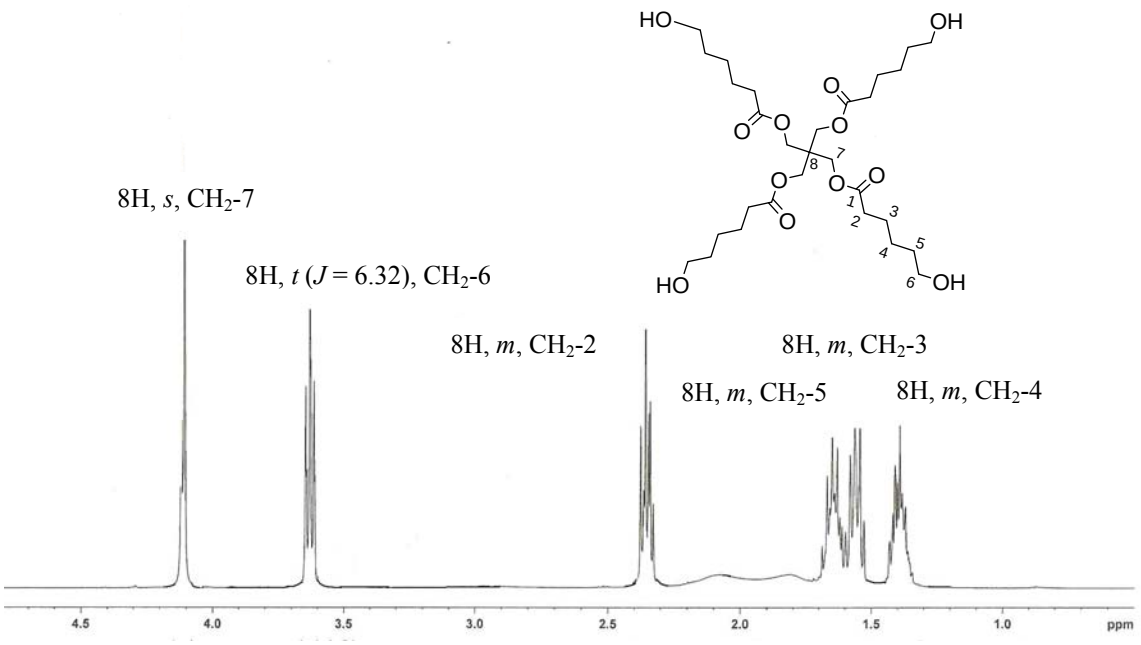

Figure 5.4 ^{1}H-NMR spectra data of compound **7**.

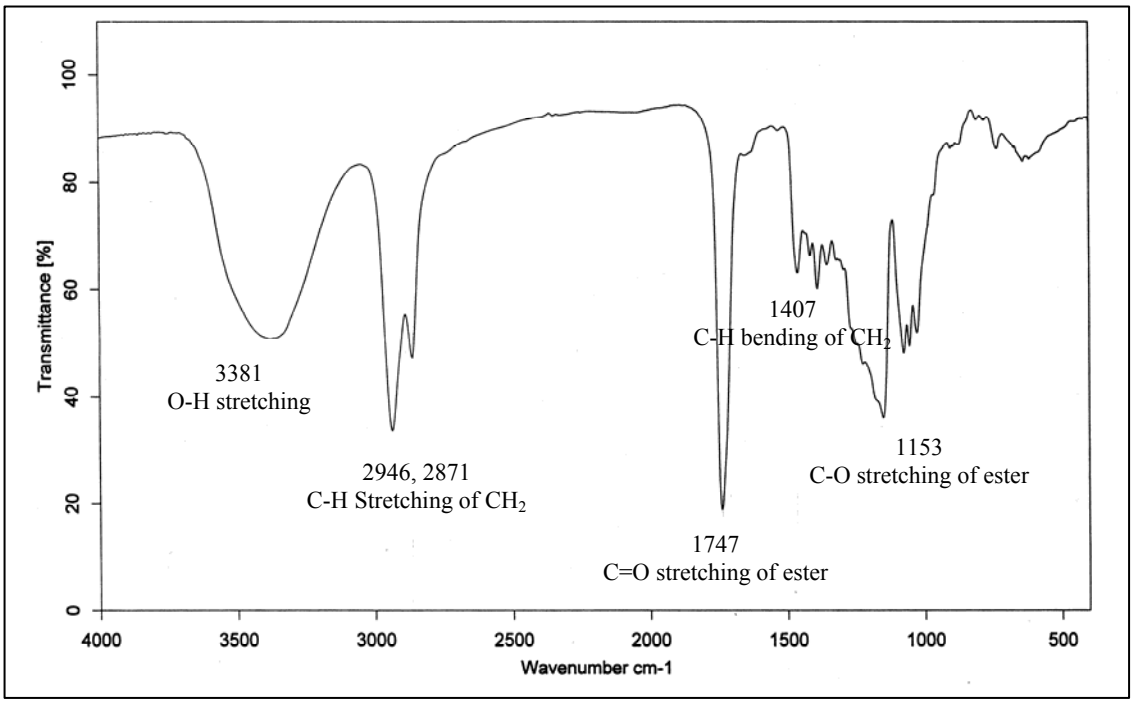

Figure 5.5 IR data of compound **7**.

5.2 Synthesis of Low Molecular Weight PCL Model Compounds with Different Molecular Architectures

Low molecular weight PCL model compounds with different molecular architectures were synthesized by ROP of ε-caprolactone at 120ºC for 48 hours using 0.1 mole % $SnOct_2$ as a catalyst and 4 mole % of 1-hexanol, PTOL and pentaerythritol tetrakis(6'-hydroxyhexanoate) as initiators. The structure of the PCLs depends on the functional initiating cores. Monofunctional alcohol (1-hexanol) yielded linear PCL (PCL_1-hexanol), while multifunctional alcohols (PTOL) and

multifunctional pentaerythritol tetrakis(6'-hydroxyhexanoate) macroinitiator yielded star-shaped PCLs (PCL_PTOL and PCL_macroinitiator respectively) as shown in Figure 5.6 (a-c). The route of synthesis in this study was the core-first method where polymer chains were grown directly from a functional core.

(a)

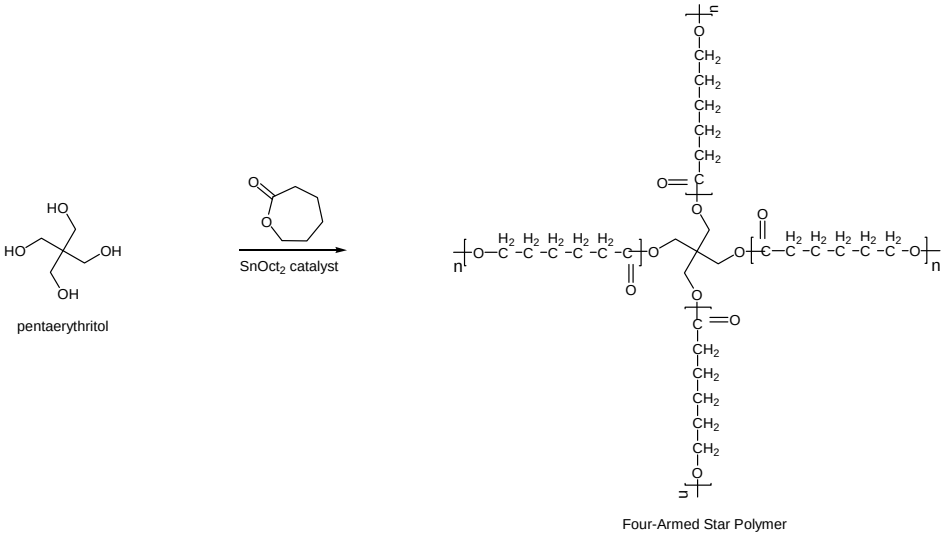

(b)

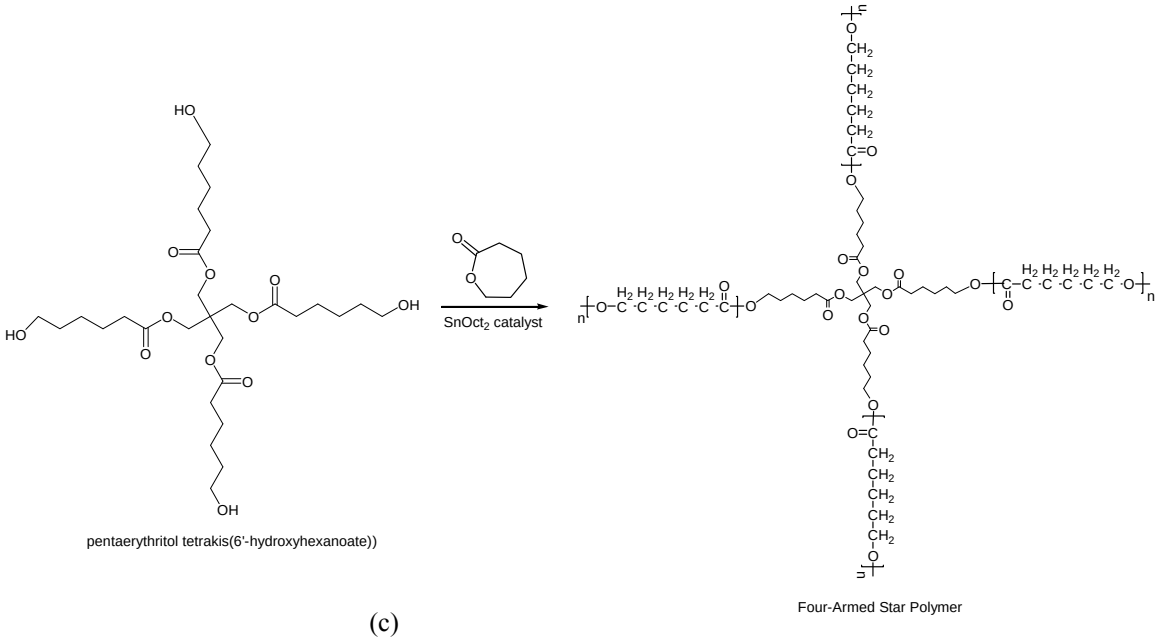

(c)

Figure 5.6 Polymerization of ε-caprolactone using 0.1 mole % $SnOct_2$ as a catalyst and 4 mole% of (a) 1-hexanol (b) PTOL and (c) pentaerythritol tetrakis(6'-hydroxyhexanoate) as initiators at 120ºC for 48 hours**.**

Relatively high amount of initiator (4% by mole monomer) was used to obtain low molecular weight PCLs as model compounds in order to confirm the structure and evaluate the influence of short-chain architecture on the properties. The structures and properties of the resulting PCL oligomers were characterized by GPC, dilute-solution viscometry, ^{1}H-NMR, DSC and TG analysis. All results are summarized in Table 5.1 and the details will be described in the following sections. The physical appearance of PCL_1-hexanol was white solids. In contrast, PCL_PTOL and PCL_macroinitiator were sticky solid. The yields of purified PCLs model compounds were quite low (65-88%) because of the high alcohol concentration used.

Table 5.1 The results of low molecular weight PCL model compound with different molecular architectures.

Polymer	**PCL_1-hexanol**	**PCL_PTOL**	**PCL_macroinitiator**
Amount of Polymer (g)	2	2	2
Catalyst (mole%)	$SnOct_2$ (0.1)	$SnOct_2$ (0.1)	$SnOct_2$ (0.1)
Initiator (mole%)	1-hexanol	PTOL	Macroinitator
Monomer : Initiator (mole%)	100 : 3.94	100 : 3.94	100 : 4.74
Temperature (ºC) ***and Time*** (hr)	120°C, 48 hr	120°C, 48 hr	120°C, 48 hr
% yield (purified)	88.5	65.0	74.0
Physical Appearance (crude)	white solid	colorless liquid	colorless liquid
Physical Appearance (purified)	white solid	sticky solid	sticky solid
Molecular weight (g mole^{-1})			
$\overline{M}_{n,theory}$	2,956	3,033	2,970
GPC			
$\overline{M}_n$	1,662	1,718	894
$\overline{M}_v$	8,274	5,330	3,555
$\overline{M}_w$	5,213	3,884	2,381
Dilute-Solution Viscometry			
$[\eta]$ in THF at 30ºC (dl/g)	0.11	0.10	0.09
$\overline{M}_v$	4,572	4,319	3,593
$g^{1/2}$ *	-	0.80	0.80
g' **	-	0.91	0.82
$g^{1/2}/g'$ ***	-	0.88	0.98
^{1}*H-NMR*			
Average DP_n/Arm, $_{NMR}$	27.8	7.9	7.6
Average DP_n/Arm, $_{Theory}$	25.0	6.3	6.3
Number of initiating OH, $_{NMR}$	0.9	3.2	3.3
Number of initiating OH, $_{Theory}$	1.0	4.0	4.0
$\overline{M}_{n,NMR}$	3,271	3,734	3,606

Table 5.1 The results of low molecular weight PCL model compounds with different molecular architectures (continued).

Polymer	**PCL_1-hexanol**		**PCL_PTOL**		**PCL_macroinitiator**	
Thermal Properties						
DSC	1st run	2nd run	1st run	2nd run	1st run	2nd run
T_m, onset (ºC)	53.7	51.4	36.3	32.4	34.5	-
T_m, Peak (ºC)	59.7	55.0	44.5	35.8	40.0	-
Heat of Fusion (J/g)	108.3	94.8	59.3	60.0	34.4	-
Degree of Crystallinity (%)	80.2	70.2	43.9	44.4	25.4	-
TGA						
$T_{d,\ 10\%}$ (ºC)	340		349		341	
$T_{d,\ 50\%}$ (ºC)	372		384		384	
$T_{d,\ range}$ (ºC)	157-545		116-554		103-549	

Note * The ratio of mean-square radius of gyration of a star-shaped polymer with the number of arms (*f*)

** The ratios of intrinsic viscosities of star-shaped polymer to that of linear polymer

*** For a star-shaped polymer with perfect arm structure, there will be an important relationship $g^{1/2}/g' = 1.0$

5.2.1 Molecular Weight Determination of PCL Model Compounds by GPC and Dilute-Solution Viscometry

In this study, the average molecular weights of low molecular weight PCL model compounds were determined by GPC. Typical GPC curves of the purified PCL model compounds are shown in Figure 5.7 and the various average molecular weights ($\overline{M}_n$, $\overline{M}_v$ and $\overline{M}_w$) for all samples are compared with $\overline{M}_n$'s theoretical values in Table 5.1.

From GPC results, the molecular weight of purified linear and star-shaped PCL model compounds ($\overline{M}_{n,GPC}$ ≈ 900-1,700) were controlled by using the ratio 100:4 mole% of monomer to initiator. As expected, the low molecular weight PCL was achieved with using the high concentration of initiator, consistent with reports from Dong *et al.* [6, 7] and Thapsukhon [8]. The result indicates that hydroxyl-containing compounds are real initiator, which can stoichiometrically control the molecular weight of the polymer. The $SnOct_2$ acted only as a catalyst, increasing the polymerization rate but having no effect on the molecular weight. However, controlled polymerization has been achieved when using very dry systems with a controlled amount of a hydroxyl-containing compound.

The GPC curve presented unimodal molecular weight distribution (MWD), which suggests that no mixture of star-shaped and linear is formed. The theoretical number-average molecular weight ($\overline{M}_{n,theory}$) were calculated from $\overline{M}_{n,theory}$ = $MW_{initiator}$ + (n × MW of ε-caprolactone), where n = number of repeating unit (mole of ε-caprolactone / mole of initiator).

Sample Calculation: for PCL_1-hexanol

$$\text{Theoretical number - average molecular weight} = 102.18 + (\frac{100x114.14}{4})$$

$$= 2956 \text{ g mole}^{-1}$$

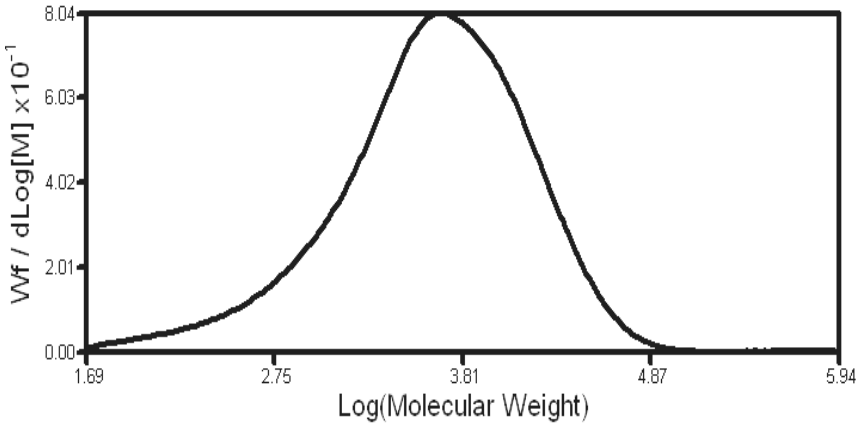

(a)

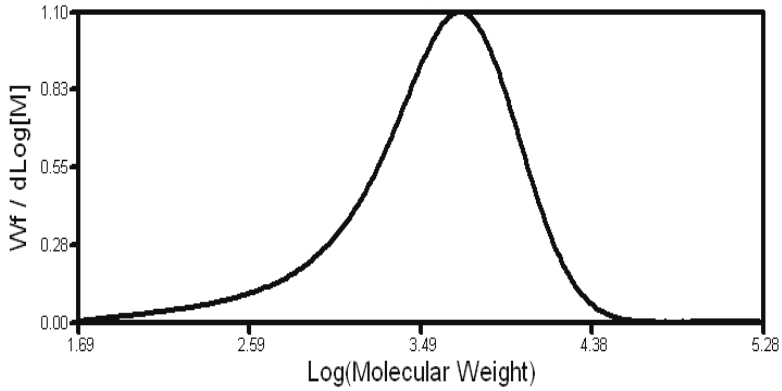

(b)

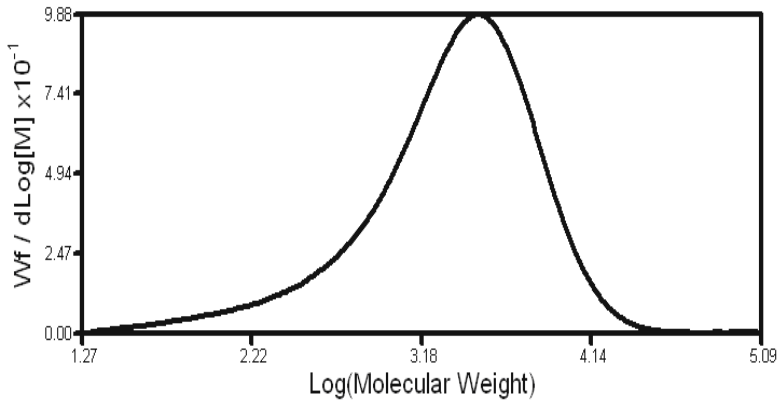

(c)

Figure 5.7 GPC curves of low molecular weight purified PCL model compounds; (a) PCL_1-hexanol (b) PCL_PTOL and (c) PCL_macroinitiator.

The calculated number average molecular weight ($\overline{M}_{n,theory}$) using the following equations assuming that all of initiating molecules acted and were incorporated in the polymers. Bearing in mind that variation in the number of arms was accomplished by using different initiating core initiator and the arm lengths were controlled to get the same molecular weight oligomers by controlling monomer to initiator molar ratio in this study.

The $\overline{M}_{n,GPC}$ values of all linear and star-shaped PCLs from GPC results are lower than the theoretical values that calculated from the monomer to initiator ratio assuming hydroxyl initiation as compared in Table 5.1. This indicates that initiation by another species has also occurred.

However, the $\overline{M}_n$ values of star-shaped PCL_macroinitiator from GPC result ($\overline{M}_{n,GPC}$ = 894) was not close to the theoretical value ($\overline{M}_{n,theory}$ = 2970), which could be described to the unique molecular structure of star-shaped PCL. The GPC analysis always underestimates the molecular weight star-shaped polymers because it has smaller hydrodynamic volume than that of linear polystyrene having the same molecular weight. For star-shape polymers, the GPC technique is not the appropriate method to determine the molecular weight [9].

Viscosities of the synthesized linear and star-shaped PCLs oligomers were measured at 30.0ºC in THF solution. Under a series of PCL concentrations, reduced viscosities (η_{red}) and inherent viscosities (η_{inh}) were measured and evaluated. Furthermore, intrinsic viscosity, [η] was estimated via the extrapolation of the η_{red} and η_{inh} versus polymer concentration plot and the results are shown in Table 5.2.

The viscosity-average molecular weights ($\overline{M}_v$) values of the low molecular weight PCLs were calculated from Mark-Houwink-Sakurada Equation; $[\eta] = K\overline{M}_v^{\,a}$, where K and a are the characterization parameters predominantly determined by the combination of polymer and solvent at constant temperature. An example of the type of flow-time data obtained, derived viscosity parameters, and reduced/inherent viscosity-concentration graphs are shown in Table 5.2 and Figure 5.8. The double extrapolation of the 2 graphs in Figure 3.8 to their common intercept at zero concentration (c = 0) gives the value of the intrinsic viscosity, [η], from which the value of $\overline{M}_v$ is calculated as follows:

Sample Calculation of $\overline{M}_v$: for PCL_macroinitiator

From Figure 5.8 (c)

$[\eta] = (\eta_{red})_{c=o} = (\eta_{inh})_{c=o} = 0.0902$ dl/g

When this value of [η] is substituted into the Mark-Houwink-Sakurada Equation for PCL in THF as solvent at 30ºC [10] of:

$$[\eta] = 1.40 \times 10^{-4}\ \overline{M}_v^{\,0.79} \text{ dl/g}$$

it yields

$$0.0902 = 1.40 \times 10^{-4}\ \overline{M}_v^{\,0.79}$$

$$\overline{M}_v = 3{,}593$$

From the viscosities and $\overline{M}_v$ values results, it was found that in dilute solution, low molecular weight star-shaped PCLs exhibited slightly lower intrinsic viscosity than linear PCL, indicating the expected star-shaped structure. It is due to the star-shaped has a higher segment density within the distance of its radius of gyration and lower hydrodynamic volume than linear polymers.

Table 5.2 Dilute-solution viscometry data of low molecular weight PCL_ macroinitiator using THF as solvent at 30ºC.

Concentration (g/dl)	Flow-Time* (second)	η_{rel}	η_{sp}	η_{red} (dl/g)	η_{inh} (dl/g)
solvent	120.01	-	-	-	-
0.2044	122.49	1.0207	0.0207	0.1011	0.1001
0.4268	125.81	1.0483	0.0483	0.1132	0.1106
0.6000	128.86	1.0738	0.0738	0.1230	0.1186
0.8004	133.00	1.1082	0.1082	0.1352	0.1284
1.0008	137.54	1.1461	0.1461	0.1460	0.1362

* average of at least 3 readings which agree to within ±0.2% of this average value

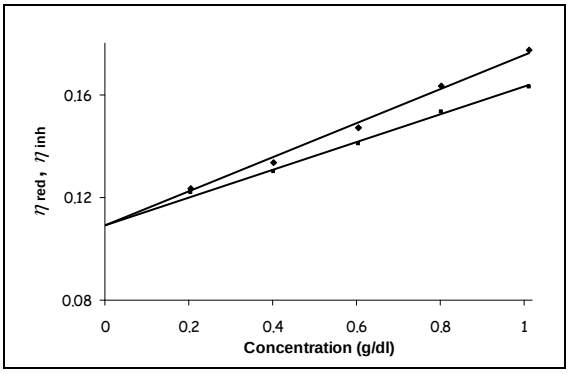

(a)

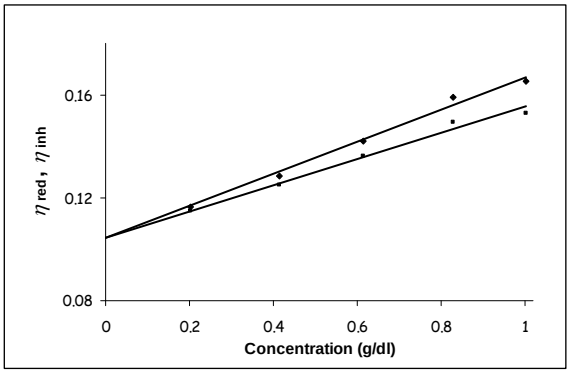

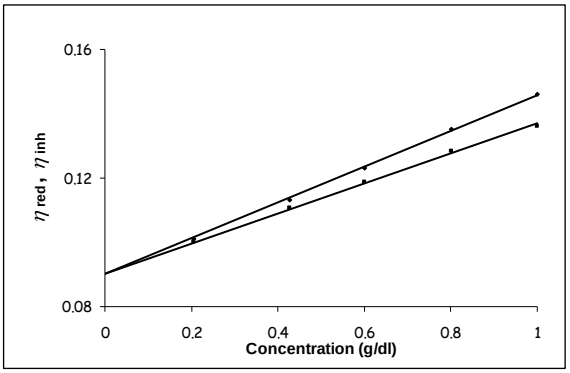

(b) (c)

Figure 5.8 Reduced (η_{red}) and inherent (η_{inh}) viscosity-concentration plots of low molecular weight; (a) PCL_1-hexanol, (b) PCL_PTOL and (c) PCL_macroinitiator (♦ η_{red} and ■ η_{inh})

The fine structures of the synthesized star-shaped PCLs could be estimated by comparing the mean square radius of gyration and intrinsic viscosities with linear polymer [11-13]. Degree of branching of star polymer can be estimated by comparing the mean-square radii with linear polymer. The equation (5.1) provided a mean-square radius of gyration ($g^{1/2}$) of a star-shaped polymer with the number of arms (f).

$$g^{1/2} = \frac{6f}{(f+1)(f+2)} \qquad \text{…….. (5.1)}$$

The ratios of intrinsic viscosities of star-shaped PCLs to that of linear PCL (g') bearing similar absolute molecular weight could be experimentally estimated in accordance to equation 5.2

$$g' = [\eta]_{star}/[\eta]_{linear} = K_{star}M_w^{\,a}(\text{star})/K_{linear}M_w^{\,a}(\text{linear}) \qquad \text{…….. (5.2)}$$

where K and a represent Mark-Houwink constants.

For a star-shaped polymer with perfect arm structure, there will be an important relationship of $g^{1/2} = g'$ or $g^{1/2}/g' = 1.0$ as proposed by Zimm and Kilb. [13] From Table 5.1 summarized the calculated values of $g^{1/2}/g'$ for the star-shaped PCLs prepared with PTOL and macroinitiator. It could be seen that the $g^{1/2}/g'$ value of star-shaped PCL_macroinitiator (0.98) was very close to 1.0

for an ideal star-shaped polymer with perfect arm architecture [13]. Deviations from this relationship for PCL_PTOL (0.88) would point to contamination of the system, e.g. with linear chains.

GPC and dilute-solution viscosity analysis are not the appropriate method to determine the molecular weight for star-shaped polymer. Since it has the smaller hydrodynamic volume than that of linear polystyrene having the same molecular weight, the GPC analysis always underestimates the molecular weight of star-shaped polymers. However, simultaneous measurement of light scattering intensity and concentration allows direct determination of the weight molecular weight of the eluted fraction, without calibration using the standard. To identify the chain branching, GPC can be coupled with viscometer or laser light scattering detectors, such as low-angle laser light scattering (LALLS) or multi-angle laser light scattering (MALLS) detectors. For polymer with low molar mass, light scattering may suffer from a lack of sensitivity; hence, a viscometer coupled with GPC constituted an interesting alternative [14].

5.2.2 Structural Analysis and Molecular Weight Determination of PCL Model Compounds by ^{1}H-NMR Spectroscopy

The structure of the low molecular weight PCL model compounds with different molecular architectures were characterized by ^{1}H-NMR. The ^{1}H-NMR spectra of PCLs in deuterated chloroform solutions were recorded using a Bruker Avace 400 MHz NMR spectrometer with tetramethylsilane (TMS) as internal standard at room temperature. The spectra of purified PCLs are shown in Figure 5.9. The summarized interpretations from the proton assignments of corresponding chemical shift and peak area integration are given in Table 5.3.

The low molecular weight PCLs spectra show characteristic peaks of CL unit in agreement with previous study [6]. The characteristic peak of monomer unit and initiators were similarly assigned as shown in Figure 5.9. The CH_2-OH methylene proton signal (hydroxyl at end chain, (g)) of the PCL arms were found in all samples at 5.55-5.63 ppm and the results confirmed that PCL was terminated by hydroxyl end groups [15]. The appearance of CH_2-O (a) of PTOL and PTOL_macroinitiator initiated polymerization proves that these two initiators participated in the polymerization. However, this signal in 1-hexanol initiated polymerization was not found owing to the overlapping of the CH_2-O (f) peak, the reason for this is might be both CH_2-O (a) and CH_2-O (f) have almost same surrounding protons. The methyl groups (h) of 1-hexanol initiated polymer were also found except PTOL and PTOL_macroinitiator that have no methyl group in it structure. From ^{1}H-NMR results, linear and star-shaped PCLs with hydroxyl end groups were successfully synthesized from homopolymerization of CL with different number of hydroxyl group as initiator.

The molecular weight determinate by ^{1}H-NMR spectroscopy was calculated from the integration ratio the methylene protons in the repeating unit and the methylene proton in the terminal unit. It was found that the number average molecular weight determined by ^{1}H-NMR was close to the theoretical values as compared in Table 5.1. However, the average molecular weight calculated from ^{1}H-NMR was higher than those determined by GPC. ^{1}H-NMR was used to calculate the average number of hydroxyl groups in the initiator that participate in the initiation. The initiation activity was estimated indirectly by comparing theoretical with average degree of polymerization per arm (DP_n/arm) determined by ^{1}H-NMR. All low molecular weight PCLs were analyzed and the results are shown in Table 5.4.

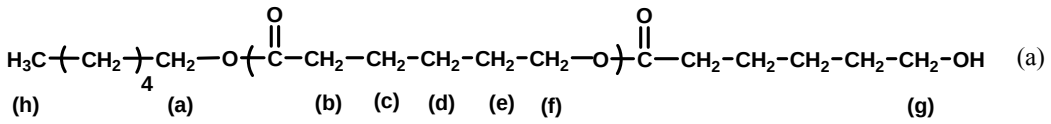

(a)

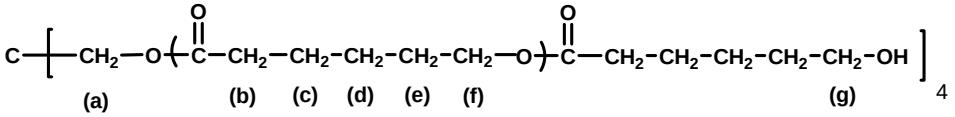

(b)

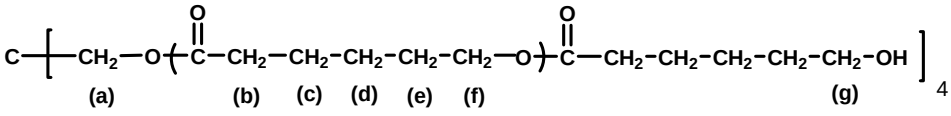

(c)

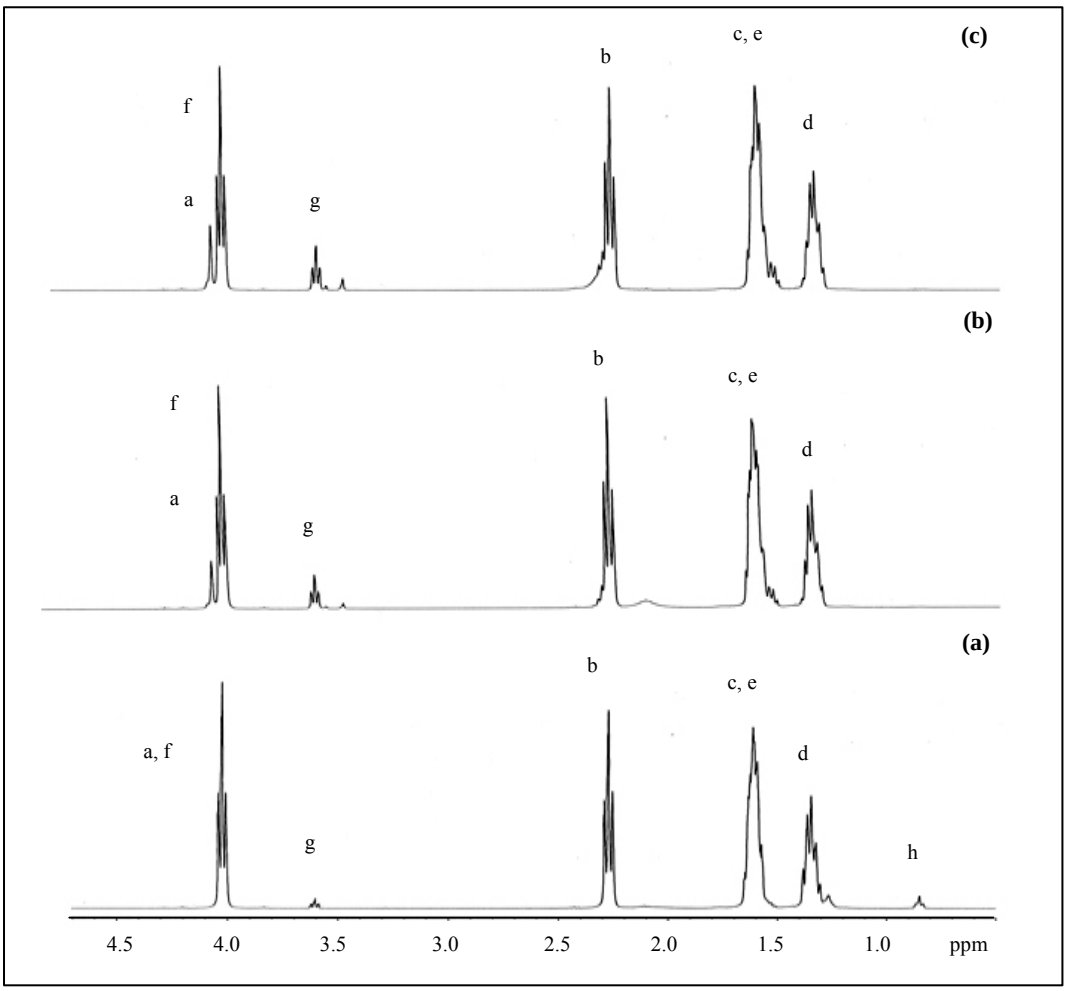

Figure 5.9 ^{1}H-NMR spectrum of low molecular weight crude PCLs; (a) PCL_1-hexanol (b) PCL-PTOL and (c) PCL-macroinitiator recorded in $CDCl_3$.

Table 5.3 Proton assignments and corresponding chemical shift ranges for the various resonance peaks in the ^{1}H-NMR spectra of the linear and star- shaped low molecular weight purified PCL model compounds.

Proton Assignment	Chemical Shift Range, δ (ppm)		
	PCL_1-hexanol	PCL_PTOL	PCL_macroinitiator
a	-	4.21-4.29	4.07-4.20
f	4.00-4.20	4.01-4.29	4.00-4.07
g	3.59-3.63	3.60-3.63	3.55-3.61
b	2.25-2.29	2.26-2.34	2.25-2.45
c, e	1.60-1.65	1.52-1.66	1.51-1.65
d	1.23-1.39	1.32-1.41	1.30-1.47
h	0.82-0.88	-	-

Table 5.4 Proton assignments and corresponding peak area integrations for the various resonance peaks in the ^{1}H-NMR spectra of the linear and star- shaped low molecular weight purified PCLs model compounds.

Proton Assignment	Peak Area Integration		
	PCL_1-hexanol	PCL_PTOL	PCL_macroinitiator
a	-	-	-
f	2.00	2.00	2.00
g	0.07	0.26	0.31
b	1.99	2.03	2.41
c, e	4.07	4.10	4.07
d	2.25	2.05	2.06
h	0.1	-	-

Average DP_n/arm of PCLs were calculated by comparing the peak integrals of chain methylene protons (Figure 5.9, (b) = 2.25-2.45 ppm) with those of methylene protons next to the terminal hydroxyl group (Figure 5.9, (g) = 3.55-3.63 ppm). This gives the average DP_n/arm in ε-caprolactone unit and, as presented in equation (5.3).

$$Average\,DP_n/arm = \frac{peak\ integral\ of\ protons\ at\ (b)}{peak\ integral\ of\ protons\ at\ (g)} \qquad \text{…….. (5.3)}$$

From Table 5.4, the average DP_n/arm calculated from ^{1}H-NMR were slightly greater than the theoretical values. Probably, the difference between the calculation and theoretical values is due to the lower initiation activity of the added arm in initiator.

The number average molecular weight determined by ^{1}H-NMR spectroscopy was calculated from equation (5.4).

$$\overline{M}_{n,\,NMR} = MW_{initiator} + (MW\ of\ \varepsilon - caprolactone \times DP_n \times arm\ number) \quad \text{…….. (5.4)}$$

It was found that the number average molecular weight determined by ^{1}H-NMR ($\overline{M}_{n,NMR}$) was slightly higher than the theoretical values ($\overline{M}_{n,theory}$) as compared in Table 5.1. The $\overline{M}_n$ showed an order as, $\overline{M}_{n,NMR} > \overline{M}_{n,theory} > \overline{M}_{n,GPC}$.

However, GPC analysis is not the appropriate method to determine the molecular weight for star-shaped polymer. Since it has the smaller hydrodynamic volume than that of linear polystyrene having the same molecular weight, the GPC analysis always underestimates the molecular weight of star-shaped polymers. The values given by GPC are affected not by the size of the molecule but also the structure of the molecule.

The average number of hydroxyl groups in the initiator that take part in the polymerization process was determined by comparing theoretical average DP_n/arm with the average DP_n/arm determined by ^{1}H-NMR as shown in equation (5.5).

$$Number\ of\ initiating-OH\ =\ \frac{theoretical\ average\ DP_n/arm}{average\ DP_n/arm\ determined\ by\ ^1H-NMR}\times\ functionality\ \ldots\ldots\ (5.5)$$

As we assumed, 1-hexanol initiating the growth of ε-caprolactone chains from one end. For example, purified PCL_1-hexanol had a theoretical average DP_n/arm of 25.0 CL units, whereas the average DP_n/arm determined by ^{1}H-NMR was 27.8. The result corresponds to value of 0.9 as the average number of hydroxyl groups initiating polymerization. As the results in Table 5.4, indicated that the linear and star-shaped PCL oligomers were successfully synthesized.

5.2.3 Thermal Characterization of PCL Model Compounds by DSC

The data in Table 5.1 compared the melting and crystallization behaviors of low molecular weight linear and star-shaped PCL model compounds synthesized using $SnOct_2$ as catalyst and different number of hydroxyl group (1- and 4-OH) initiators. The DSC thermograms of PCL model compounds are shown in Figures 5.10-5.11. The degree of crystallinity (X_c) of PCLs was determined from the enthalpy of melting using equation (5.6):

$$X_c(\%)\ =\ \frac{\Delta H_m}{\Delta H_m^{\circ}}\times 100 \qquad \ldots\ldots..\ (5.6)$$

where ΔH_m is the apparent enthalpy of melting of each sample and ΔH_m° is the extrapolated value of enthalpy corresponding to the melting of a 100% crystalline PCL, 135.0 J g^{-1} [16].

It was found that the melting temperatures (T_m) and degree of crystallinity of star-shaped PCLs (PCL_PTOL and PCL_maroinitiator) are all lower than that of linear (PCL_1-hexanol). The thermal properties will affected when branching points are introduced into the polymer. The reduction in melting point with branching is attributed to shorter chain length and the increase in the number of free chain ends, which disrupts the orderly fold pattern of the crystal and less compactly packed volume in the solution. In the second run, PCL_macroinitiator did not show any T_m because of it is very short chain length leaded to the amorphous structure. However, PCL_PTOL showed some crystallinity due to imperfect star-shape.

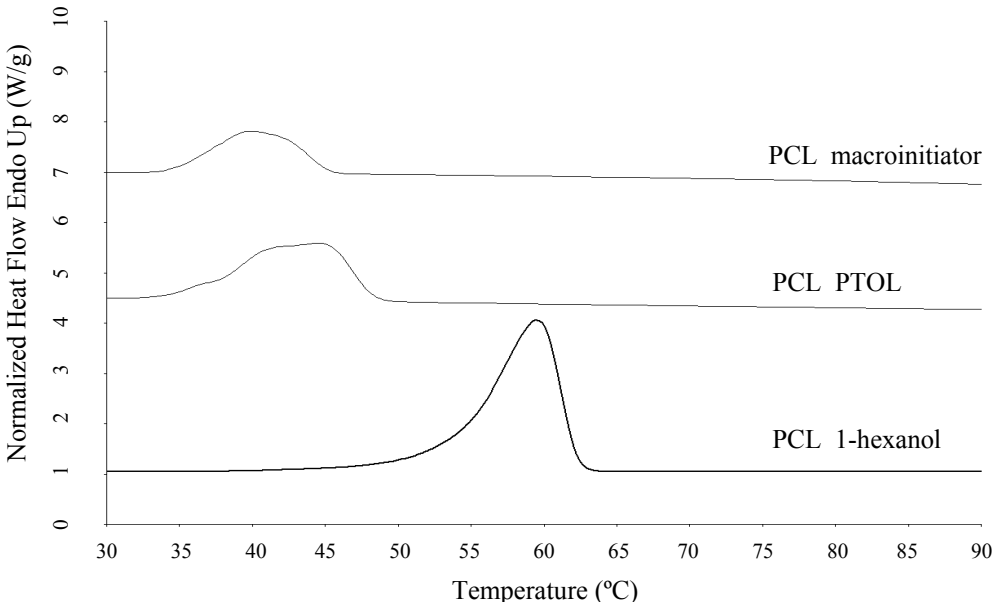

Figure 5.10 Comparison of the DSC thermograms first run of linear and star-shaped low molecular weight PCLs model compounds.

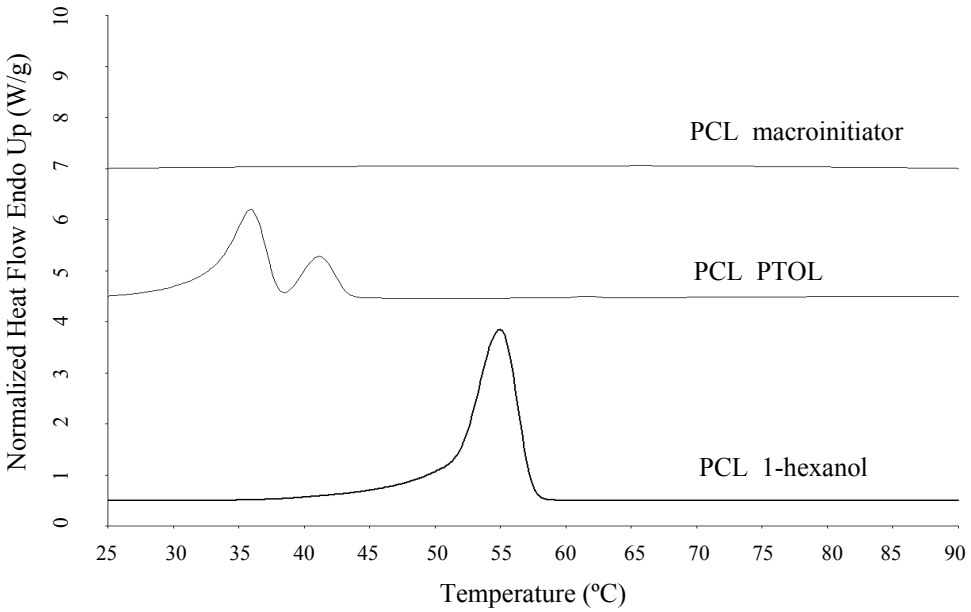

Figure 5.11 Comparison of the DSC thermograms second run of linear and star- shaped low molecular weight PCLs model compounds.

From Figure 5.11, PCL_PTOL, the initially existing shoulder in the first run becomes into two peaks in the second run, which could be due to the two different molecular weight distributions within the oligomeric range and probably in different spherulite morphology and size. In addition, the degree of crystallinity value determined in the first heating run was apparently higher than the degree of crystallinity determined in second run heating run. This indicated that the thermal history has obvious effect on the degree of crystallinity of semicrytalline PCLs.

5.2.4 Thermal Characterization of PCL Model Compounds by TGA

The dynamic (non-isothermal) TG thermograms of the linear and star-shaped low molecular weight PCLs are shown in Figure 5.12. In each case, a heating rate of 20ºC/min was used under an inert nitrogen atmosphere. In terms of "initial" ($T_{d,\ 10\%}$), "half" decomposition ($T_{d,\ 50\%}$) and temperature degradation ranges ($T_{d,\ range}$) which the weight losses occurred were compared in Table 5.1. From TG thermograms, it was found that all PCLs model compounds showed a pattern consisting only one stage degradation which could be ascribed to the homogeneous polymer products from the polymerization.

As depicted in Table 5.1, the values of $T_{initial}$ of PCL_1-hexanol is 157°C, whereas the corresponding values of $T_{initial}$ of PCL_PTOL and PCL_macroinitiator are 116 and 103°C, respectively. Star-shaped PCLs start to degrade at lower temperature than linear PCL. The result suggests that star-shaped PCLs significantly decrease the thermal stability of low molecular weight PCLs. It is reasonable that star-shaped PCLs, equal to higher end group concentration, show higher probability of chain cleavage and subsequently more readily undergo pyrolysis reaction. It has been generally accepted that the thermal degradation of different molecular architecture of PCLs was triggered by the participation of the end-capped hydroxyl groups.

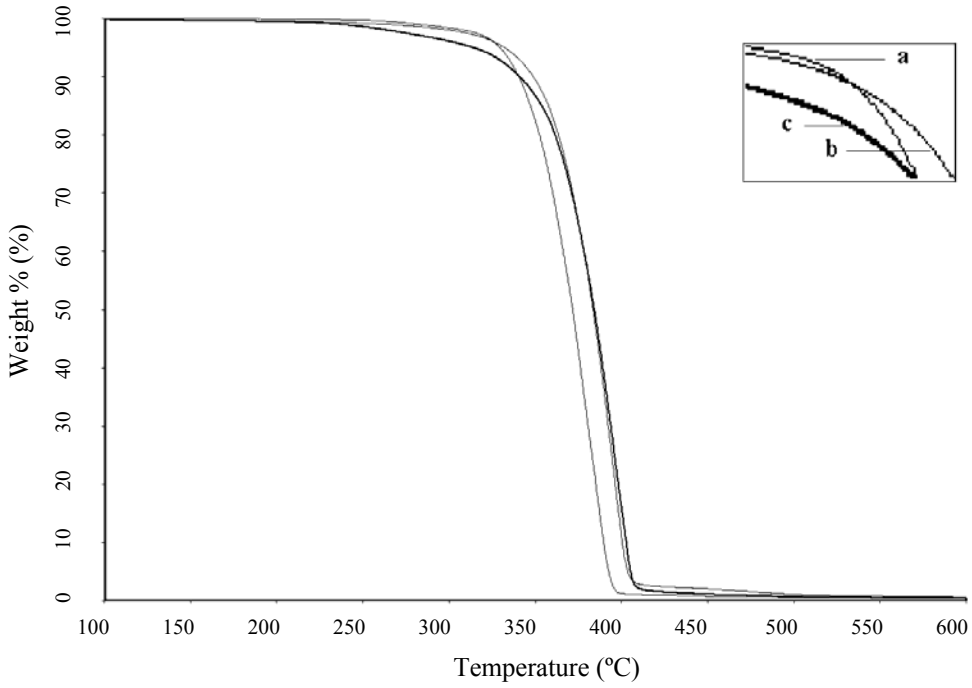

Figure 5.12 Comparison of the TG thermograms of PCL model compounds; (a) PCL_1-hexanol, (b) PCL_PTOL and (C) PCL_macroinitiator.

5.3 Synthesis and Characterization of High Molecular Weight PCL with Different Molecular Architectures

The ROP of high molecular weight PCLs homopolymers were prepared using 0.05 mole % initiator and 0.1 mole% $SnOct_2$ as catalyst at 120ºC for 72 hours. The structure of the polymer depends on the alcohol used. Monofunctional alcohol (1-hexanol) yielded linear PCL (PCL_1-hexanol), while multifunctional alcohols (PTOL) and multifunctional pentaerythritol tetrakis(6'-hydroxyhexanoate) macroinitiator yielded star-shaped PCLs (PCL_PTOL and PCL_macroinitiator

respectively) as shown in Figure 5.6 (a-c). The polymer molecular weight was fixed by controlling monomer to hydroxyl group molar ratio.

Relatively low amount of initiator (0.05% by mole monomer) was used to obtain high molecular weight PCLs in order to confirm the structure and evaluate the influence of long-chain architecture on the properties. The structures and properties of the resulting PCLs were characterized as fully as possible in order to underlying the molecular architecture-properties relationships by combination of techniques: molecular weight determination by GPC and dilute-solution viscometry, thermal transition by DSC, thermal decomposition and stability by TGA, mechanical properties by tensile testing and rheological properties by melt rheology measurements. Also, the "*in vitro*" hydrolytic biodegradability of the films was studied as an indication of their potential use in biomedical applications.

The physical appearances of all crude and purified PCLs were white solid with high % yields (97-98%). All results are summarized in Table 5.5 and the details will be described in the following sections.

Table 5.5 The results of high molecular weight PCL with different molecular architectures.

Polymer	**PCL_1-hexanol**		**PCL_PTOL**		**PCL_macroinitiator**	
Catalyst (mole %)	$SnOct_2$ (0.1)		$SnOct_2$ (0.1)		$SnOct_2$ (0.1)	
Initiator (mole %)	1-hexanol		PTOL		Macroinitiator	
Monomer : Initiator (mole %)	100 : 0.05		100 : 0.05		100 : 0.05	
Temperature (ºC) ***and Time*** (hr)	120ºC, 72 hr		120ºC, 72 hr		120ºC, 72 hr	
% yield (purified)	97.5		96.7		97.0	
Physical Appearance (crude)	white solid		white solid		white solid	
Physical Appearance (purified)	white solid		white solid		white solid	
Molecular weight (g $mole^{-1}$)						
$\overline{M}_{n,Theory}$	228,380		228,420		228,810	
GPC						
$\overline{M}_n$	16,970		19,780		16,270	
$\overline{M}_w$	53,680		60,630		60,030	
$\overline{M}_v$	46,640		51,400		50,420	
Dilute-Solution Viscometry						
[η] in THF at 30ºC (dl/g)	0.69		0.74		0.63	
$\overline{M}_v$	47,030		51,851		41,904	
Thermal Properties						
DSC	1st run	2nd run	1st run	2nd run	1st run	2nd run
T_m, onset (ºC)	54.8	53.6	56.0	52.9	51.2	52.6
peak (ºC)	58.8	55.8	61.2	56.7	56.2	55.3
Heat of Fusion (J/g)	80.8	59.8	56.2	57.9	63.5	57.3
Degree of Crystallinity (%)	59.8	44.3	41.6	42.9	47.0	42.4
TGA						
$T_{d,\ 10\%}$ (ºC)	392		389		390	
$T_{d,\ 50\%}$ (ºC)	450		448		451	
$T_{d,\ range}$ (ºC)	178-590		185-563		133-568	
Mechanical Properties						
Tensile Testing						
Stress at Break (MPa)	11.30 ± 1.08		8.59 ± 1.02		10.03 ± 1.10	
Elongation at break (%)	19.76 ± 2.54		22.66 ± 3.21		53.96 ± 2.82	
Young's Modulus (MPa)	252.46 ± 36.34		220.07 ± 25.78		215.27 13.20	

5.3.1 Molecular Weight Determinations of High Molecular Weight PCL by GPC and Dilute-Solution Viscometry

The molecular weights ($\overline{M}_n$, $\overline{M}_w$ and $\overline{M}_v$) were determined by GPC as shown in Table 5.5. The theoretical molecular weights of terpolymers ($M_{n,cal} \approx 228{,}000$) can be predicted based on the molar ratio of monomer to initiator practically participating in the polymerization. It was found that the $\overline{M}_n$'s values of all PCLs from GPC results ($\overline{M}_n \approx$ 16,000-19,000) are lower than the theoretical value. This may be ascribed to another hydroxyl initiation (water and hydroxyl-containing impurities in the system) or transesterification reaction may be occurred. It also believed that the molecular weight can be controlled by the monomer to initiator ratio within a limited range. However, the PCL_PTOL showed higher molecular weight than PCL_1-hexanol and PCL_macroinitiator because of the difficult dissolving of the PTOL initiator in cyclic esters monomers lead to lower PTOL concentration.

The intrinsic viscosity [η] values of the PCLs were obtained from their reduced and inherent viscosity-concentration plots. The results obtained for determining [η] and $\overline{M}_v$ by Mark-Houwink Sakurada equations are summarized in Table 5.5. It was found that in dilute solution, star-shaped PCL_macroinitiator lower intrinsic viscosity than linear PCL at the same molecular weight ($\overline{M}_n$), indicating the expected star-shaped structure. This is due to the fact that intrinsic viscosity reflects the chain conformation of the polymer in dilute solution.

5.3.2 Thermal Characterization of High Molecular Weight PCL by DSC

Thermal analysis of the high molecular weight linear and star-shaped PCLs was carried out by means of DSC. To enable them to be compared, all of the PCLs samples had the same thermal histories. DSC analyses were conducted at the heating rate of 10ºC/min under dry nitrogen atmosphere. The DSC thermograms for both first and second hating runs are shown in Figures 5.13-5.14 and thermal properties results are compared in Table 5.5.

DSC curves of linear and star-shaped PCLs have a single melting peak both in first and second heating run. Normally, the thermal properties will affected when branching points are introduced into the polymer and influences T_m and crystallinity. The imperfect crystallization possibly existed in the star-shaped PCLs but not in the linear PCL which rearrange and crystallize easily. However, the melting temperatures (T_m) and degree of crystallinity of star-shaped PCLs (PCL_PTOL and PCL_maroinitiator) are slighly lower than that of linear (PCL_1-hexanol) in this study. The results seem to suggest that the crystallization rearrangement of polymer chain ends is interrupted by the highly branched architecture of these polymers.

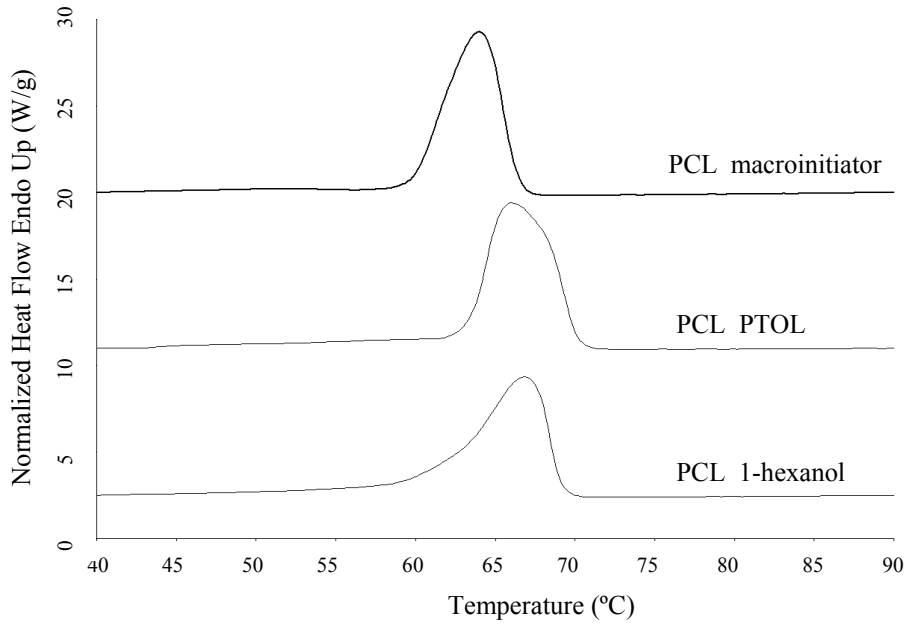

Figure 5.13 Comparison of the DSC thermograms first run of linear and star-shaped high molecular weight poly(*ε*-caprolactone) homopolymers.

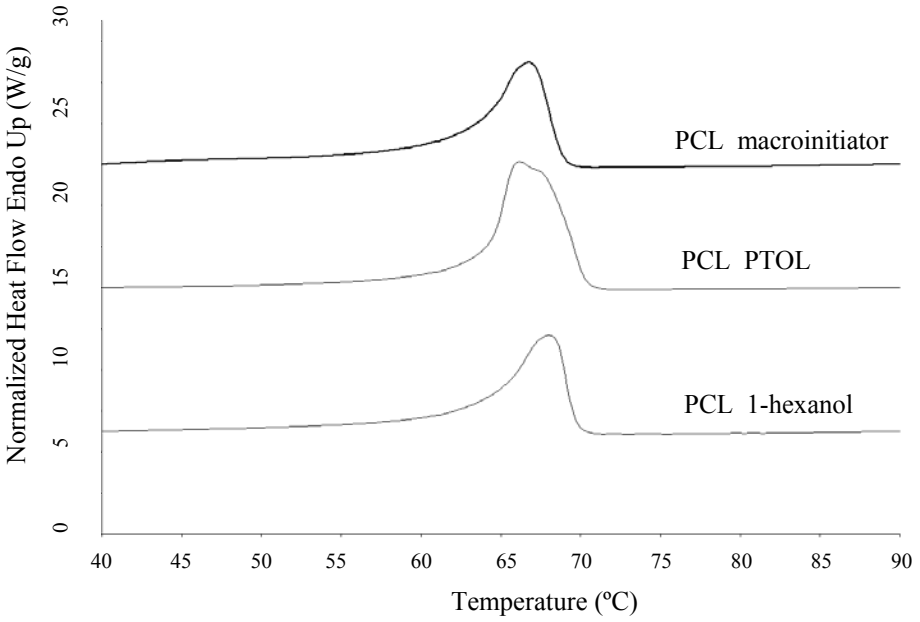

Figure 5.14 Comparison of the DSC thermograms second run of linear and star-shaped high molecular weight poly(*ε*-caprolactone) homopolymers.

5.3.3 Thermal Characterization of High Molecular Weight PCL by TG

The TG thermograms and thermal degradation ranges of the linear and star-shaped high molecular weight PCLs are compared in Figure 5.15 and Table 5.5. From TG thermograms, the star-shaped PCLs start to decompose at lower temperature than linear PCL. Although TG is not a particularly informative technique as far as polymer characterization is concerned, it is extremely useful when combined with DSC data for defining the melt processing range of polymers. In this study, the star-shaped PCLs can be processed at lower temperature than their linear counterparts because lower T_m and lower T_d, which could be advantageous, especially in the melt processing of thermo-labile polyesters.

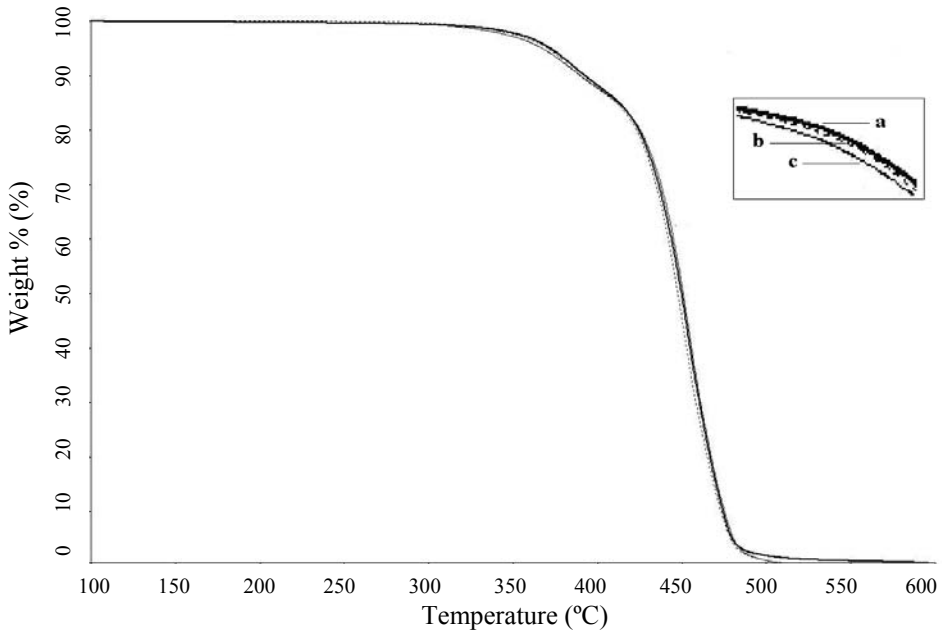

Figure 5.15 Comparison of the TG thermograms of homopolrmers; (a) PCL_1-Hexanol, (b) PCL_PTOL and (C) PCL_macroinitiator.

5.3.4 Mechanical Properties of High Molecular Weight PCL by Tensile Testing

The stress-strain curves of all PCL films are shown in Figure 5.16 and the derived property values (stress at break, % elongation at break and Young's modulus) are compared in Table 5.5. The PCL_macroinitiator showed higher %elongation at break (53%) than PCL_PTOL and PCL_1-hexanol (22% and 19% respectively). These results meant star-shaped PCL were more flexible than linear PCL and could be suggested from these results that molecular architecture of PCL affect the properties.

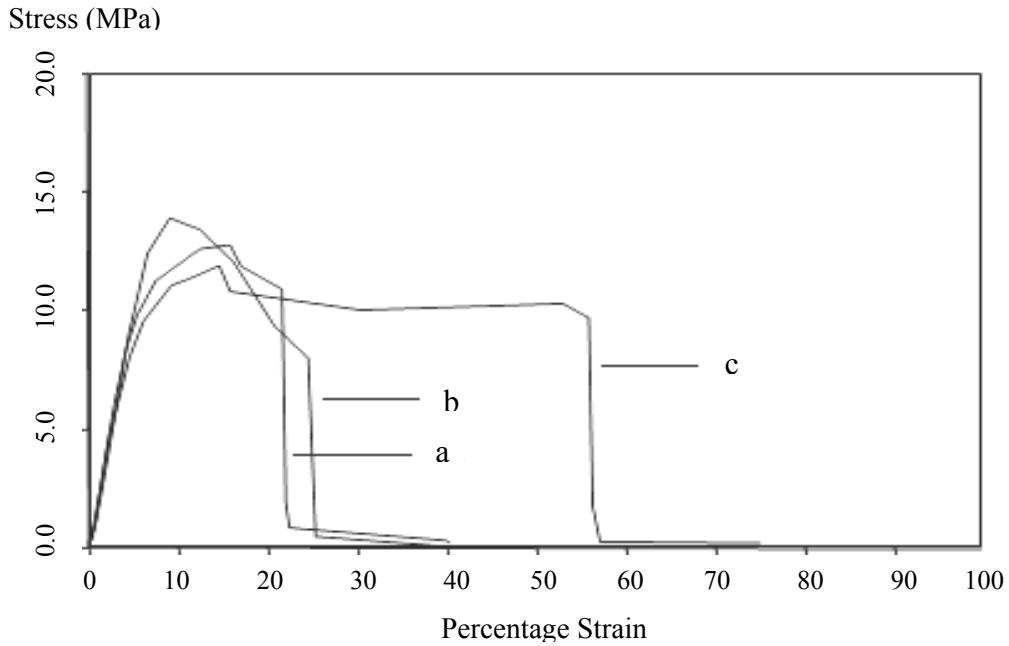

Figure 5.16 Comparison of the stress-strain curve of homopolymer; (a) PCL_1- hexanol, (b) PCL_PTOL and (C) PCL_macroinitiator.

5.3.5 Rheological Properties of High Molecular Weight PCL by Melt Rheology Measurement

One of the best methods to characterize the mechanical properties of polymer melts with respect to structure is melt rheology. The effect of molecular architecture on polymer properties in the melt was investigated in this study. Measurements of zero shear viscosity, η_o were performed as a function of frequency paralleled plate geometry of a Bohlin Gemini HR^{nano} Rotational Rheometer. The rheological behaviors of all samples were analyzed by shear rate of 0.1 to 100 rad/s under isothermal condition at 80ºC. The η_0 measurements were preformed by measuring viscosity as a function of shear rate.

Figure 5.17 shows η_0, as a function of shear rate for the high molecular weight linear and star-shaped PCL. In principle, shear viscosity of a pure polymer is divided into two distinct regions including the Newtonian and shear thinning regions as could be seen in Figure 5.17. Comparison of the flow curve for the linear and star-shaped PCLs at the same molecular weight, it was found that the η_o of PCL_1-hexanol was higher than PCL_macroinitiator at the low shear rates. It is generally found that the η_o decreases as short chains are added to a polymer backbone. Branching is often introduced to modify the flow properties of polymeric materials for specific forming operations. In contrast, the η_o of linear PCL was lower than star-shaped PCLs at the high shear rates. The expected behavior for a material with long chains is evident and this type of flow behavior is advantageous for certain processing operations.

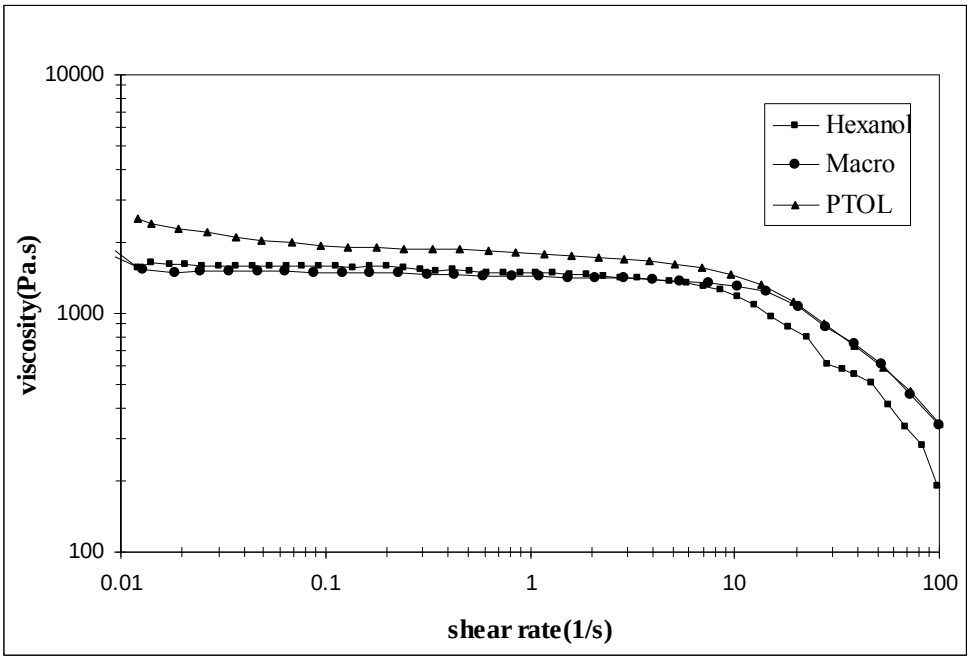

Figure 5.17 The viscosity and stress vs. shear rate (l/s) of linear and star-shaped PCL at 80ºC.

5.4 Synthesis and Characterization of High Molecular Weight PLL with Different Molecular Architectures

The ROP of high molecular weight PLLs homopolymers were prepared using 1 mole % initiator and 0.1 mole% $SnOct_2$ as catalyst at 120ºC for 48 hours. The structure of the polymer depends on the alcohol used. Monofunctional alcohol (1-hexanol) yielded linear PLL (PLL_1-hexanol), while multifunctional alcohols (PTOL) and multifunctional pentaerythritol tetrakis(6'-hydroxyhexanoate) macroinitiator yielded star-shaped PLLs (PLL_PTOL and PLL_macroinitiator respectively) as shown in Figure 5.18 (a-c). The polymer molecular weight was fixed by controlling monomer to hydroxyl group molar ratio.

The properties of the resulting PLLs were characterized as the molecular architecture-properties relationships by combination of techniques: molecular weight determination by dilute-solution viscometry and thermal transition by DSC the results are shown in Table 5.6. Also, the "*in vitro*" hydrolytic biodegradability of the films was studied as an indication of their potential use in biomedical applications.

5.4.1 Molecular Weight Determinations of High Molecular Weight PLL by Dilute-Solution Viscometry

The intrinsic viscosity [η] values of the PLLs were obtained from their reduced and inherent viscosity-concentration plots. The results obtained for determining [η] and $\overline{M}_v$ by Mark-Houwink Sakurada equations are summarized in Table 5.6. From the dilute-solution viscometry results, it was found that star-shaped PLLs exhibited lower [η] and $\overline{M}_v$ than those of linear PLL at same molecular weight ($\overline{M_n}$), supportive of the expected star-shaped structure. This is due to the fact that intrinsic viscosity reflects the chain conformation of the polymer in dilute solution. The star-shaped PLL occupies a smaller hydrodynamic volume in solution than the linear PLL at the same molecular weight.

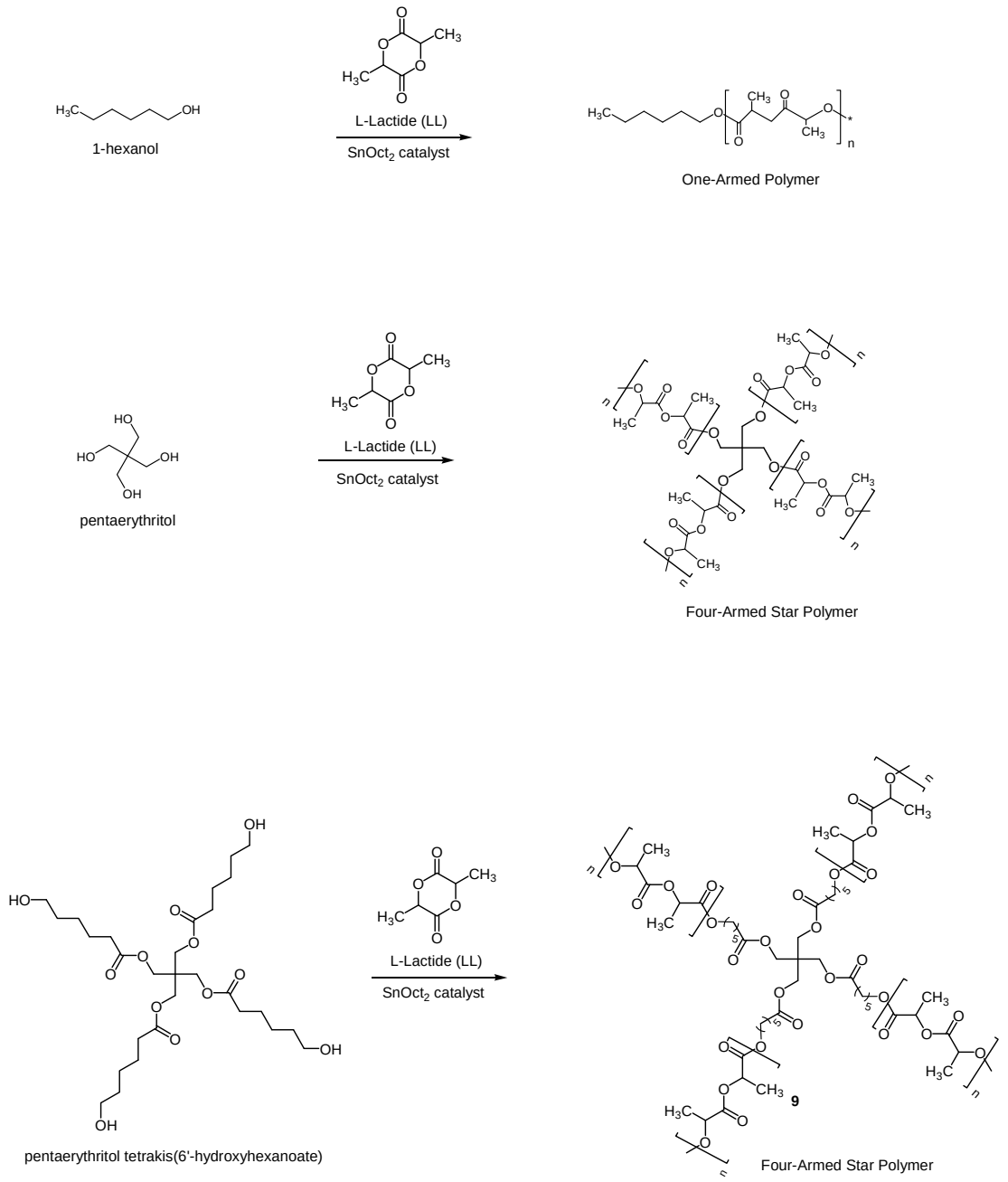

Figure 5.18 Polymerization of L-lactide using (a) 1-hexanol (b) PTOL and (c) pentaerythritol tetrakis(6'-hydroxyhexanoate) as initiators**.**

Table 5.6 The results of high molecular weight PLL homopolymer with different molecular architectures.

Polymer	**PLL_1-hexanol**		**PLL_PTOL**		**PLL_macroinitiator**	
Catalyst (mole %)	$SnOct_2$ (0.1)		$SnOct_2$ (0.1)		$SnOct_2$ (0.1)	
Initiator (mole %)	1-hexanol		PTOL		Macroinitiator	
Monomer : Initiator (mole %)	100 : 1		100 : 1		100 : 1	
Temperature (ºC) ***and Time*** (hr)	120ºC, 48 hr		120ºC, 48 hr		120ºC, 48 hr	
% yield (purified)	94.9		93.4		91.5	
Physical Appearance (crude)	white solid		white solid		white solid	
Physical Appearance (purified)	white solid		white solid		white solid	
Molecular weight (g $mole^{-1}$)						
$\overline{M}_{n,Theory}$	15,114		14,843		15,005	
Dilute-Solution Viscometry						
[η] in $CHCl_3$ at 25ºC (dl/g)	0.42		0.36		0.29	
$\overline{M}_v$	8,925		7,355		5,456	
Thermal Properties						
DSC	1st run	2nd run	1st run	2nd run	1st run	2nd run
T_g (ºC)	-	48.0	-	53.2	-	47.8
T_c, onset (ºC)	100.7	84.4	100.2	100.6	99.6	91.2
peak (ºC)	105.7	88.3	104.7	108.0	102.3	98.7
Heat of Fusion (J/g)	13.1	28.8	5.6	21.9	14.6	13.2
T_m, onset (ºC)	164.5	160.3	153.4	152.4	147.8	149.5
peak (ºC)	170.0	167.3	158.0	157.0	155.3	154.0
Heat of Fusion (J/g)	56.6	52.6	48.0	42.8	45.6	49.7
Degree of Crystallinity (%)	46.5	87.0	57.3	69.1	64.3	67.2

5.4.2 Thermal Characterization of High Molecular Weight PLL by DSC

Thermal properties of linear and star-shaped PLL were characterized by DSC. All samples were measured between 0 to 200ºC at the heating rate of 10ºC/min under dry nitrogen atmosphere. The thermal properties values are shown in Tables 3.6 and DSC thermograms for first and second heating run are compared in Figures 5.19-5.20. The degree of crystallinity (X_c) of PLLs was determined from the enthalpy of melting using the equation (3.6);

$$X_c\,(\%) \;=\; \frac{\Delta H_m \;+\; \Delta H_c}{\Delta H_m{}^{o}} \;\times\; 100 \qquad \text{……..(5.6)}$$

where ΔH_m is the apparent enthalpy of each sample and $\Delta H_m{}^o$ is the extrapolated value enthalpy corresponding of a 100% crystalline PLL, 93.6 J/g. ΔH_c is the apparent enthalpy of crystallization of each sample.

The DSC thermograms 1st run as showed that all PLL samples did not exhibit a glass transition (T_g) peak but did show crystallization (T_c) and melting (T_m) peaks. This was due to their thermal histories. In contrast, the DSC thermograms 2nd run all exhibited T_g, T_c and T_m transitions since all samples has been quenched from their melt states. Consequently very little crystallinity was present in the samples prior to the second heating scan. It was found that the T_g of the linear PLL was lower than the star-shaped PLL synthesized from PTOL. This was due to the effect of chain microstructure. The higher T_g of the star-shaped PLL showed that branching hinders segmental motion.

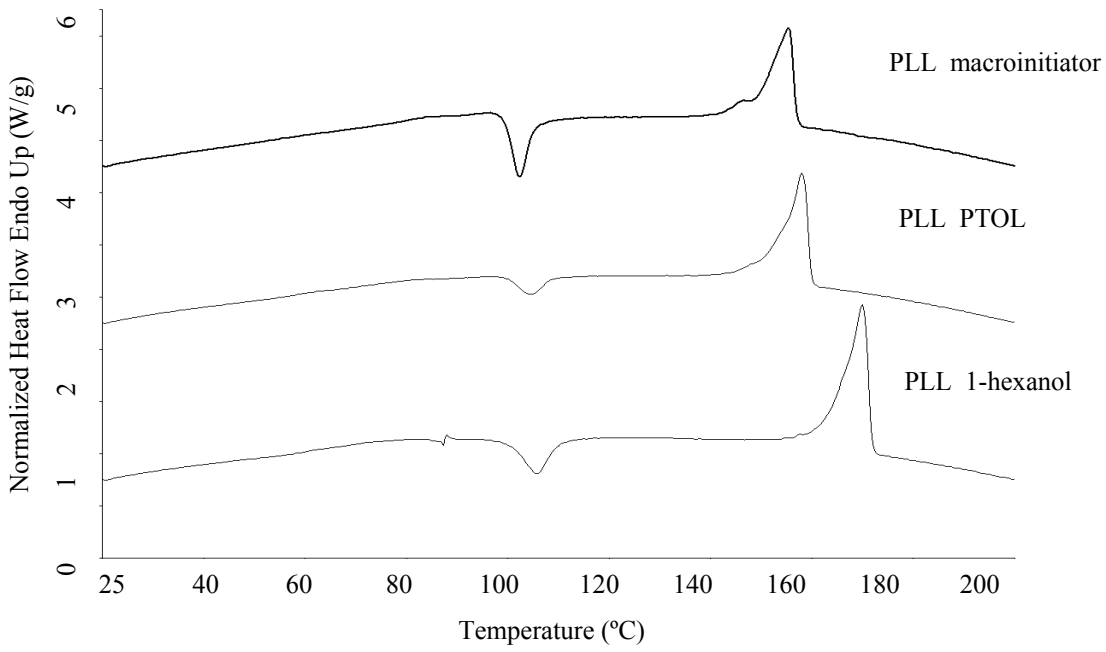

Figure 5.19 Comparison of the DSC thermograms 1st run of the linear and star- shaped PLLs homopolymer.

.

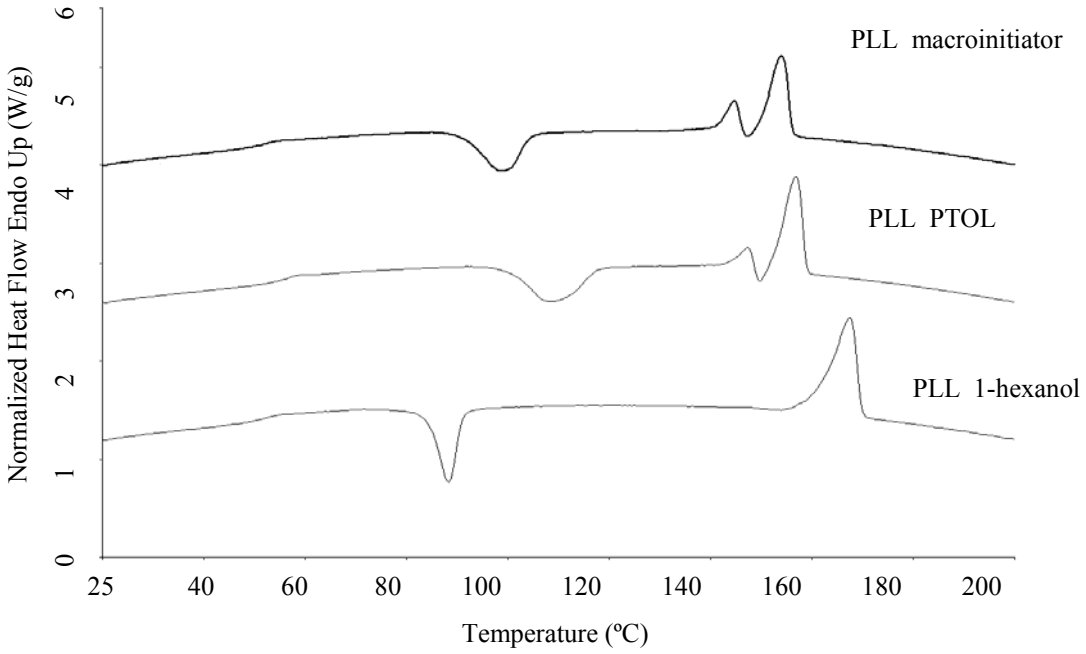

Figure 5.20 Comparison of the DSC thermograms 2nd run of the linear and star- shaped PLLs homopolymer.

.

It was also observed that the star-shaped PLLs possessed lower melting points and degrees of crystallinity than the linear PLL, which could be attributed to crystal imperfections mainly due to the short chain lengths of the star-shaped polymers arms. It can also be seen clearly that the T_c of linear PLL is lower than the star-shaped PLLs, attributable to relatively slow crystallization. The globular structures of the star-shaped PLLs decreased the intermolecular interactions and the number of molecular conformations, which facilitated crystallization. Meanwhile, it is noted that

the PLLs have two melting peaks resulting from differences in crystallite size and/or shape. These DSC results indicate that the thermal properties and crystallinity are affected when branching point are introduced into the polymer.

5.5 *In Vitro* Hydrolytic Biodegradation Studies of High molecular weight PCL and PLL

Linear and star-shaped PCL and PLL films were hydrolyzed in order to study the effects of molecular architectures on the *in vitro* hydrolytic biodegradation. This experiment was selected to provide information about the effect of polymer molecular architecture on the degradation pathway and properties change. The hydrolysis was performed in phosphate buffer saline (PBS) at pH 7.40±0.01 as an immersion medium at body temperature (37±1.0ºC) for 21 weeks. After designated time interval (1, 2, 3, 5, 7, 9, 11, 13, 15, 17 and 21 week), three bottles with different molecular architecture were taken out from the incubator. The film samples were then filtered off, washed carefully with deionized water and dried to constant weight in vacuum oven at room temperature. Normally, the biodegradation of the polymer chain is dependent on the molecular weight, molecular architecture, % crystallinity and polymer environment [15, 18]. The high molecular weight linear and star-shaped PCLs and PLLs use for *in vitro* hydrolytic degradation study are synthesized and characterized as shown in Tables 5.7 and 5.8 respectively.

Table 5.7 The results of the high molecular weight PCLs with different molecular architectures use for *in vitro* hydrolytic degradation study.

Polymer	PCL_1-hexanol	PCL_PTOL	PCL_macroinitiator
Amount of Polymer (g)	25	25	25
Catalyst (mole%)	$SnOct_2$ (0.1)	$SnOct_2$ (0.1)	$SnOct_2$ (0.1)
Initiator (mole%)	1-hexanol	PTOL	Macroinitiator
Monomer : Initiator (mole%)	100 : 0.005	100 : 0.005	100 : 0.005
Temperature (ºC) ***and Time*** (hr)	120ºC, 72 hr	120ºC, 72 hr	120ºC, 72 hr
% yield (after reprecipitation)	97.0	96.0	97.5
Physical Appearance (crude)	white solid	white solid	white solid
Physical Appearance (purified)	white solid	white solid	white solid
Molecular weight (g mole^{-1})			
GPC			
$\overline{M}_n$	28,400	34,520	31,710
$\overline{M}_w$	89,600	79,730	72,200
$\overline{M}_v$	76,120	79,730	72,200
Dilute-Solution Viscometry			
$[\eta]$ in THF at 30°C (dl/g)	1.52	1.45	1.42
$\overline{M}_v$	128,493	120,616	117,905

Table 5.8 The results of the high molecular weight PLLs with different molecular architectures use for *in vitro* hydrolytic degradation study.

Polymer	PLL_1-hexanol	PLL_PTOL	PLL_macroinitiator
Amount of monomer (g)	25	25	25
Catalyst (mole%)	$SnOct_2$ (0.1)	$SnOct_2$ (0.1)	$SnOct_2$ (0.1)
Initiator (mole%)	1-hexanol	PTOL	Macroinitiator
Monomer : Initiator (mole%)	100 : 0.005	100 : 0.005	100 : 0.005
Temperature (ºC) ***and Time*** (hr)	120ºC, 72 hr	120ºC, 72 hr	120ºC, 72 hr
% yield (after reprecipitation)	97.5	96.7	97.0
Physical Appearance (crude)	white solid	white solid	white solid
Physical Appearance (purified)	white solid	white solid	white solid
Molecular weight (g $mole^{-1}$) *Dilute-Solution Viscometry*			
$[\eta]$ in $CHCl_3$ at 25ºC (dl/g)	2.84	2.94	2.71
$\overline{M}_v$	123,609	129,307	116,107

The physical appearance of all PCL and PLL films after *in vitro* hydrolytic biodegradation and drying in vacuum oven at room temperature until constant weight was observed. It was found that both linear and star-shaped PCL films were still translucent and flexible during the *in vitro* biodegradation time. In contrast, linear and star-shaped PLL films were transparent and rigid during weeks 1-5 and change from transparent to opaque after week 5. The star-shape PLL_macroinitiator films started to crack in week 15, followed by star-shape PLL_PTOL in week 21.

5.5.1 Weight Loss Profiles

After vacuum drying to constant weight, their % weight retention and % weight loss were calculates as follows:

$$\%\,\text{weight retention} = \frac{W_f \times 100}{W_0}$$

$$\%\,\text{weight loss} = 100 - \%\,\text{weight retention}$$

where W_0 = initial weight of sample and W_f = final weight of sample

The weight, % weight loss, % weight retention and pH of linear and star-shaped PCLs and PLLs immersed in PBS medium at 37±1.0ºC were calculated and recorded as shown in Tables 5.9-5.14.

Table 5.9 Weight, % weight loss, % weight retention and pH of PCL_1-hexanol immersed in PBS medium at 37±1.0ºC.

Time (weeks)	Initial weight ±0.0001g	Final weight ±0.0001g	% weight loss ±0.1%	% weight retention ±0.1%	pH ±0.01
0	0.0157	0.0157	0.0	100.0	7.40
1	0.0140	0.0140	0.0	100.0	7.38
2	0.0136	0.0136	0.0	100.0	7.40
3	0.0142	0.0142	0.0	100.0	7.39
5	0.0144	0.014	0.0	100.0	7.38
7	0.0143	0.0143	0.0	100.0	7.39
9	0.0146	0.0146	0.0	100.0	7.37
11	0.0140	0.0140	0.0	100.0	7.38
13	0.0141	0.0141	0.0	100.0	7.38
15	0.0144	0.0144	0.0	100.0	7.39
17	0.0140	0.0140	0.0	100.0	7.41
21	0.0135	0.0135	0.0	100.0	7.39

Table 5.10 Weight, % weight loss, % weight retention and pH of PCL_PTOL immersed in PBS medium at 37±1.0ºC.

Time (weeks)	Initial weight ±0.0001g	Final weight ±0.0001g	% weight loss ±0.1%	% weight retention ±0.1%	pH ±0.01
0	0.0157	0.0157	0.0	100.0	7.40
1	0.0142	0.0142	0.0	100.0	7.38
2	0.0155	0.0155	0.0	100.0	7.40
3	0.0145	0.0145	0.0	100.0	7.37
5	0.0139	0.0139	0.0	100.0	7.39
7	0.0140	0.0140	0.0	100.0	7.39
9	0.0145	0.0145	0.0	100.0	7.38
11	0.0146	0.0146	0.0	100.0	7.38
13	0.0136	0.0136	0.0	100.0	7.38
15	0.0147	0.0147	0.0	100.0	7.38
17	0.0157	0.0157	0.0	100.0	7.42
21	0.0145	0.0145	0.0	100.0	7.41

Table 5.11 Weight, % weight loss, % weight retention and pH of PCL_macroinitiator immersed in PBS medium at 37±1.0ºC.

Time (weeks)	Initial weight ±0.0001g	Final weight ±0.0001g	% weight loss ±0.1%	% weight retention ±0.1%	pH ±0.01
0	0.0156	0.0156	0.0	100.0	7.40
1	0.0146	0.0146	0.0	100.0	7.36
2	0.0132	0.0132	0.0	100.0	7.40
3	0.0151	0.0151	0.0	100.0	7.40
5	0.0152	0.0152	0.0	100.0	7.37
7	0.0141	0.0141	0.0	100.0	7.40
9	0.0150	0.0150	0.0	100.0	7.39
11	0.0137	0.0137	0.0	100.0	7.38
13	0.0152	0.0152	0.0	100.0	7.39
15	0.0141	0.0141	0.0	100.0	7.37
17	0.0140	0.0140	0.0	100.0	7.41
21	0.0146	0.0146	0.0	100.0	7.38

Table 5.12 Weight, % weight loss, % weight retention and pH of PLL_1-hexanol immersed in PBS medium at 37±1.0ºC.

Time (weeks)	Initial weight ±0.0001g	Final weight ±0.0001g	% weight loss ±0.1%	% weight retention ±0.1%	pH ±0.01
0	0.0149	0.0149	0.0	100.0	7.40
1	0.0157	0.0154	1.0	99.0	7.36
2	0.0151	0.0145	1.7	98.3	7.32
3	0.0139	0.0133	3.1	96.7	7.23
5	0.0143	0.0136	4.2	95.8	7.10
7	0.0145	0.0137	5.2	94.8	7.11
9	0.0164	0.0154	6.1	93.9	6.89
11	0.0154	0.0141	8.1	91.9	6.60
13	0.0167	0.0152	8.6	91.4	6.54
15	0.0157	0.0142	9.8	90.2	6.38
17	0.0142	0.0125	10.7	89.3	6.12
21	0.0154	0.0134	13.2	86.8	5.97

Table 5.13 Weight, % weight loss, % weight retention and pH of PLL_PTOL immersed in PBS medium at 37±1.0ºC.

Time (weeks)	Initial weight ±0.0001g	Final weight ±0.0001g	% weight loss ±0.1%	% weight retention ±0.1%	pH ±0.01
0	0.0165	0.0165	0.0	100.0	7.40
1	0.0155	0.0150	1.9	98.1	7.35
2	0.0154	0.0147	2.9	97.1	7.29
3	0.0156	0.0149	4.2	95.8	7.11
5	0.0172	0.0163	5.4	94.6	7.00
7	0.0164	0.0154	6.4	93.6	6.80
9	0.0152	0.0144	7.7	92.3	6.52
11	0.0164	0.0148	9.1	90.9	6.36
13	0.0169	0.0151	9.6	90.4	6.30
15	0.0163	0.0145	10.0	90.0	6.15
17	0.0157	0.0137	11.8	88.2	5.92
21	0.0155	0.0133	14.6	85.4	5.68

Table 5.14 Weight, % weight loss, % weight retention and pH of PLL_macroinitiator immersed in PBS medium at 37±1.0ºC.

Time (weeks)	Initial weight ±0.0001g	Final weight ±0.0001g	% weight loss ±0.1%	% weight retention ±0.1%	pH ±0.01
0	0.0149	0.0149	0.0	100.0	7.40
1	0.0154	0.0147	2.7	97.3	7.35
2	0.0163	0.0153	3.4	96.6	7.26
3	0.0158	0.0146	5.6	94.4	7.11
5	0.0172	0.0158	6.2	93.2	6.92
7	0.0187	0.0171	7.6	92.4	6.78
9	0.0171	0.0153	10.3	89.7	6.52
11	0.0170	0.0149	12.9	87.1	6.21
13	0.0162	0.0140	13.7	86.3	5.98
15	0.0157	0.0134	14.9	85.1	5.74
17	0.0162	0.0137	16.1	83.9	5.43
21	0.0170	0.0141	18.4	81.6	5.18

The weight, %weight retention and %weight loss of linear and star-shaped PCLs and PLLs are shown in Tables 5.9-5.14. The corresponding %weight loss and %weight retention profiles of linear and star-shaped PLLs are shown in Figures 5.21-5.22.

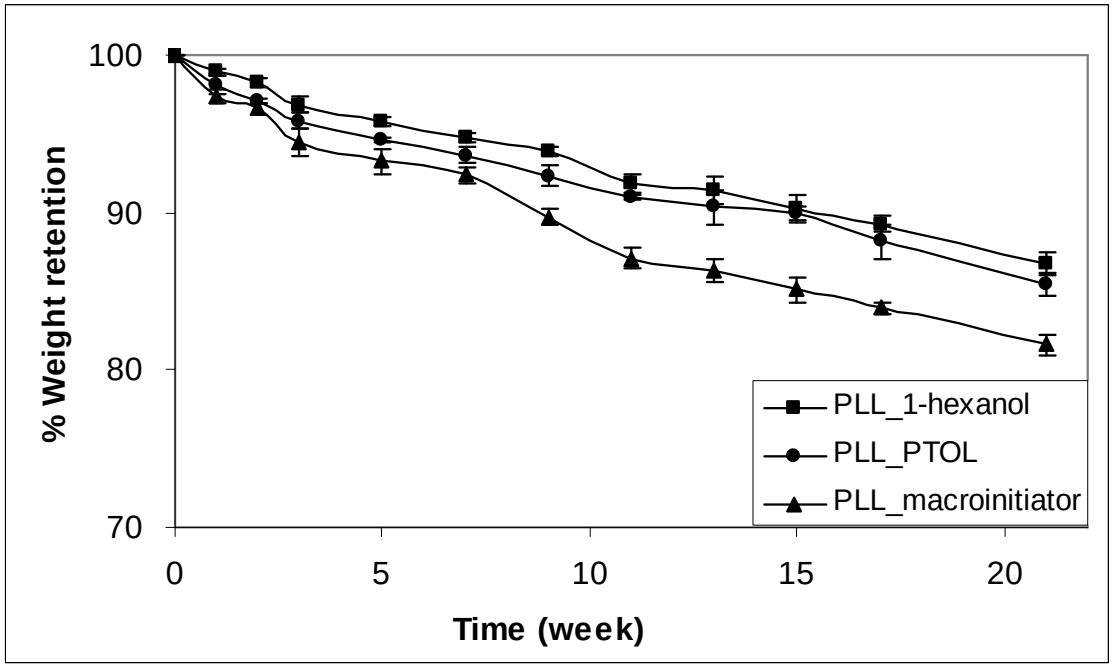

Figure 5.21 Comparison of % weight retention of linear and star-shape PLLs during of the period of the *in vitro* biodegradation experiments.

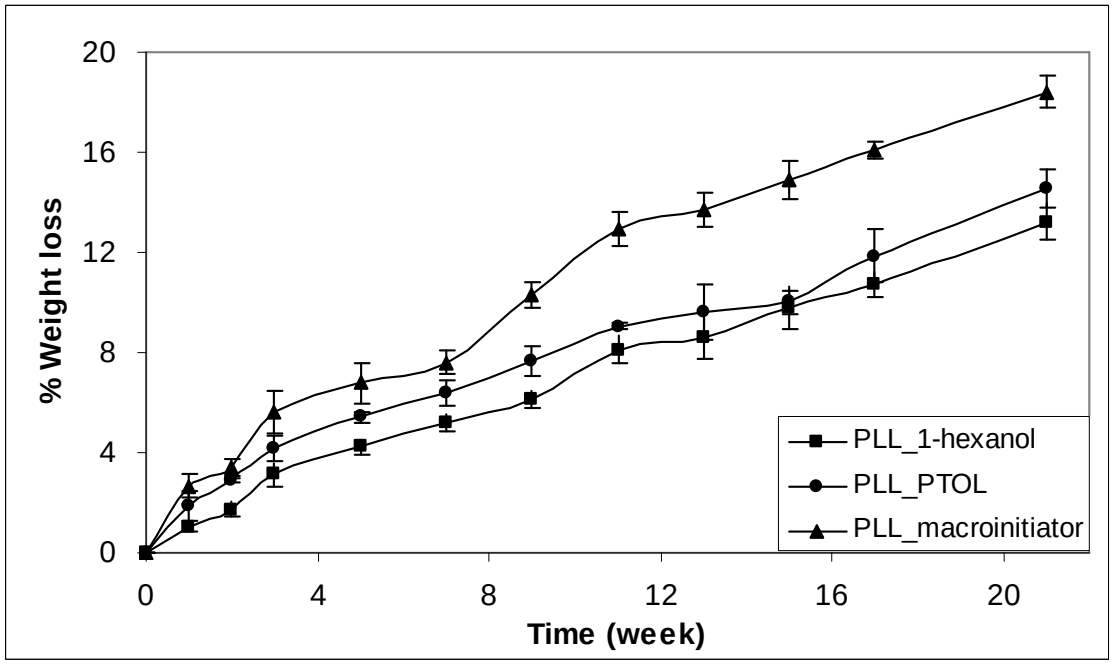

Figure 5.22 Comparison of % weight loss of linear and star-shape PLLs during of the period of the *in vitro* biodegradation experiments.

From the results obtained in Tables 5.9-5.11, all the linear and star-shaped PCL films were not changed weight during *in vitro* biodegradation periods (21 weeks) due to the fact that PCL has a long degradation time (approximately 3 years) with high crystallinity. In contrast, star-shaped PLL showed a faster degradation rate than linear PLL seems to be due to star-shaped polymers have a different entanglement structure and possess a higher density of chain-end than linear chain of comparable molecular weight. This could be affect mechanical properties and degradation behaviors.

Although chemical microstructure is the dominant factor for hydrolytic degradation, matrix morphology (% crystallinity and crystallize orientation) is also important. It could be seen that the biodegradation rate of star-shaped PLL_macroinitiator is faster than star-shaped PLL_PTOL, which should be ascribed to the shorter and longer chain in imperfection star-shaped of PLL_PTOL.

The biodegradability of semi-crystalline polymers might be depended on the characteristics of the amorphous region. The proposed degradation proceeds through two main stages: the first stage takes place in the amorphous region; the second in the crystalline region. Within the first stage, because of the molecules in the amorphous region of a polymer are loosely packed, they are more susceptible to attack by solvents than those in the crystalline region and the tie-chain segments in the amorphous regions degrade into fragments. This chain scission results in a lesser degree of entanglement of long-chain molecules located in the amorphous regions. Therefore, the remaining un-degraded chain segments can move and reorganize themselves from a disordered to an order state. Further crystallization is induced and increase in the heat of fusion is thus observed. Therefore, two competing processes hydrolysis and induced crystallization were observed in the hydrolytic degradation. In addition, the weight loss of the polymer samples first occurs in the amorphous regions can lead to an apparent increase in crystallinity that can be confirmed all of star-shaped PLL films were changed into opaque white solid during weeks 15-21. When all of the amorphous regions have been removed by the hydrolysis, the second stage of degradation starts.

For the degradation occurred, the polymer should have hydrolytically unstable functional groups, *e.g.,* ester groups. When these biodegradable polymers are placed in contact with the physiological environment, water penetrates the polymer matrix and facilitates the hydrolytic chain cleavages, leading to biodegradation. The degradation of these PLLs is believed to be a random chain scission which may take place through hydrolysis in the main chain, side chain or both. Normally, the biodegradability of the polymer chain is dependent on the molecular weight, molecular architecture, % crystallinity and polymer environment. In this experiment all factors were fixed except molecular architectures. From the results obtained, the biodegradation rate of star-shaped PLL_macroinitiator is faster than PLL_PTOL and linear PLL. The higher degradation rate of star-shaped PLLs seems to be due to the higher density of chain-end compared with linear PLL.

5.5.2 pH Stability of Phosphate Immersion Medium

The pH of PBS immersion medium was monitored throughout the period of the experiment. No attempt was made to re-adjust the pH to 7.40 since it was of interest to note how the pH changed. It was found that the initially adjusted pH of 7.40 decreased with time, as showed in Tables 5.9-5.14 and Figure 5.23. The simple hydrolysis reaction can be acid-catalyzed in the event that the new carboxylic acid end groups formed causes the pH of the medium to drop below 7. When these generated groups act as a catalyst, the hydrolytic degradation is called an autocatalytic process.

From the pH profile, two phases can be observed in this plot. In the first phase, the pH of the immersion medium decreased slowly due to the most acid degradation products was tapped inside the polymer matrix. In the second phase, the pH decreases dramatically because the tapped acid degradation products are released. Normally, the third phase may be occurred in the longer times.

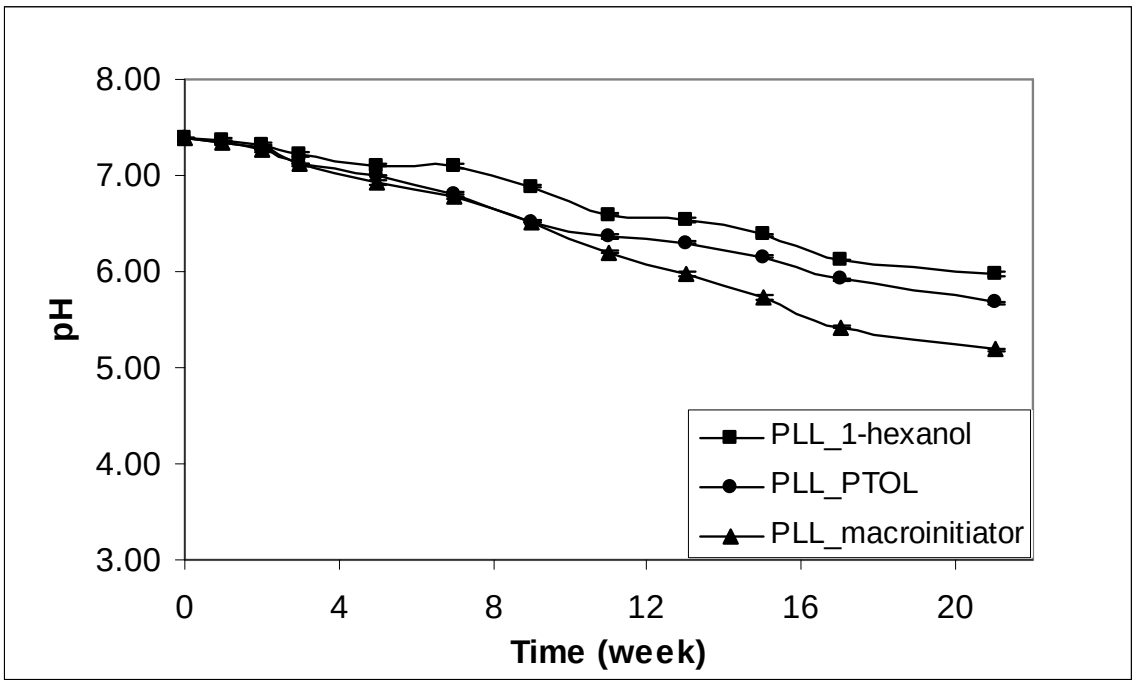

Figure 5.23 Comparison of pH of linear and star-shape PLL during of the period of the *in vitro* biodegradation experiments.

The star-shaped PLLs were decreased of pH values than linear PLL because of star-shaped had more chain ends and short chain length due to disordered polymer chains and less chain entanglements. The hydrolysis continued inside the hydrated polymer matrix so that the molecular weight of the polymer continuously decreases. Also linear polymer chain can rearrange itself from a disordered to an order state and gave higher crystallinity and strength. The degradation prefers occur in amorphous region more than crystalline region due to water molecules can penetrate easy in amorphous region. From this reason, star-shaped PLL films degraded faster than linear PLL film.

5.5.3 Morphology Determination by DSC

Thermal characterization of linear and star-shaped PLLs immersed in PBS medium at 37±1.0ºC was accomplished by DSC. All samples were measured between 0 to 200ºC at the heating rate of 10ºC/min under dry nitrogen atmosphere. The thermal properties values are shown in Tables 5.15-5.20 and DSC thermograms for first and second heating run are compared in Figures 5.24-5.29.

From DSC data first and second run, all PLL samples possess T_g, T_c and T_m. The degree of crystallinity (X_c) of PLLs was determined from the enthalpy of melting using the equation 5.6. For the results obtained, the % crystallinity of all linear and star-shaped PLL films increased during 1-21 weeks indicated to the molecules in the amorphous region of a polymer were crystallized slowly in immersion medium. The degradation time in weeks 1-21, % crystallinity of star-shaped PLLs are all lower than that linear due to the amorphous region of star-shape PLL is higher. The increasing in amorphous with branching is attributed to shorter chain length and the increase in the number of free chain end, which probably disrupts the orderly fold pattern of the crystal [19].

DSC thermograms 1st run as showed that all PLL samples did not exhibit a T_c but did show melting (T_m) peaks. This was due to their thermal histories. DSC curves second heating run for linear and star-shaped PLL films are shown in Figures 5.27-5.29. It was found that the T_c and T_m of all PLL films increased during 1-5 weeks, while in weeks 7-21 the T_c and T_m decreased. Earliest stage of *in vitro* biodegradation, the low degradation rate of these PLLs occurred with the molecules

in the amorphous region were crystallized at the same time. As the time increase, the degradation rate increased, which also could be attributed to water penetrates the polymer matrix and facilitates the hydrolytic chain cleavages.

The double melting peaks were observed for the hydrolyzed polymer films, suggesting that two kinds of different fine crystal structures existed in PCL as shown in Figures 5.21-5.23 and melting point decreased with the decrease of crystallite size.

Table 5.15 DSC results for first run of linear PLL_1-hexanol immersed in PBS medium at 37±1.0ºC.

PLL_1-hexanol (week)	DSC (1st run)								
	T_g,onset (ºC)	T_g,half (ºC)	T_c,onset (ºC)	T_c,peak (ºC)	ΔH_c (J/g)	T_m,onset (ºC)	T_m,peak (ºC)	ΔH_m (J/g)	X_c (%)
0	-	-	-	-	-	148.0	157.2	24.4	26.1
1	-	-	-	-	-	147.5	157.3	23.5	25.1
2	-	-	-	-	-	152.9	161.5	27.8	29.7
3	-	-	-	-	-	153.8	161.67	25.6	27.4
5	-	-	-	-	-	151.9	161.7	26.6	28.5
7	42.0	47.5	-	-	-	153.2	164.0	35.0	37.4
9	-	-	-	-	-	151.4	165.0	22.5	24.0
11	48.0	50.2	-	-	-	156.4	165.0	41.3	44.2
13	45.8	49.6	-	-	-	156.8	162.8	39.5	42.2
15	-	-	-	-	-	159.0	163.2	39.7	42.4
17	-	-	-	-	-	158.0	164.7	37.8	40.4
21	-	-	-	-	-	156.8	162.2	40.9	43.7

Table 5.16 DSC results for second run of linear PLL_1-hexanol immersed in PBS medium at 37±1.0ºC.

PLL_1-hexanol (week)	DSC (2nd run)								
	T_g,onset (ºC)	T_g,half (ºC)	T_c,onset (ºC)	T_c,peak (ºC)	ΔH_c (J/g)	T_m,onset (ºC)	T_m,peak (ºC)	ΔH_m (J/g)	X_c (%)
0	46.7	51.0	108.7	120.8	18.0	150.6	159.0	27.0	48.1
1	49.8	52.6	105.6	120.7	23.9	152.8	160.2	27.6	55.0
2	58.1	60.0	110.5	127.3	27.8	156.4	161.8	26.7	58.2
3	57.4	58.7	110.2	125.8	26.7	156.3	162.0	31.1	61.8
5	49.1	52.9	101.6	115.3	31.9	151.8	158.0	27.1	63.1
7	55.7	58.3	107.1	121.2	35.6	155.9	161.3	35.9	76.4
9	50.9	54.0	105.9	118.2	34.0	154.8	161.0	35.8	74.5
11	49.6	52.4	104.9	116.0	35.1	162.2	166.5	35.5	75.5
13	53.9	56.0	103.7	113.8	37.3	153.5	158.5	36.8	79.2
15	51.7	53.7	100.3	108.5	37.1	159.3	163.7	39.9	82.2
17	56.7	58.6	104.6	112.7	35.7	160.5	164.8	37.8	78.6
21	55.7	57.3	97.0	106.0	37.6	156.9	162.3	38.3	81.0

Table 5.17 DSC results for first run of star-shaped PLL_PTOL immersed in PBS medium at 37±1.0ºC.

PLL_ PTOL (week)	DSC (1st run)								
	$T_{g,}$onset (ºC)	$T_{g,}$half (ºC)	$T_{c,}$onset (ºC)	$T_{c,}$peak (ºC)	ΔH_c (J/g)	$T_{m,}$onset (ºC)	$T_{m,}$peak (ºC)	ΔH_m (J/g)	X_c (%)
0	-	-	-	-	-	151.3	161.2	20.8	28.9
1			-	-	-	150.6	160.2	21.1	22.6
2	38.2	43.3	-	-	-	150.5	160.8	23.8	25.4
3	41.6	43.6	-	-	-	150.7	160.2	22.9	24.5
5	-	-	-	-	-	150.1	159.7	18.8	20.0
7	-	-	-	-	-	150.9	162.7	31.0	33.1
9	-	-	-	-	-	154.1	163.5	29.1	31.1
11	49.6	51.6	-	-	-	155.8	163.7	31.2	33.3
13	-	-	-	-	-	151.7	162.2	32.6	34.8
15	52.9	55.2	-	-	-	158.1	164.3	30.0	32.1
17	54.1	56.7	-	-	-	159.0	164.2	32.7	35.0
21	52.9	55.7	-	-	-	159.4	165.2	34.1	36.4

Table 5.18 DSC results for second run of star-shaped PLL_PTOL immersed in PBS medium at 37±1.0ºC.

PLL_PTOL (week)	DSC (2nd run)								
	$T_{g,}$onset (ºC)	$T_{g,}$half (ºC)	$T_{c,}$onset (ºC)	$T_{c,}$peak (ºC)	ΔH_c (J/g)	$T_{m,}$onset (ºC)	$T_{m,}$peak (ºC)	ΔH_m (J/g)	X_c (%)
0	58.9	61.7	118.1	131.2	8.1	155.6	162.5	15.8	25.5
1	60.2	62.2	113.4	130.8	17.5	154.9	161.0	18.6	38.5
2	57.4	59.8	112.8	129.5	16.5	155.3	161.5	19.9	38.9
3	56.2	58.3	111.2	127.3	19.6	155.0	161.7	24.4	46.9
5	45.2	46.1	101.7	118.3	31.7	151.8	158.7	23.3	58.8
7	56.5	58.7	110.3	125.5	28.1	156.4	161.8	28.5	60.5
9	51.1	53.7	109.5	123.8	28.6	156.2	162.3	30.2	62.8
11	50.6	53.8	107.7	121.8	32.0	155.9	161.5	31.0	66.3
13	53.8	55.7	105.2	120.2	36.8	154.4	159.8	34.8	76.5
15	59.7	61.5	108.3	122.7	36.6	155.9	161.0	34.2	75.6
17	59.6	61.5	108.3	121.2	37.1	156.0	160.8	35.9	78.0
21	58.9	60.9	107.1	116.8	33.1	155.3	159.7	35.5	73.4

Table 5.19 DSC results for first run of star-shaped PLL_macroinitiator immersed in PBS medium at 37±1.0ºC.

PLL_macro initiator (week)	DSC (1st run)								
	$T_{g,}$onset (ºC)	$T_{g,}$half (ºC)	$T_{c,}$onset (ºC)	$T_{c,}$peak (ºC)	ΔH_c (J/g)	$T_{m,}$onset (ºC)	$T_{m,}$peak (ºC)	ΔH_m (J/g)	X_c (%)
0	-	-	-	-	-	147.7	158.8	21.0	22.5
1	-	-	-	-	-	147.9	157.7	24.2	25.8
2	42.4	45.7	-	-	-	156.9	163.8	22.1	23.6
3	47.2	46.8	-	-	-	156.2	163.5	23.5	25.1
5	-	-	-	-	-	153.8	161.3	23.5	25.2
7	42.4	45.9	-	-	-	158.3	164.2	28.6	30.5
9	49.3	51.3	-	-	-	158.5	165.2	31.7	33.8
11	-	-	-	-	-	159.1	164.5	30.5	32.6
13	44.5	48.5	-	-	-	157.5	162.5	33.2	35.4
15	-	-	-	-	-	159.5	164.3	31.9	34.1
17	52.7	54.7	-	-	-	160.3	164.5	33.0	35.3
21	-	-	-	-	-	159.1	164.3	34.3	36.6

Table 5.20 DSC results for second run of star-shaped PLL_macroinitiator immersed in PBS medium at 37±1.0ºC.

PLL_macro initiator (week)	DSC (2nd run)								
	$T_{g,}$onset (ºC)	T_g,half (ºC)	$T_{c,}$onset (ºC)	$T_{c,}$peak (ºC)	ΔH_c (J/g)	$T_{m,}$onset (ºC)	$T_{m,}$peak (ºC)	ΔH_m (J/g)	X_c (%)
0	60.4	62.6	112.6	126.2	23.5	155.0	160.5	25.2	52.1
1	46.8	50.2	103.0	116.7	21.9	151.4	158.0	27.8	53.1
2	58.4	60.4	111.4	125.7	25.9	157.2	162.5	29.1	58.7
3	57.8	59.8	110.6	127.2	27.6	157.2	162.7	27.8	59.2
5	45.8	47.1	100.1	113.7	29.7	151.4	158.0	24.6	58.0
7	56.7	58.8	107.9	120.5	32.8	156.4	161.5	33.3	70.6
9	49.8	53.6	107.6	119.5	30.6	156.4	161.3	31.8	66.7
11	47.8	52.5	107.1	118.5	30.5	156.3	161.3	31.9	66.8
13	54.0	56.1	103.9	113.8	33.8	153.5	158.5	36.6	75.2
15	59.6	61.4	107.5	116.5	32.9	155.6	160.0	34.1	71.8
17	59.7	60.7	106.3	113.8	33.7	161.6	166.0	34.2	72.5
21	58.5	60.1	104.7	111.7	37.2	161.3	165.5	36.5	78.7

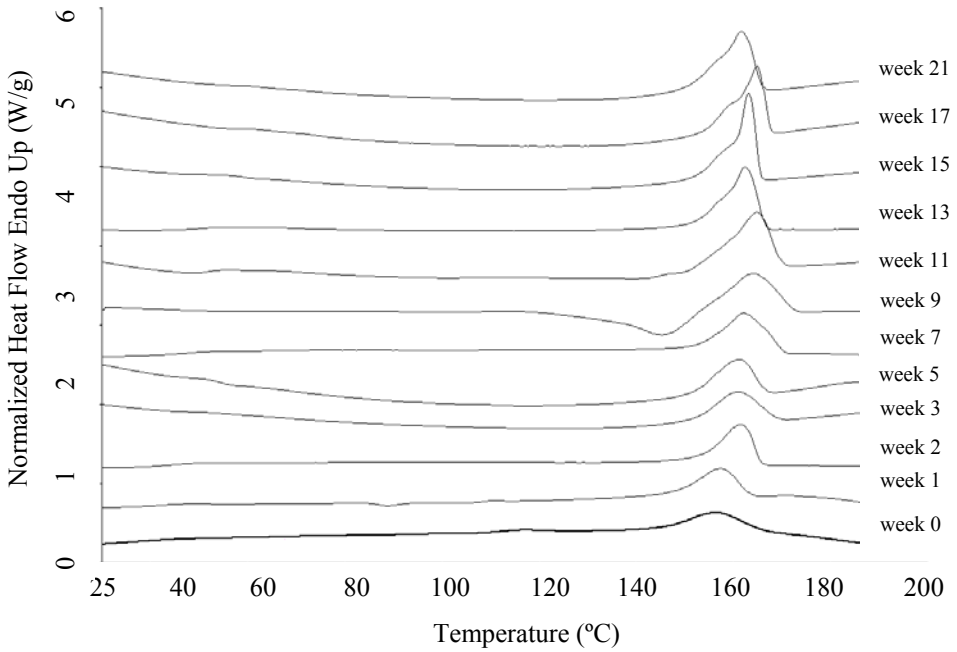

Figure 5.24 Comparison of the DSC thermograms first heating run of PLL_1-hexanol during of the period of the in vitro biodegradation experiments.

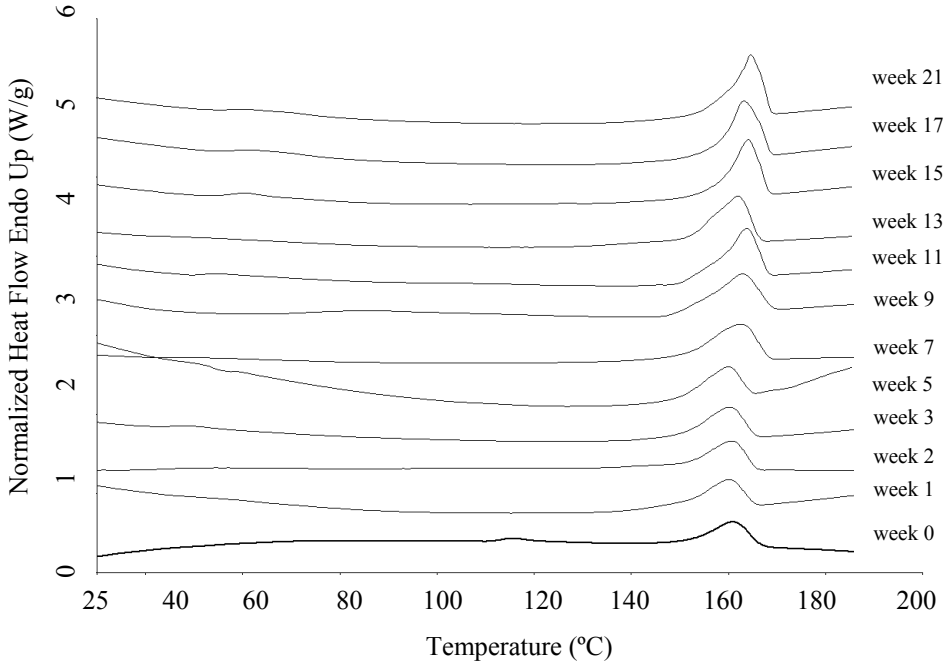

Figure 5.25 Comparison of the DSC thermograms first heating run of PLL_PTOL during of the period of the *in vitro* biodegradation experiments.

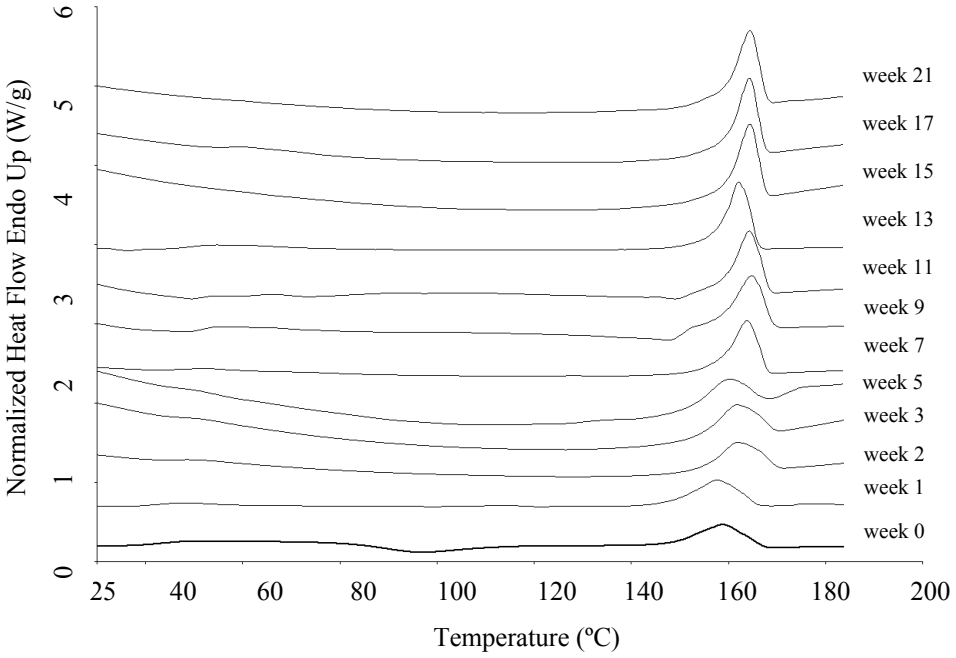

Figure 5.26 Comparison of the DSC thermograms first heating run PLL_macroinitiator during of the period of the *in vitro* biodegradation experiments.

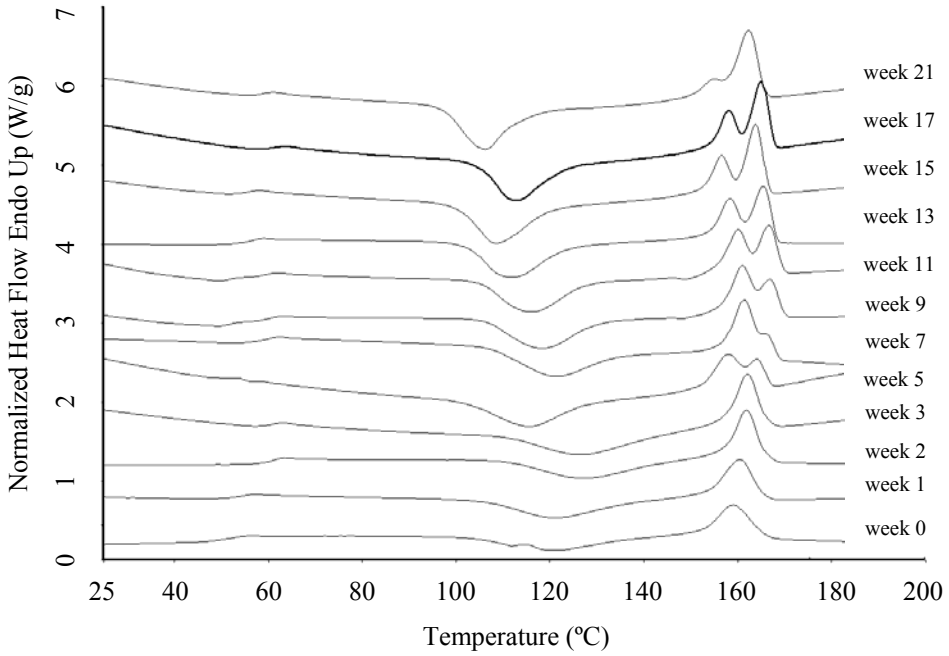

Figure 5.27 Comparison of the DSC thermograms second heating run of PLL_1- hexanol during of the period of the in vitro biodegradation experiments.

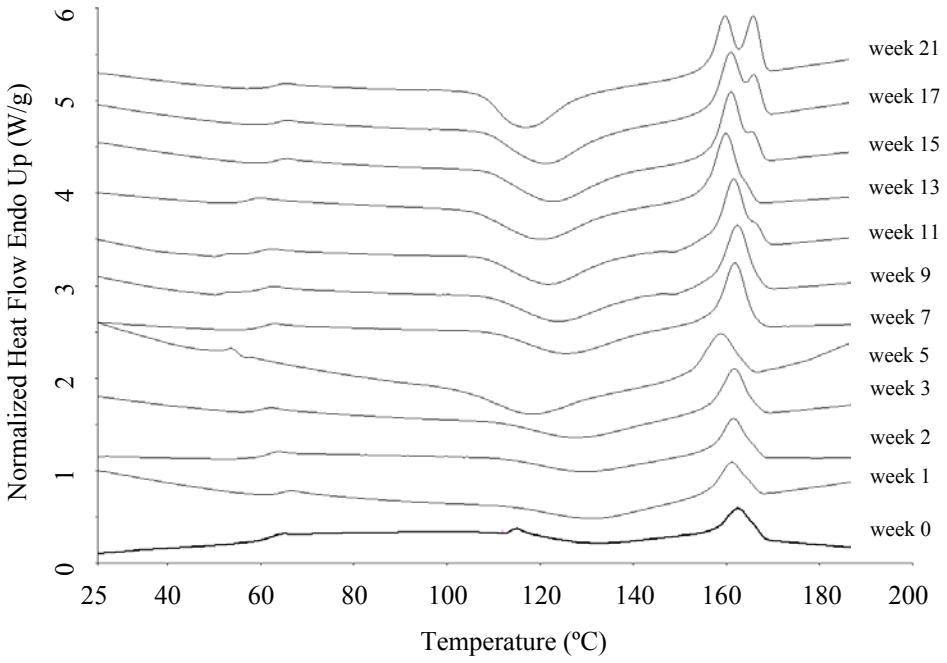

Figure 5.28 Comparison of the DSC thermograms second heating run of PLL_PTOL during of the period of the *in vitro* biodegradation experiments.

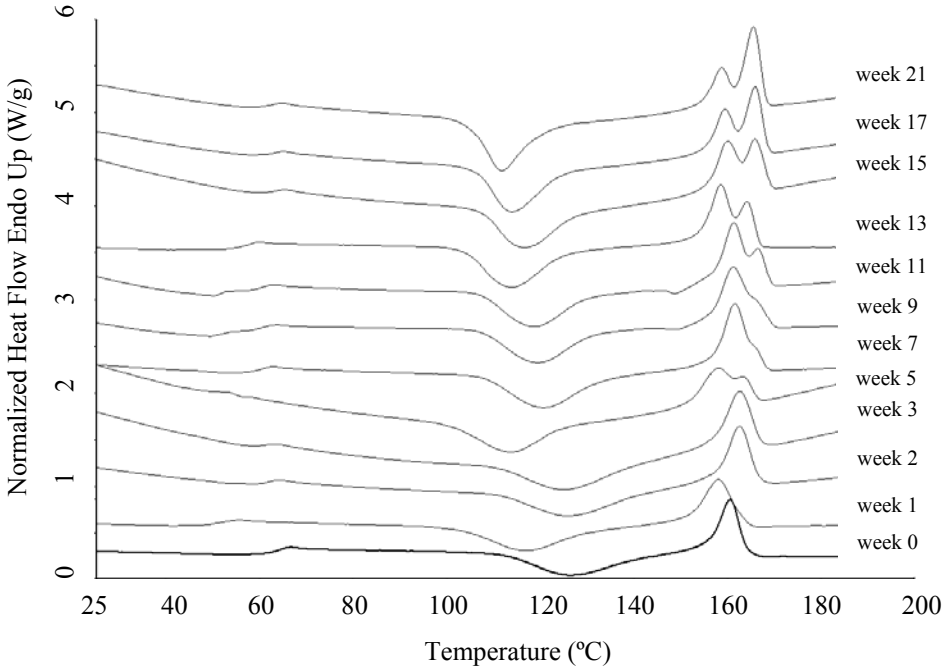

Figure 5.59 Comparison of the DSC thermograms second heating run PLL_macroinitiator during of the period of the *in vitro* biodegradation experiments.

The various stages and processes involved in absorption were described on the following. The first step in hydrolytic degradation process is the absorption of water (hydration) and wetting at the polymer surface. The efficiencies and the rate of these physical processes depend primarily on the hydrophilic and hydrophobic of the polymer and the amount of surface area available for interaction. This is then followed by ester hydrolysis at the surface leading to the formation of micro-defects which facilitate the diffusion of water into the bulk interior of the polymer matrix. The ester hydrolysis occurs preferentially in the amorphous regions where the chains are more loosely packed than in highly-ordered crystalline regions. Then, as hydrolysis precedes the polymer molecular weight decreases until the degradation products are small enough in size to diffuse out the matrix, resulting in mass loss.

5.6 Effect of Molecular Architecture on the Properties of a Biodegradable Terpolyester for Biomedical Applications

It is possible to design the synthetic polymer by controlling the molecular architecture (linear, branched and star-shaped). The synthesis route for poly(L-lactide-*co*-caproplactone-*co*-glycolide) terpolyesters, PLCG 75:20:5 with different molecular architecture in this study as shown in Figure 5.60 was the core-first method where polymer chains were grown directly from an alcohol used as the multifunctional core by ROP. It is worth noticing that the polymer chains are directly functionalized by an end-group which comes from the alcohol. The structure and properties of the resulting polymers were characterized by a combination of analytical techniques: spectroscopic methods (^{1}H-NMR and ^{13}C-NMR), molecular weight methods (GPC and dilute-solution viscometry), thermal analysis methods (DSC and TG), mechanical analysis methods (tensile testing and DMA), rheological analysis methods and *in-vitro* degradation method.

Most of the results are summarized and divided up under the following topics.

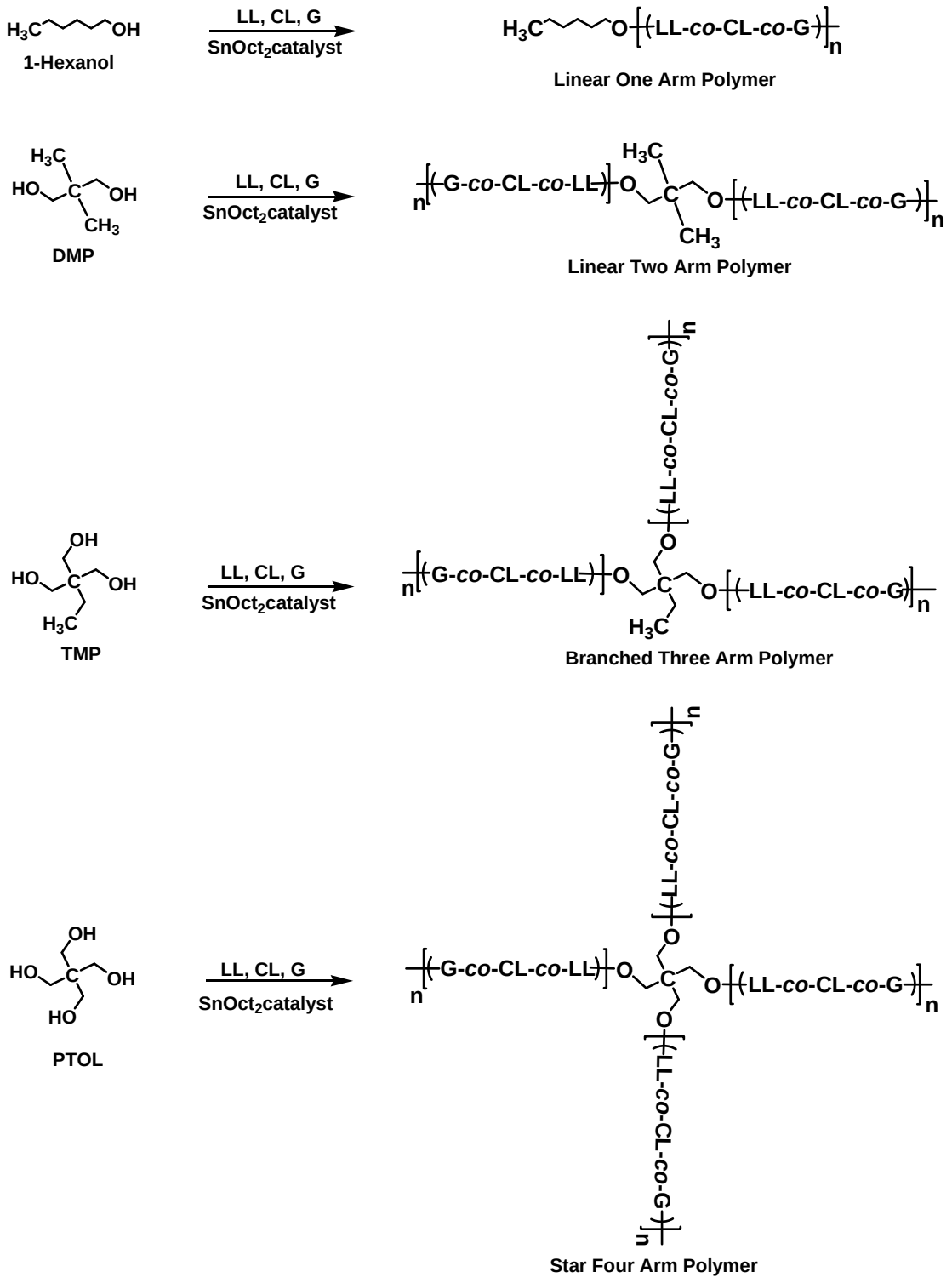

Figure 5.60 Design molecular architectures of poly(LL-*co*-CL-*co*-G) terpolymers using alcohol initiators with different numbers of hydroxyl end-groups.

5.6.1 Influence of monomer to initiator molar ratio ([M]:[I]) on PLCG 75:20:5 Properties

The effects of molar ratios of monomer to initiator, [M]:[I] on the molecular weight and mechanical properties of PLCG 75:20:5 terpolymers were studied. PLCG terpolymers were synthesized by ROP using $SnOct_2$ 0.1 mole % as the catalyst and DMP as the initiator at 120°C for 48 hours. Various molecular weights were carried out with [M]:[I] varying between 100:0.005 and 100:0.5. From both GPC and dilute-solution viscometry results showed that the average molecular weight (M_n, M_w and M_v) and intrinsic viscosity, [η], could be controlled in the range of $M_n \approx 6.9x10^3$-$1.6x10^4$ g mol^{-1} and [η] ≈ 0.57-1.07 dl g^{-1} and the values increased as the initiator concentration decreased. The results indicated that hydroxyl-containing compounds are real initiator. Excess alcohols act as a transesterification agent and caused a drop in the average molecular weight. These results are conformed to both of the mechanistic pathways proposed by Kricheldorf *et al.* and Penczek *et al.*. The tensile mechanical properties of PLCG depended on the polymer molecular weight. The tensile strength and Young's modulus are slightly increased with the polymer molecular weight in the range of $M_n \approx 6.9x10^3$-$1.6x10^4$ g mol^{-1}. From these mentions above, the [M]:[I] ratio affect to polymer molecular weight and its mechanical properties. The higher value of [M]:[I] ratio gave high polymer molecular weight and (tensile) mechanical properties. In the following sections, the [M]:[I] ratios of 100:5 and 100:0.005 were chosen to controlled the low and high molecular weight polymers respectively.

5.6.2 Synthesis of Low Molecular Weight PCLs and PLLs Model Compounds with Different Molecular Architectures

In order to confirm the polymer molecular architecture and study its properties, a series of linear and star-branched low molecular weight poly(ε-caprolactone), PCLs and poly(L-lactide), PLLs were synthesized with structure variation of arm number through ROP of CL and LL respectively in the presence of 0.1 mole% stannous octoate as catalyst. Arm number was varied by using different mono- and multifunctional cores having 1 (1-hexanol), 2 (DMP), 3 (TMP) and 4 (PTOL) hydroxyl groups as initiator. Relatively high amounts of initiators (0.5 mole%) were used in order to obtain low molecular weight ($M_{n,\ cal}$ ≈ 2,000-3,000) polymers for confirming the structure and evaluate the influence of short-chain branched structure on the properties.

Short chain branches and star PCLs and PCLs with different molecular architectures and the same molecular weight were successfully synthesized, as confirmed by dilute solution viscometry, ^{1}H-NMR and DSC analysis. The three- and four-armed PCLs and PLLs have lower intrinsic viscosity, [η], than their linear analog at the same molecular weight (M_n), indicating the expected branched structure. It is due to the branched and star-shaped has a higher segment density within the distance of its radius of gyration and lower hydrodynamic volume than linear polymers. Subsequently, degree of branching of star polymers can be estimated by comparing the mean-square radii with linear polymer. The branched structures contained some arm defects as evidenced on the $g^{1/2}/g'$ values, where g and g' denote the ratios of mean-square radius of gyration and intrinsic viscosity of branched and star-shaped polymers to those of a linear structural reference with similar absolute molecular weight.

The most direct ones to determine the short chain branching content is ^{1}H-NMR. Structural variations among the linear, branched and star-shaped were verified to be precisely controlled as evidenced by ^{1}H-NMR spectra. The methyl groups of 1-hexanol, DMP and TMP initiated polymer were found, except PTOL that has no methyl group in its structure. It was also found that the average number of initiating OH group of branch and star structure, as calculated from the average degree of polymerization per arm (DP_n/Arm) determined experimentally by ^{1}H-NMR, were closed to the theoretical OH functionalities.

Different molecular architectures also result in different thermal behaviors. The thermal analysis by DSC demonstrated that branched and star-shaped PCLs possessed lower melting temperatures (T_m) and degree of crystallinity (X_c) than the linear ones. The reduction in melting point with branching is attributed to the decrease in chain length and, of course, to the increase in the number of free chain ends. This affects the orderly crystalline pattern. Also, the melting peaks of branched and star-shaped PLLs could not be observed. It can ascribe to the relatively slow crystallization rate and the amorphous phase in the sample increased. As would be expected, the short chain branches mostly affect the crystallinity. This offers possibilities to adjust the crystallinity by variation of the arm number (three- and four-arms) and arm length (DP_n/Arm of four-arms < DP_n/Arm of three-arms) and this can be utilized and optimized for each application.

The thermal stability of PCLs and PLLs oligomer showed the one state degradation pattern, which could be ascribed to the homogeneous polymer products obtained from the polymerization. The effect of molecular architecture on the thermal stability of PCLs and PLLs were found that the decomposition temperature (T_d) slightly decreases with increasing the number of hydroxyl groups of the initiator. Thermal properties were clearly affected when branching points were introduced into the polymers.

5.6.3 Synthesis of High Molecular Weight PLCG 75:20:5 with Different Molecular Architectures

To study the effect of molecular architecture on the polymer properties, the high molecular weight linear, branched and star-shaped PLCG 75:20:5 were synthesized by using mono- and multifunctional alcohols (1-hexanol, DMP, TMP and PTOL) with the lowest alcohol concentration (0.005 mole%) as initiator. Three experiments using the same polymerization conditions were synthesized and the results were compared (Set A, B and C). The PLCG terpolymers with different molecular architectures and the same molecular weight were successfully synthesized and characterized as fully as possible in order to underlying the molecular architecture-properties relationships by combination of techniques.

The M_n's values of all terpolymers from GPC results ($M_n \approx$ 8,000-18,000) are lower than the theoretical value that can be explained by another hydroxyl initiation and transesterification reaction may be involved. The degree of branching is often characterized in terms of the branching factor form Mark-Houwink relationship. The ratio $g^{1/2}/g'$ for branched and star-shaped PLCGs yielded value just below 1.00, indicating that the branched and star-shaped PLCGs contained small linear chains or arm defect. It was meant that the arm length of branched and star-shaped PLCGs may be not equal or some hydroxyl groups of TMP or PTOL did not completely react.

From ^{1}H-NMR results showed that final polymer composition was corresponding to the initial monomer feed confirming that the reaction conditions employed were appropriated for the attainment of near-quantitative (> 95%) conversion. However, from ^{1}H-NMR spectra of high molecular weight PLCG could not be confirmed the polymer structure due to the low density of the chain ends. The microstructure of high molecular weight PLCG could be determined by ^{13}C-NMR. In the spectra, each peak come from the C=O carbon of the middle unity. The evidence for PLCGs that apart from the expected preponderance of LLL sequences, the two minor components, C and G, are indeed distributed at various points along the terpolymer chain, as would be expected in tapered microstructure. Typical ^{13}C-NMR spectra of PLCGs do not present any different signals between linear, branched and star-shaped terpolymers in this study.

The incorporation of branching into polymers influences the thermal properties. From DMA results (Set A and C), branched and star-shaped PLCGs had lower T_g because they had more chain ends and more free volume to give polymer chains move easily and the increasing of the chain flexibility due to its more free volume than linear PLCGs. However, if molecular symmetry exists and the side chains are long enough to order, side chain crystallization may occur

which increases the T_g. Normally, long-chain branching does not have a large influence on the T_g, while short chain branches often depress the T_g due to increase in free volume. The branching point also influences T_m and crystallinity of PLCGs terpolymer in this study. For example in Set A and B, the results indicated that imperfect crystallization possibly existed in the branched and star-shaped PLCGs but not in the linear PLCGs which rearrange and crystallize easily. However, the effect of arm number on T_m and heat of fusion (ΔH_m) for PLCGs was shown to be negligible in Set A and B, which is regarded to be due to the crystallinities of the terpolymers were on the same level. For Set C, lower T_m and no crystallinity for branched and star-shaped PLCGs that could be attributed to the crystalline imperfection mainly due to the short chain length of branch PLCG arms. The reduction in T_m with branching is attributed to shorter chain length and the increase in the number of free chain ends, which probably disrupts the orderly fold pattern of the crystal. In theory, short-chain branching influences thermal behavior and mechanical properties and limit chain crystallization, while long chain branching is utilized to control the rheological properties. However, it is often difficult to separate effect form termonomer incorporation and degree of short-chain branches or long chain branches on thermal transition and crystallization behavior due to the nature of random branching in polyester chemical composition. DSC results could be combined with TG data for defining the melt processing range of polymers and it was found that the branched and star-shaped PLCGs can be processed at lower temperature than their linear counterparts because lower T_m and higher T_d, which could be advantageous, especially in the melt processing of thermo-labile polyesters.

Moreover, the branch and star terpolymers exhibit useful mechanical and rheological properties in comparison with conventional linear terpolymer. From DMA results, the G' values of branched and star-shaped PLCGs are slightly lower than linear PLCGs at temperature above T_g. Also at body temperature (37^{o}C), G′ and G″ values was deceased from linear to branched and star-shaped PLCGs indicated that branched and star-shaped terpolymers were softer than the linear terpolymers at the usage temperature for biomedical applications. The effects of molecular architecture of PLCGs on the rheological properties were also found. Both G′ and G″ were decreased with increase in number of arm, implied that more chain ends impeded the movement of molecular chain and viscous properties of the melt were hence decreased. The η^* of branched and star-shaped PLCGs is less than linear PLCGs. The enhancement of viscosity is probably caused by the decreased regularity of the structure provide by the branched molecules.

The PLCGs films has been subjected to *in vitro* biodegradation in a phosphate buffer saline (PBS) solution at pH 7.40±0.01 as an immersion medium at the temperature 37±1 ^{o}C for 12 weeks. The weight loss and molecular weight changes have been characterized in order to determine the degradation pathway. From the results obtained, the biodegradation rate of star-shaped PLCG is faster than branch and linear PLCGs during 2-7 weeks due to the higher density of chain-end compared with linear PLCGs. The simple hydrolysis reaction can be acid-catalyzed in the event that the new carboxylic acid end groups formed causes the pH of the medium to drop below 7. The effect of branching leads to a dramatically decreasing of pH values of star-branched PLCGs more than linear PLCGs. Because of star-shaped had more chain ends and short chain length to disordered polymer chains. The degradation prefers occur in amorphous region more than crystalline region due to water molecules can penetrate easy in amorphous region. Because of star-shaped had more chain ends and short chain length due to disordered polymer chains. However, linear polymer chains can rearrange themselves from a disordered to an order state and gave more crystallinity. The hydrolysis cleaves the polymer backbone and leads to molecular weight of the polymer decrease.

In conclusion, the study on the effects of molecular architecture on the properties of biodegradable homopolyester and terpolyester will shed light on designing new polyesters-based materials with novel properties.

6. Conclusions

The problem using the PTOL as star-core initiator for the ROP of ε-caprolactone (CL) to controlled polymer molecular weight is the difficulty of dissolving PTOL in CL monomer and the steric hindrance of PTOL initiating leaded to imperfect 4-arm star-shaped poly(ε-caprolactone) (PCL). In this research, the star-shaped PCL was synthesized using a novel pentaerythritol tetrakis(6′-hydroxyhexanoate) star-core macroinitiator. The route of synthesis for star-shaped PCL in this study was the core-first method where polymer chains were grown directly from a multifunctional core. The effects of differing molecular architecture on the thermal, morphological, mechanical and rheological properties and *in vitro* hydrolytic degradation studies of linear and star-shaped PCLs were investigated.

Most of the results have already been discussed in detail. This final Chapter of this research now aims to bring together the main conclusions and correlate them as far as possible. These conclusions can be summarized as follows:

6.1 Synthesis of Pentaerythritol tetrakis(6′-hydroxyhexanoate) Star- Core Macroinitiator

Novel pentaerythritol tetrakis(6'-hydroxyhexanoate) as star-core macroinitiator can be prepared using CL to cap the OH groups of PTOL in a ratio of 4:1 as shown in Figure 6.1. The synthesis of star-core macroinitiator can be achieved via a sequence of simple reactions: methanolysis (79%), alcohol protection (92%), hydrolysis (75%), esterification and deprotection (43%) respectively, resulting in colorless oil and a moderate yield of the final product. It could be dissolved in common organic solvents and CL monomer. The chemical structure of star-core macroinitiator was confirmed by IR, NMR and ESI-MS. The IR spectrum shows the absorption peaks of C=O stretching (ester) at 1740 cm^{-1} and O-H stretching (alcohol) at 3400 cm^{-1}. The ^{1}H-MNR spectrum show δ = 3.91 ppm (multiplet), δ = 3.67 ppm (triplets), and δ = 2.42 ppm (multiplets) ppm. Electrospray ionization mass spectrometry (ESI-MS) data revealed in a signal at 625.3356 m/z $(M + Na)^{+}$ of $C_{29}H_{52}O_{12}Na$.

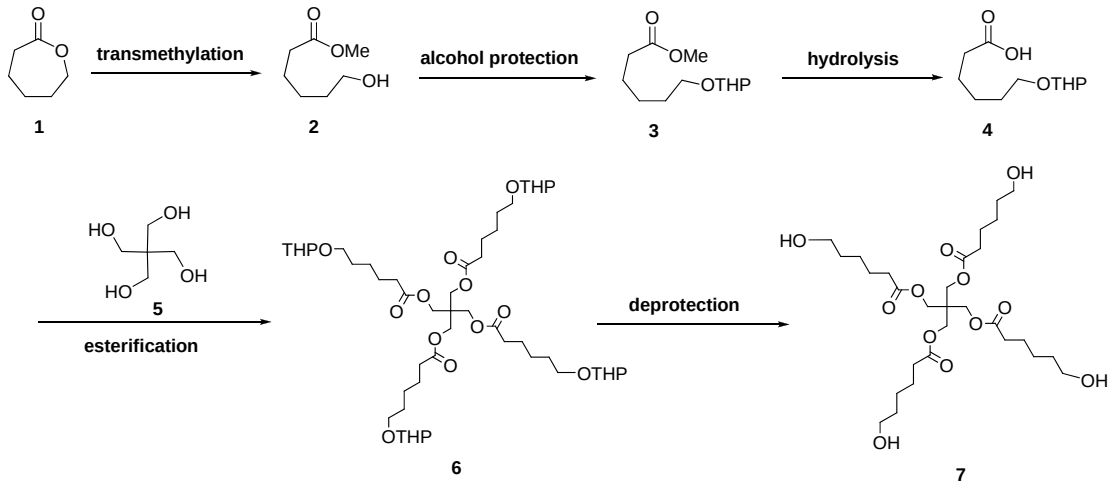

Figure 6.1 Synthesis of pentaerythritol tetrakis(6'-hydroxyhexanoate).

6.2 Synthesis of Low Molecular Weight PCLs Model Compounds with Different Molecular Architectures

Linear and star-shaped low molecular weight PCLs were synthesized using 4 mole% of hydroxyl initiators (1-hexanol, PTOL and star-core macroinitiator) through ROP of CL in the presence of 0.1 mole% stannous octoate as catalyst. Relatively high amounts of initiators (4 mole%) were used in order to obtain low molecular weight ($\overline{M}_{n,cal} \approx 3{,}000$) polymers for confirming the structure and evaluate the influence of short-chain branched structure on the properties.

Low molecular weight PCLs with different molecular architectures were characterized by ^{1}H-NMR, DSC and TG analyses. The molecular architectures of the low molecular weight PCLs obtained depended on the functionality of the alcohol used as the initiator. Mono-functional alcohols (1-hexanol) yielded linear polymer, while PTOL and star-core macroinitiator gave star-shaped polymers, as confirmed by their ^{1}H-NMR spectra. It was found that the average number of hydroxyl groups initiating polymerization, as calculated from the average degree of polymerization per arm (DP_n/arm) determined experimentally by ^{1}H-NMR, were close to the actual hydroxyl functionalities. Subsequently, degree of branching of star polymers can be estimated by comparing the mean-square radii with linear polymer. The branched structures contained some arm defects as evidenced on the $g^{1/2}/g'$ values, where $g^{1/2}$ and g' denote the ratios of mean-square radius of gyration and intrinsic viscosity of branched and star-shaped polymers to those of a linear structural reference with similar absolute molecular weight. It could be seen that the $g^{1/2}/g'$ value of star-shaped PCL_macroinitiator (0.98) was very close to 1.0 for an ideal star-shaped polymer with perfect arm architecture. Deviations from this relationship for PCL_PTOL (0.88) would point to steric hindrance of PTOL initiating leaded to imperfect star-shaped polymer.

The DSC and TG results showed that the star-shaped PCLs had lower melting temperatures, degrees of crystallinity and decomposition temperatures than the linear PCL. The thermal properties will affected when branching points are introduced into the polymer. The reduction in melting point with branching (more steric architecture) is attributed to shorter chain length and the increase in the number of free chain ends, which disrupts the orderly fold pattern of the crystal. Also, the melting peaks of star-shaped PCL initiated by star-core macroinitiator could not be observed. It can ascribe to the relatively slow crystallization rate and the amorphous phase in the sample increased. The lower melting temperatures and lower degradation temperatures of the star-shaped polymers widen the "processing window", an important advantage in the melt processing of PCL. As would be expected, the short chain branches mostly affect the thermal properties and crystallinity. This offers the possibility of being able to adjust the crystallinity by varying the shape of the polymer molecules, thus providing a useful means of controlling polymer properties and can be utilized and optimized for each application.

6.3 Effect of Molecular Architectures on the Properties of High Molecular Weight PCLs and PLLs

To study the effect of molecular architecture on the polymer properties (thermal, crystallinity, mechanical and rheological properties and *in vitro* hydrolytic degradation), the high molecular weight linear and star-shaped PCLs and PLLs were synthesized by using 1-hexanol, PTOL and star-core macroinitiator.

From the dilute-solution viscometry results, it was found that star-shaped PCLs exhibited lower intrinsic viscosities than linear PCL at same molecular weight ($\overline{M}_n$), supportive of the expected star-shaped structure. This is due to the fact that intrinsic viscosity reflects the chain conformation of the polymer in dilute solution. The star-shaped PLL occupies a smaller hydrodynamic volume in solution than the linear PLL at the same molecular weight.

The melting temperatures (T_m) and degree of crystallinity of star-shaped PCLs (PCL_PTOL and PCL_maroinitiator) are slightly lower than that of linear (PCL_1-hexanol). The results seem to suggest that the crystallization rearrangement of polymer chain ends is interrupted by the highly branched architecture of these polymers. In theory, short-chain branching influences thermal behavior and mechanical properties and limit chain crystallization, while long chain branching is utilized to control the rheological properties. DSC results could be combined with TG data for defining the melt processing range of polymers and it was found that the star-shaped PCLs can be processed at lower temperature than their linear counterparts because lower T_m and lower T_d, which could be advantageous, especially in the melt processing of thermo-labile polyesters.

The effects of molecular architecture of PCLs on the rheological properties were also found. All of linear and star-shaped PCLs exhibit a clear zero shear viscosity (η_0) followed by a shear thinning region at high shear rate. The η_0 of linear PCL_1-hexanol is higher than star-shaped PCL_macroinitiator at low shear rate. The expected behavior for a material with long chains is evident. It is generally found that the η_0 decreases as short chain are added to a polymer backbone. The reason for these phenomena is that the overall size is decreased. The lower η_0 of star-shape PCL_macroinitiator, which can be utilized in melt processing at lower temperature.

The hydrolytic degradation of linear and star-shaped PCLs and PLLs were also investigated. At the same polymer molecular weight, linear and star-shaped PCLs and PLLs films has been subjected to *in vitro* biodegradation in a phosphate buffer saline (PBS) solution at pH 7.40±0.01 as an immersion medium at body temperature 37±1.0ºC for 21 weeks. The weight loss, pH and thermal stability changes have been characterized in order to determine the degradation pathway. From the results obtained, the PCL films were still translucent and fixable appear almost unchanged surface interior and weight during the period of study because of the long degradation time. The biodegradation rate of the star-shaped PLL_ macroinitiator is faster than imperfect star-shaped PLL_PTOL and linear PLL_hexanol during 21 weeks due to higher density of chain-end of star-spahed PLLs than linear chain of comparable molecular weight. The simple hydrolysis reaction can be acid-catalyzed in the event that the new carboxylic acid end groups formed causes the pH of the medium to drop below 7. The effect of branching leads to a dramatically decreasing of pH values of star-shaped PLL_macroinitiator more than imperfect star-shaped PLL_PTOL and linear PLL. The degradation prefers occur in amorphous region more than crystalline region due to water molecules can penetrate easy in amorphous region. Because of star-shaped had more chain end short chain length due to disordered polymer chains.

Thermal analysis from DSC revealed that the % crystallinity of PLLs films increased during 21 weeks indicated to the molecules in the amorphous region of a polymer were crystallized slowly in immersion medium. In the earlier stage of *in vitro* biodegradation, the low degradation rate of these PLLs occurred with the molecules in the amorphous region were crystallized at the same time. As the time increase, the degradation rate increased, which also could be attributed to water penetrates the polymer matrix and facilitates the hydrolytic chain cleavages.

On the basis of all of these results, it was concluded that the problem of the insolubility and steric hindrance of PTOL could be overcome by using the novel star-core macroinitiator leading to the synthesis of star-shaped PCLs with interesting properties which were different to linear PCL.

6.4 Effect of Molecular Architecture on the Properties of a Biodegradable Terpolyester for Biomedical Applications

Series of linear, branched and star-shaped poly(*ε*-caprolactone)s (PCLs), poly(L-lactide)s (PLLs) and poly(L-lactide-*co*-*ε*-caprolactone-*co*-glycolide)s (PLCGs) 75:20:5 mol% were synthesized with structure variation of arm number through ring-opening polymerization (ROP) at 120^{o}C for 48 hours in the presence of 0.1 mole% stannous octoate as catalyst. Arm number was varied by using range of alcohols with different number of hydroxyl groups (1-hexanol, 2,2-dimethyl-1,3-propanediol (DMP), trimethylolpropane (TMP) and pentaerythritol (PTOL) as the

initiator. The molecular weights were controlled by varying the molar ratios of monomer to initiator, [M]:[I] and tend to increase with increasing [M]:[I] ratio.

Low molecular weight PCLs and PLLs with different molecular architectures were synthesized to confirm the structure and evaluate the influence of chain architecture on the properties that confirmed by ^{1}H-NMR, intrinsic viscosities, [η], DSC and TG analysis. The ^{1}H-NMR results showed that the average number of OH groups initiating polymerization, as calculated from the average degree of the polymerization per arm (DP_n/arm) was close to the actual OH functionalities. The arm structures as evidenced on the $g^{1/2}/g'$ values, where $g^{1/2}$ and g' denote the ratios of mean-square radius of gyration and intrinsic viscosity of star-shaped to those of linear structure with similar molecular weight. From the results obtained, the structure still had some arm defects. The branched and star-shaped PCLs exhibited the lower [η], melting temperatures (T_m), degree of crystallinity (X_c) and higher degradation temperatures (T_d) than the linear counterparts. That is attributed to shorter chain length and the increase in the number of free chain ends, which probably disrupts the orderly fold pattern of the crystal.

Structure-property studies have shown that variation in the molecular architecture from linear to star-branch can have substantial effects on the thermal properties, crystallinity, mechanical, rheological and biodegradability properties of the high molecular weight PLCGs, 75:20:5 mole% terpolymers with different molecular architecture. From ^{1}H and ^{13}C-NMR results showed that polymer composition is corresponding to the monomer feed and they had tapered character in their monomer sequence distributions. Branched and star-shaped PLCG had lower T_g, T_m and heat of melting (ΔH_m) than linear PLCGs. The molecular architecture is not significant effect on mechanical (tensile) properties. However, from DMA measurement, the shear storage modulus (G') at 37^{o}C (body temperature) of branched and star-shaped was lower than linear PLCGs indicating soft material at the usage temperature. From the melt rheology measurements, the melt viscosity (η^{*}) is also lower for branched and star-shaped PLCGs, which can be utilized in melt processing at lower temperatures. An *in vitro* biodegradation of PLCGs films was carried out for 12 weeks in a phosphate buffer saline (PBS) solution at pH 7.40 ± 0.01 as an immersion medium at the temperature 37 ± 1 ^{o}C. From the results obtained, the biodegradation rate of star-shaped PLCG is faster than branch and linear PLCGs during 2-7 weeks due to the higher density of chain-end compared with linear PLCGs. The simple hydrolysis reaction can be acid-catalyzed in the event that the new carboxylic acid end groups formed causes the pH of the medium to drop below 7. The hydrolysis cleaves the polymer backbone and leads to molecular weight of the polymer decrease. On the basis of all of these results, it was concluded that the terpolymer properties can be effectively controlled by varying the molecular architecture to suit a different applications.

References

1. P. Meepowpan, B. Thapsukhon, M. Dumklang, T. Wongchanapiboon, R. Molloy and W. Punyodom, "Efficiency of Tin(II) Butoxide as a Catalyst in the Synthesis of L-Lactide", *The 42nd International Symposium on Macromoleules World Polymer Congress (MACRO 2008)*, Taipei, Tiwan (2008).
2. Differential Scanning Calorimeter Model DSC-7, Instrument Manual, Perkin-Elmer Corp., Norwalk, Conn., USA.
3. A. Kowalski, A. Duda and S. Penczek, Macromol. Rapid. Commun., 19, 567 (1998).
4. P.A. Ongley, "Practical Handbook of Organic Chemistry", Pergamon Press, Germany (1972).
5. Council of European, "European Pharmacopoeia", 3rd ed. (1997).
6. C.M. Dong, K.Y. Qiu, Z.W. Gu and X.D. Feng, Macromolecules, 34, 4691 (2001).
7. C.M. Dong, K.Y. Qiu, Z.W. Gu and X.D. Feng, Polymer, 42, 6891 (2001).
8. B. Thapsukhon, "Effect of Molecular Architecture on the Properties of a Biodegradable Terpolyester for Biomedical Applications", M.S. Thesis, Chiang Mai, Thailand (2006).
9. W. Yuan, X. Tang, X. Huang and S. Zheng, Polymer, 46, 1701 (2005).
10. A. Schindler, Y.M. Hibionada and C.G. Pitt, J. Polym. Sci., Polym. Chem. Ed., 20, 319 (1982).
11. A. Kaivez, X.A. Gallez, D. Daoust, J. Devaux and P. Godard, Polymer, 43, 3181 (2002).
12. H.M. Huang, I.C Liu and R.C.C. Tsiang, Polymer, 46, 955 (2005).
13. Q. Hao, F. Li, Q. Li, Y. Li, L. Jia, J. Yang, Q. Fang and A. Cao, Biomacromolecules, 6, 2236 (2005).
14. C.A.P. Joziasse, H. Grablowitz and A.J Penning, Macromol. Chem. Phys., 6, 2236 (2005).
15. L.I. Palade, H.J. Lehermeier and J.R. Dorgan, Macromolecules, 34, 1384 (2001).
16. M. Lang, R.P. Wong and C.C. Chu, J. Polym. Sci., Part A: Polym. Chem., 40, 1127 (2002).
17. M.G. McKee, S. Unal, G.L. Wilkes and T.E. Long, Progress Polymer Science, 30, 507 (2005).
18. H. Claesson, E. Malmström, M. Johansson and A. Hult, Polymer, 43, 3511 (2002).
19. H.Jiabng, J. He, Y. Tao and Y. Tang, J. Polym., 35(7), 598 (2003).

APPENDIX 1

Girdthep, S., Worajittiphon, P., Molloy, R., Saisamorn, L., Leejarkpai, T., and **Punyodom, W.***, *"Biodegradable nanocomposite blown films based on poly(lactic acid) containing silver-loaded kaolinite: A route to controlling moisture barrier property and silver ion release with a prediction of extended shelf life of dried longan"*, **Polymer**, *accepted* (impact factor = 3.776)

From: "Kohzo Ito" <ees.jpol.60d0.2ccbff.a6fd0ab1@eesmail.elsevier.com>
Date: 24 ตุลาคม 2557 13 นาฬิกา 51 นาที 51 วินาที GMT+7
To: winitacmu@gmail.com
Subject: Your Submission POLYMER-14-1310R1

Ref.: Ms. No. POLYMER-14-1310R1
Biodegradable nanocomposite blown films based on poly(lactic acid) containing silver-loaded kaolinite: A route to controlling moisture barrier property and silver ion release with a prediction of extended shelf life of dried longan

Polymer

Dear Dr. Winita Punyodom

I am pleased to tell you that your work has now been accepted for publication in Polymer.

When your paper is published on ScienceDirect, you want to make sure it gets the attention it deserves. To help you get your message across, Elsevier has developed a new, free service called AudioSlides: brief, webcast-style presentations that are shown (publicly available) next to your published article. This format gives you the opportunity to explain your research in your own words and attract interest. You will receive an invitation email to create an AudioSlides presentation shortly. For more information and examples, please visit http://www.elsevier.com/audioslides.

Thank you for submitting your work to this journal.

With kind regards

Kohzo Ito, Dr Eng
Rest of Asia: Phys.Chem. & Functionality
Polymer

Biodegradable nanocomposite blown films based on poly(lactic acid) containing silver-loaded kaolinite: A route to controlling moisture barrier property and silver ion release with a prediction of extended shelf life of dried longan

Sutinee Girdthep[a], Patnarin Worajittiphon[a], Robert Molloy[b], Saisamorn Lumyong[c], Thanawadee Leejarkpai[d] and Winita Punyodom[a,*]

[a]Polymer Research Laboratory, Department of Chemistry, Faculty of Science, Chiang Mai University, Chiang Mai, 50200, Thailand

[b]Materials Science Research Center, Faculty of Science, Chiang Mai University, Chiang Mai, 50200, Thailand

[c]Department of Biology, Faculty of Science, Chiang Mai University, Chiang Mai, 50200, Thailand

[d]National Metal and Materials Technology Center, National Science and Technology Development Agency, Pathumthani, 12120, Thailand

*** Corresponding author:** Polymer Research Laboratory, Department of Chemistry, Faculty of Science, Chiang Mai University, Chiang Mai, 50200, Thailand.

E-mail address: winitacmu@gmail.com (W. Punyodom), *Tel: +66 5394 3341; fax: +66 5389 2277*

ABSTRACT

Novel biodegradable nanocomposite blown films based on compatibilized poly(lactic acid)-poly(butylene adipate-*co*-terephthalate) blend are fabricated for use as a model package for dried longan. Silver-loaded kaolinite (AgKT) dispersing in the polymer matrix in intercalated-

From: "Kohzo Ito" <ees.jpol.60d0.2ccbff.a6fd0ab1@eesmail.elsevier.com>
Date: 24 ตุลาคม 2557 13 นาฬิกา 51 นาที 51 วินาที GMT+7
To: winitacmu@gmail.com
Subject: Your Submission POLYMER-14-1310R1

Ref.: Ms. No. POLYMER-14-1310R1
Biodegradable nanocomposite blown films based on poly(lactic acid) containing silver-loaded kaolinite: A route to controlling moisture barrier property and silver ion release with a prediction of extended shelf life of dried longan

Polymer

Dear Dr. Winita Punyodom

I am pleased to tell you that your work has now been accepted for publication in Polymer.

When your paper is published on ScienceDirect, you want to make sure it gets the attention it deserves. To help you get your message across, Elsevier has developed a new, free service called AudioSlides: brief, webcast-style presentations that are shown (publicly available) next to your published article. This format gives you the opportunity to explain your research in your own words and attract interest. You will receive an invitation email to create an AudioSlides presentation shortly. For more information and examples, please visit http://www.elsevier.com/audioslides.

Thank you for submitting your work to this journal.

With kind regards

Kohzo Ito, Dr Eng
Rest of Asia: Phys.Chem. & Functionality
Polymer

Elsevier Editorial System(tm) for Polymer
Manuscript Draft

Manuscript Number: POLYMER-14-1310R1

Title: Biodegradable nanocomposite blown films based on poly(lactic acid) containing silver-loaded kaolinite: A route to controlling moisture barrier property and silver ion release with a prediction of extended shelf life of dried longan

Article Type: Research Paper

Section/Category: Physical Chemistry of Polymers

Keywords: polymer-clay nanocomposite; barrier properties; shelf life prediction

Corresponding Author: Dr. Patnarin Worajittiphon,

Corresponding Author's Institution: Chiang Mai University

First Author: Sutinee Girdthep

Order of Authors: Sutinee Girdthep; Patnarin Worajittiphon; Robert Molloy; Saisamorn Lumyong; Thanawadee Leejarkpai; Winita Punyodom

Abstract: Novel biodegradable nanocomposite blown films based on compatibilized poly(lactic acid)-poly(butylene adipate-co-terephthalate) blend are fabricated for use as a model package for dried longan. Silver-loaded kaolinite (AgKT) dispersing in the polymer matrix in intercalated-exfoliated fashion functions as an excellent property improver of the blend. The emphasis of this paper is enhancement of film moisture barrier property by inducing polymer crystallization coupled with formation of AgKT tortuous path. Additionally, controlled silver release which provides long-term antibacterial activity is attributed to AgKT's layered structure. The amount of released silver ions herein also complies with migration levels specified by the standard for food-contact plastic packages. Dried longan shelf lives as eventually predicted by experimental moisture sorption isotherm and by Peleg model are almost identical (~308 days) for the nanocomposite films being over two folds of that obtained from the compatibilized blend package at ambient condition.

Dear Professor Dr. Kohzo Ito,

The authors would like to thank all 3 reviewers for giving of their valuable time to review our manuscript. Their comments and suggestions are extremely useful in filling in one or two gaps in the paper which, in turn, will benefit the reader's understanding. Please also note the change in Corresponding Author from "Dr. Patnarin Worajittiphon" to "Dr. Winita Punyodom". This is due to Dr. Punyodom being the Principal PhD Thesis Advisor of Ms. Sutinee Girdthep (the first-named author) whose work this paper is based on and for whom this paper will fulfill one of the requirements for her PhD graduation.

Our answers to the reviewers' comments are given in red below and the actual changes made to the manuscript are additionally highlighted in yellow both below and in the revised manuscript.

Yours respectfully

Asst. Prof. Dr. Winita Punyodom

Corresponding Author

ANSWERS TO REFEREES' COMMENTS

Manuscript ID: POLYMER-14-1310

TITLE: **Biodegradable nanocomposite blown films based on poly(lactic acid) containing silver-loaded kaolinite: A route to controlling moisture barrier property and silver ion release with a prediction of extended shelf life of dried longan**

AUTHORS: **Sutinee Girdthep, Patnarin Worajittiphon, Robert Molloy, Saisamorn Lumyong, Thanawadee Leejarkpai and Winita Punyodom***

REVIEWER #1

1. Please confirm the role of TBT through extensive surface morphology study.

We have edited the relevant paragraph as highlighted in yellow below and in the revised manuscript in section "*3.2. Morphology evaluation*" on page 14.

Fig. 3a-c show the fractural surface morphologies of the films. It can be seen that the compatibilized blend with TBT added (Fig. 3b) demonstrates smoother topography, suggesting more compatibility between PLA and PBAT. Such an observation reflects an effectiveness of TBT as the compatibilizer promoting strong interaction between the two polymer phases during melt-extrusion. Because PLA-*co*-PBAT copolymers are formed through transesterification reactions in the presence of TBT during melt processing [3], the interfacial adhesion between the two phases is enhanced by the PLA-*co*-PBAT copolymers acting as compatibilizers [3-5, 25].

2. Please do extensive TEM characterization and try to understand the role of TBT and Ag/KT. Also measure the melt-rheological properties.

We have further discussed the roles of TBT and AgKT from the TEM results in the revised manuscript in section "*3.2. Morphology evaluation*" on pages 16-17 as highlighted below.

The microstructure of the nanocomposite film is revealed by the TEM image (inset b in Fig. 3d) showing dark and bright regions of the AgKT layers as an intercalated and exfoliated structure in the polymer matrix respectively. This is in good agreement with the XRD observations (Fig. 3d). Particularly, the XRD patterns show absence of AgKT peak at 8.54 º (1.04 nm) when incorporated into the compatibilized polymer blend corresponding to the exfoliated structure of AgKT in the polymer matrix in the TEM results. However, the dispersed-AgKT had only a few intercalated structures in the polymer matrix from the XRD results (inset a in Fig. 3d) which show only a small peak at 8.74 º (1.02 nm). Both TEM and

XRD suggest the AgKT dispersion is intercalated-exfoliated in nature. A greater number of AgKT layers of the related plane is thus likely to exfoliate in the matrix. Although the exfoliated nanocomposites have generally been reported to exhibit the best properties, such as good barrier properties due to the optimal interaction between the clay and the polymer [6], an additional advantage in this work which is due to the silver nanoparticles is the long-lasting antibacterial activity as described later.

Moreover, a possible cause of the molecular TBT-compatibilizer structure is that it contains both hydrophobic and hydrophilic groups which help to disperse the AgKT in the polymer matrix. While the hydrophobic part of TBT can interact with the hydrophobic part of clay, the hydrophilic part can interact with the polar components of the polymer. Hence, the probability of clay layer aggregation in the polymer matrix is minimized. Furthermore, clay gallery separation due to polymer chain segment insertion into the clay layers is additionally reflected from an increase of d-spacing from 0.68 nm (13.00 º) to 0.72 nm (12.23 º) as illustrated by the TEM result.

In the sections relating to the measurement of the melt-rheological properties, we have edited "*2.2. Preparation of blend and nanocomposite films*" on pages 6-7 for the methodology and "*3.2. Morphology evaluation*" on page 13 for the results, as detailed below.

On pages 6-7:

For the screw speed setting, the melt flow index (MFI) of the sample is an important consideration in helping to set an appropriate screw speed for safeguarding the machine and for indicating the melt-rheological properties of the polymer. The MFI of PLA/PBAT with TBT and AgKT was determined using a Davenport MFI-10 Melt Flow Indexer (Lloyd Instruments). The samples were melted at 190 ºC and extruded through a capillary die using a 2.16 kg piston according to ASTM D1238. The weights of extrudate were measured at 10 minute intervals. The MFI value was taken as the average of at least 15 measurements.

On page 15:

Moreover, the melt-rheological properties in terms of the melt flow index (MFI) of the polymer (from the twin-screw extruder) could give an indication of the polymer chain mobility and the compatibility enhancement by PLA-*co*-PBAT formation via the role of TBT. Thus, the decrease in MFI from 4.85 (PLA/PABT) to 4.72 (PLA/PBAT/TBT) g/10 min when adding 0.5 phr of TBT indicated an increase in melt viscosity due to PLA-*co*-PBAT formation in the system. Similarly, the addition of AgKT also decreased the MFI from 4.72 of (PLA/PBAT/TBT) to 3.99 (PLA/PBAT/TBT/AgKT) g/10 min due to the formation of a clay network with polymer chains in between the KT platelets resulting in a decrease in melt fluidity. These observed changes in MFI are consistent with linear rheological behavior [26].

3. Please clarify the compatibilization role of TBT by measuring torque during processing.

On page 14:

In addition, transesterification between the PLA and PBAT to give PLA-*co*-PBAT for improving the blend compatibility could be induced by changing the torque due to the presence of peroxide TBT-compatibilizer during the melting process in the internal mixer, as reported in previous work [4,5,25]. As a result of the formation of PLA-*co*-PBAT, the torque increased significantly after adding the TBT-compatibilizer and then decreased slightly before becoming stable. Chain scission of the polymer leading to a decrease in molecular weight has also been observed at high concentrations of TBT (0.6 phr) resulting in a decrease in torque [4,5,25].

4. If possible, please do SAXS study. X-ray results must be plotted from 1 to 10 deg.

The XRD results have been modified with an expanded scale of 1-10 deg inserted in Fig. 3(d) on page 15. While we agree with the reviewer's suggestion that SAXS would be very useful, we do already have TEM and XRD results which are considered to be sufficient for discussing the dispersion of nanoparticles in the polymer matrix. The additional details in Fig. 3(d) are highlighted in yellow on page 16 of the revised manuscript.

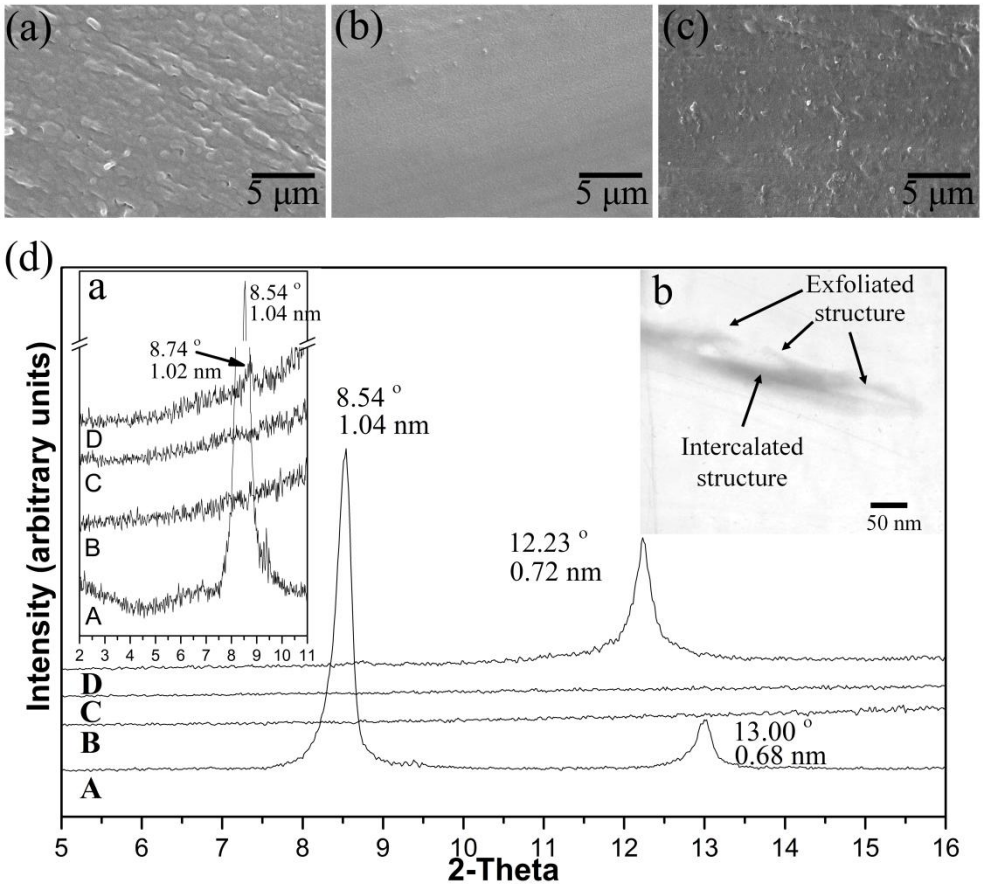

Fig. 3. Fractural surface morphologies of (a) PLA/PBAT blend, (b) PLA/PBAT/TBT compatibilized blend, (c) PLA/PBAT/TBT/AgKT nanocomposite films at 5k magnification and (d) XRD patterns of (A) AgKT nanocomposite powder, (B) PLA/PBAT blend, (C) compatibilized PLA/PBAT/TBT blend and (D) PLA/PBAT/TBT/AgKT nanocomposite films. Inset in (d) shows (a) an XRD plot from 2-11 degrees of 2-Theta and (b) a TEM micrograph of the nanocomposite film at 100k magnification.

REVIEWER #2

This is a carefully done study and the findings are of considerable interest. A few minor revisions are list below. The dispersed and aggregated of the silver-loaded kaolinite in PLA/PBAT blend, PLA/PBAT/TBT compatibilized blend and PLA/PBAT/TBT/AgKT nanocomposite are poorly defined. What is the temperature of morphology properties? Were dispersant used?

More explanation has already been added regarding the dispersion of silver-loaded kaolinite in the polymer matrix from both the TEM and XRD results on page 16 (see also the answer to Reviewer 1, question 2). The temperature at which the morphology properties were studied by SEM, TEM and XRD was ambient temperature (25 ºC). Further details, highlighted in yellow, have been added on pages 7-8 in the revised manuscript at "*2.3 Characterization*". In this research, a specific dispersant was not used. However, the TBT-compatibilizer could help to disperse the AgKT in the polymer matrix due to the combination of hydrophobic and hydrophilic groups in its molecular structure, as alluded to on page 15.

On pages 7-8:

Film morphology was investigated on fractured surfaces at ambient temperature (25.0 º C) by a scanning electron microscope, SEM, (JSM 5910-LV, JEOL) equipped with an energy dispersive spectroscopy, EDS, (EDX-700HS, Shimadza) to quantify the amount of Ag nanoparticles. The film samples were mounted onto SEM stubs with carbon tabs attached then coated with gold using a sputter-coater.

The dispersion of the AgKT in the polymer matrix was evaluated at 25.0 º C by a transmission electron microscope, TEM, (JSM-2010, JEOL) at an accelerating voltage of 100 kV. The TEM specimen was prepared, cryotomed at low temperature (-60 °C), and stained. TEM micrographs were obtained on thin cross-sections of the nanocomposite films.

X-ray diffractograms were acquired using an X-ray diffractometer (XRD TTRAX III, Rigaku) equipped with a filament (0.15418 nm) at a scanning rate of 2 $^{o} \cdot min^{-1}$ at room temperature. The Bragg's equation was used to determine basal spacing of AgKT.

REVIEWER #3

It is a well written paper with a clear objectives and research methodology.

However, the authors need to provide some explanation on the following matters:

1. In the case of PLA/PBAT/TBT/AgKT, please provide some explanation on where would be the preferred location for the KT in the polymer matrix.

Some further explanation has been included on page 17 (see also the answer to Reviewer 1, question 2) as follows.

Although the exfoliated nanocomposites have generally been reported to exhibit the best properties, such as good barrier properties due to the optimal interaction between the clay and the polymer [6], an additional advantage in this work which is due to the silver nanoparticles is the long-lasting antibacterial activity as described later.

2. With reference to Table 1, apart from molecular orientation as explained by the authors on page 18, how does the blowing process influenced the clay orientation and subsequently the strength of the samples in MD and TD?

Further discussion was added in "*3.3. Mechanical properties*" on page 19 as follows.

Although extended chain crystals occurred in MD from the tension force that caused a higher degree of orientation than in TD, the induced crystals were grown in the vertical direction (TD) by the clay platelets. Consequently, due to the polymer reinforcement by the induced crystals and clay molecular orientation which interacted with the polymer chains in TD, the strength of the samples in TD was higher than in MD.

3. Authors mentioned about "governed by higher crystallinity of PLA compared to PBAT", however, no data on crystallinity appear to be reported in the paper. How does the presence of TBT and AgKT influence the degree of crystallinity of PLA/PBAT blend?

On page 24, the degrees of crystallinities of PBAT in the PLA/PBAT blend, the PLA/PBAT/TBT compatibilized-blend and the PLA/PBAT/TBT/AgKT composite blend could not be calculated due to the melting peak of PBAT (110.8 ºC) overlapped with the crystallization peak of PLA (117.8 ºC). Moreover, since the compositions of the polymer blends in our research were PLA-based, it was difficult to observe characteristic peaks of PBAT. We also discussed the degree of crystallinity in terms of the heat of melting (ΔH_m). In this respect, the wording "governed by higher crystallinity of PLA compared to PBAT" on page 24 has been changed to "From the relative sizes of the repeating units of PLA and PBAT, it is to be expected that that PLA will be more crystalline than PBAT."

For the influence of TBT and AgKT on the crystallinity of PLA/PBAT, additional comments have been added under "*3.4. Thermal properties*" on pages 20-21 as follows.

Although T_m values of PLA/PBAT blend, TBT compatibilized-blend and PLA/PBAT/TBT/AgKT nanocomposite films are almost identical, ΔH_m of these three different samples are observably different, i.e. 19.4, 19.9 and 21.3 J g^{-1}, respectively. Thus, crystallite amount formed can be ordered in a sequence as in nanocomposite > compatibilized blend > blend. It should be noted here that both TBT and AgKT are nucleating agents which can influence the crystallization of PLA in a PLA/PBAT blend, with AgKT being a stronger nucleating agent than TBT. In the case of TBT, chain scission of PLA via TBT-catalyzed transesterification can facilitate molecular rearrangement and the formation of smaller-sized crystallites. In comparison, AgKT gave rise to an even larger increase in crystallinity (higher ΔH_m) than TBT due to the effect of the clay platelets in orienting the PLA chains in such a way as to induce crystallization.

Additional Changes

Few minor corrections to the paper were done in comparison to the submitted version. None of these corrections affect the conclusions of the paper. The following changes were made:

On the first page, the corresponding author has been changed to: Winita Punyodom, *E-mail* address: winitacmu@gmail.com (W. Punyodom).

On page 20, the following highlighted sentence has been added.

The T_c and ΔH_c of PLA/PBAT blend, TBT-compatibilized blend and PLA/PBAT/TBT/AgKT nanocomposite film are observed at 117.8 °C (13.4 J g^{-1}), 112.8 °C (15.4 J g^{-1}) and 112.5 °C (16.3 J g^{-1}), respectively, while both neat films do not show their T_c and ΔH_c. It can be assumed that this is a PLA crystallization peak [5].

On page 34, some additions to the list of Acknowledgements have been added.

Acknowledgements

This work was financially supported by the Human Resource Development in Science Project (Science Achievement Scholarship of Thailand, SAST) and the Graduate School, Chiang Mai University (for Sutinee Girdthep), the Thailand Research Fund (TRF) and the Commission on Higher Education (CHE) (Grant No. MRG4780109 for Winita Punyodom), the National Science and Technology Development Agency Northern Region (NSTDA Northern Network)

and the “Trade Standard Compliance and Innovations for Agri-Food Supply Chains in Thailand and Neighbouring Countries Project” under the Science and Technology Research Institute, Chiang Mai University (for Patnarin Worajittiphon and Winita Punyodom).

On page 36, two more references have been added.

[25] Coltelli M-B,S Bronco, Chinea C. Polym Degrad Stab 2010;96:332-41.

[26] Wang K, Liang S, D Jinni, Y Hong, Z Qin, F Qiang, D Xia, W Dujin, Han C. C. Polymer 2006;47:7131-44.

Graphical Abstract (for review)

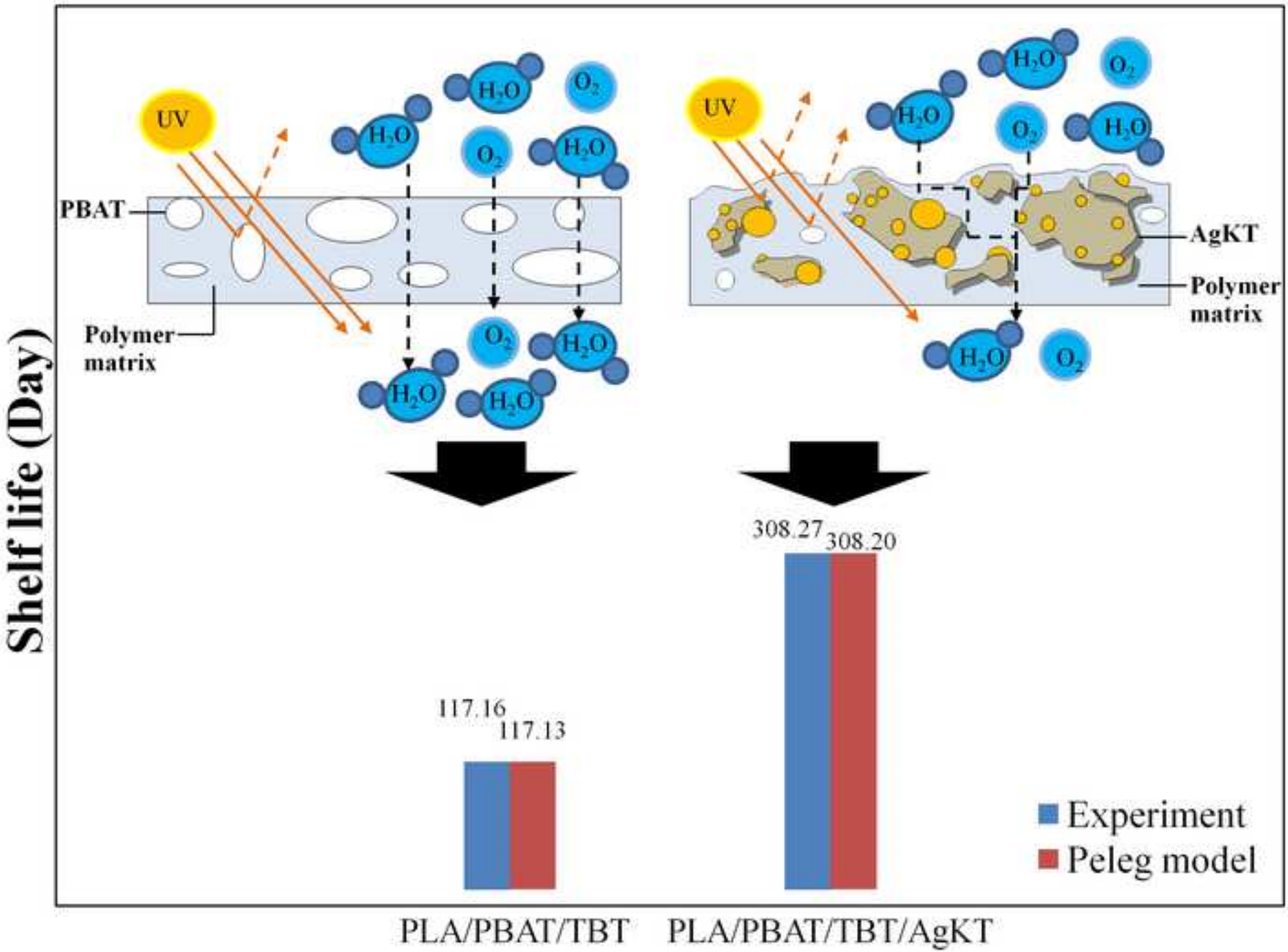

Biodegradable nanocomposite blown films based on poly(lactic acid) containing silver-loaded kaolinite: A route to controlling moisture barrier property and silver ion release with a prediction of extended shelf life of dried longan

Sutinee Girdthep[a], Patnarin Worajittiphon[a], Robert Molloy[b], Saisamorn Lumyong[c], Thanawadee Leejarkpai[d] and Winita Punyodom[a,*]

[a]Polymer Research Laboratory, Department of Chemistry, Faculty of Science, Chiang Mai University, Chiang Mai, 50200, Thailand

[b]Materials Science Research Center, Faculty of Science, Chiang Mai University, Chiang Mai, 50200, Thailand

[c]Department of Biology, Faculty of Science, Chiang Mai University, Chiang Mai, 50200, Thailand

[d]National Metal and Materials Technology Center, National Science and Technology Development Agency, Pathumthani, 12120, Thailand

*** Corresponding author:** Polymer Research Laboratory, Department of Chemistry, Faculty of Science, Chiang Mai University, Chiang Mai, 50200, Thailand.

E-mail address: winitacmu@gmail.com (W. Punyodom), *Tel: +66 5394 3341; fax: +66 5389 2277*

ABSTRACT

Novel biodegradable nanocomposite blown films based on compatibilized poly(lactic acid)-poly(butylene adipate-*co*-terephthalate) blend are fabricated for use as a model package for dried longan. Silver-loaded kaolinite (AgKT) dispersing in the polymer matrix in intercalated-

exfoliated fashion functions as an excellent property improver of the blend. The emphasis of this paper is enhancement of film moisture barrier property by inducing polymer crystallization coupled with formation of AgKT tortuous path. Additionally, controlled silver release which provides long-term antibacterial activity is attributed to AgKT's layered structure. The amount of released silver ions herein also complies with migration levels specified by the standard for food-contact plastic packages. Dried longan shelf lives as eventually predicted by experimental moisture sorption isotherm and by Peleg model are almost identical (~308 days) for the nanocomposite films being over two folds of that obtained from the compatibilized blend package at ambient condition.

Keywords: Polymer-clay nanocomposite, Barrier properties, Shelf life prediction

1. Introduction

Golden dried longan is one of the important economic fruits of warm-climate countries. During longan harvest season, there is a great amount of longan produced exceeding the local demand. To add value to the harvest and especially to extend shelf life of the longan flesh, it is typically dried and packaged for distant markets. Effective drying of the longan flesh should yield water activity (a_w) of < 0.6 which is able to inhibit growth of micro-organisms [1]. Since this dried product has a high moisture adsorption rate, its shelf life is usually shortened by bacterial and microbial contaminations. Temperature, oxygen and especially UV light radiation levels are typical storing conditions that cause product browning [2]. Not only does this color change reduce product shelf life, but also ruins its physical appearance. Consequently, the dried longan loaded in the package with suitable properties; essentially, water, oxygen and UV barriers, as well as antibacterial activity, is required as an alternative way to prolong its shelf life.

Nowadays, one of the common packaging polymers for dried fruits is oriented poly propylene (OPP) which exhibits high tensile strength, good abrasion, and high chemical resistance. However, it is a solid residue in the environment and made from limited petroleum resources. The concern to move to renewable resources and reduced environmental impact has focused the study of biodegradable and bio-based materials as alternatives to replace petroleum-based packaging. One of most studied biodegradable polymers is poly(lactic acid) (PLA). Nevertheless, its intrinsic hardness and brittleness have been major bottlenecks for practical uses. Blending of PLA with high-toughness and more flexible biodegradable polymers, such as poly(butylene adipate-*co*-terphthalate) (PBAT), was proved as a route to solve such a problem. At the molecular level, PLA/PBAT blend showed immiscibility between the two polymers, attributing to significantly poor properties. The two polymer phases were linked together via transesterification using tetrabutyl titanate (TBT) as a compatibilizer [3-5].

Packaging polymers for dried fruits should be able to prevent the permeability of water vapour and gas molecules. Polymer nanocomposites, rather than polymer blends, have been produced for this particular purpose by the incorporation of rigid layered nano-fillers, including montmorillonite (MMT), kaolinite (KT), vermiculite and talc [6]. The clay layers dispersing in a polymer matrix can create a tortuous path [7] that helps to reduce the water vapour and gas permeation though the packaging films. KT is the commercially-available clay used in this work. Although KT price is lower than MMT, there have been a very few literature reports on KT nanocomposites in comparison with MMT [8]. Generally, the KT was simply modified to improve the dispersion in the polymer by an organic solvent, i.e. dimethyl sulfoxide (DMSO) [9]. Moreover, the addition of metal nanoparticles such as silver (Ag) into the interlamellar space of KT, during reduction reactions by DMSO, can help to increase interlamellar space of KT [5,10,11], leading to higher clay dispersion in polymer matrix. The

presence of Ag nanoparticle-deposited KT not only enhances gas barrier properties by action of the clay layers, but also inhibits bacterial growth on polymer film by function of Ag nanoparticles. In addition, the clay layer is likely to control Ag release for long-lasting antibacterial effect to save the product quality.

Previously, there have been several studies regarding KT as a filler for polymer matrices, particularly ethylene-vinyl alcohol (EVOH) copolymers [12], poly(*m*-xylene adipamide) (MXD6) resin [8], polylactide [13], cassava starch [14,15], polyolefin/iron [16], polyimide [17] and poly(lactic acid)/poly(butylene adipate-*co*-terephthalate) (PLA/PBAT) [5]. The authors consistently reported that KT-polymer nanocomposites exhibited a significant improvement in tensile strength, elongation at break, thermal resistance, UV blocking, and dramatically better waterproofing, including water vapour and gas barrier properties [5,8,12-17]. These papers presented preparation and characterizations of the polymer nanocomposites with proposed applications. However, how such polymer materials actually work as packaging material in blown-film form has been shown in very few literature reports. Packaging film performance can be recognized via experimental or simulational investigation of products' shelf life. To predict shelf life of the dried longan, water vapour permeability (WVP) of the packaging materials is one of the important criteria used to predict a rate of moisture uptake [18]. Moreover, water activity (a_w) is also generally applied for shelf life prediction of dried fruit as the main parameter since water is required for cell metabolism and, hence, micro-organism growth [19]. The a_w values are obtained by measurements of water sorption isotherm of the product [20] which is mathematically simplified to many equations. For example, Brunauer-Emmett-Teller (B.E.T.) and Guggenheim-Anderson-de Boer (G.A.B.) models are classified as theoretical, while Halsey and Peleg models are considered as semi-empirical and Oswin model is categorized as empirical [19,21].

Herein, PLA/PBAT blends and their nanocomposites with silver-loaded kaolinite

(AgKT) are developed as polymeric materials for biodegradable packaging of dried longan. Blown film properties studied include morphological, mechanical and thermal properties, as well as WVP and antimicrobial activity. Finally, shelf life prediction of the dried longan is made by mathematical models based on the moisture sorption isotherm of the dried longan and WVP of the developed film. Film properties and the shelf life are related and discussed in details. To the best of our knowledge, this work is the first report on blown films of such polymer nanocomposites prepared by extrusion blowing inclusively with model demonstration of their effective function in extending shelf life of the dried longan.

2. Experimental section

2.1 Materials

PLA pellets (4043D grade) with the number–average molecular weight ($\overline{M}_n$) of 1.50×10^5 g·mol^{-1} and the weight–average molecular weight ($\overline{M}_w$) of 1.30×10^5 g·mol^{-1} were supplied by NatureWorks LLC (Minnetonka, USA). PBAT pellets (Ecoflex® F blend C1200) with the $\overline{M}_n$ of 2.44×10^4 g·mol^{-1} was provided by BASF Chemical Company (Ludwigshafen, Germany). The TBT compatibilizer, a product of Fluka Analytical (Sigma-Aldrich. Co, USA), was obtained as viscous clear liquid. Ag-loaded KT (AgKT) powder, as an antimicrobial agent (Fig. 1), was synthesized using the previously reported reduction method [5]. The yellow-brownish powder comprised 3.4 wt.% of Ag particles whose average diameters ranged from 20 to 50 nm. All polymer pellets and the antimicrobial agent were vacuum dried at 60 °C for 24 h prior to use.

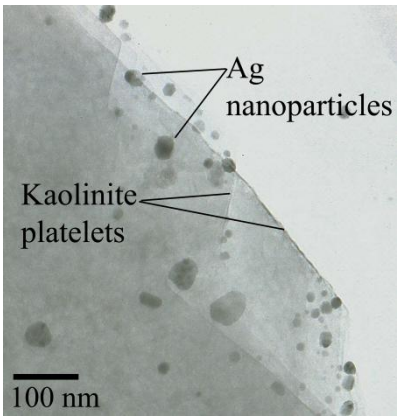

Fig. 1. TEM micrograph of AgKT powder.

2.2. Preparation of blend and nanocomposite films

Neat PLA, neat PBAT, PLA/PBAT blend, and PLA/PBAT/TBT compatibilized blend were compounded using melt blending technique in a rotating twin screw extruder (pilot scale, JSW TEX 30 α) at the temperature of feed to die zone ranging between 165 °C and 180 °C, coupled with a screw speed of 60-70 rpm. The absolute composition of PLA/PBAT blend, PLA/PBAT/TBT compatibilized blend and PLA/PBAT/TBT/AgKT nanocomposite were chosen from our previous work [5] being 70/30, 70/30/0.5 and 70/30/0.5/4, respectively, where 70, 30, 0.5 and 4 represent 70 wt.% PLA, 30 wt.% PBAT, 0.5 phr TBT and 4 phr AgKT.

Prior to the fabrication of PLA/PBAT/TBT/AgKT nanocomposite films, a masterbatch was prepared by mixing and dispersing the filler phase (AgKT) into the polymer matrix (PBAT) using an internal mixer (HAAKE Polylab internal mixer, Rheomex 252p) at 185 °C and 60 rpm for 15 min. The masterbatch was then melt blended with PLA pellets and TBT.

For the screw speed setting, the melt flow index (MFI) of the sample is an important consideration in helping to set an appropriate screw speed for safeguarding the machine and for indicating the melt-rheological properties of the polymer. The MFI of PLA/PBAT with TBT and AgKT was determined using a Davenport MFI-10 Melt Flow Indexer (Lloyd

Instruments). The samples were melted at 190 ºC and extruded through a capillary die using a 2.16 kg piston according to ASTM D1238. The weights of extrudate were measured at 10 minute intervals. The MFI value was taken as the average of at least 15 measurements.

All compounds were dried at 60 °C for 6 h prior to blown film extrusion using a single screw extruder (YJF, Ø50-800L) with specific processing parameters: a screw diameter of 50 mm, a spiral die diameter of 90 mm, a screw L/D ratio of 27, a screw speed of 90 rpm and a blow-up ratio of 2.83. The resultant film thickness was 50-55 µm. All films were stored in a controlled desiccator before test.

2.3 Characterization

Film thickness was measured by a hand-held micrometer (Mitutoyo, Japan) having a sensitivity of 0.001 mm. Ten thickness measurements were taken on each testing sample at different points. The films with thickness of approximately 50-55 µm were used throughout this study.

The transparency of the film samples with average thickness of 50 µm was expressed as percent transmittance (%T) measured at 660 nm, using a UV-visible spectrophotometer (Lambda 25, Perkin Elmer). The %T values were defined as opaque (<30%), semi-translucent (31-45%), translucent (46-75%) and optically clear (>75%).

Film morphology was investigated on fractured surfaces at ambient temperature (25.0 ºC) by a scanning electron microscope, SEM, (JSM 5910-LV, JEOL) equipped with an energy dispersive spectroscopy, EDS, (EDX-700HS, Shimadza) to quantify the amount of Ag nanoparticles. The film samples were mounted onto SEM stubs with carbon tabs attached then coated with gold using a sputter-coater.

The dispersion of the AgKT in the polymer matrix was evaluated at 25.0 ºC by a transmission electron microscope, TEM, (JSM-2010, JEOL) at an accelerating voltage of 100

kV. The TEM specimen was prepared, cryotomed at low temperature (-60 °C), and stained. TEM micrographs were obtained on thin cross-sections of the nanocomposite films.

X-ray diffractograms were acquired using an X-ray diffractometer (XRD TTRAX III, Rigaku) equipped with a filament (0.15418 nm) at a scanning rate of 2 $^{o} \cdot min^{-1}$ at room temperature. The Bragg's equation was used to determine basal spacing of AgKT.

Mechanical properties in terms of the tensile strength and elongation at break in both machine (MD) and transverse directions (TD) of the films were evaluated by a Universal Testing Machine (Lloyds LRX) following an ASTM Method D882. Initial grip separation was set at 50 mm and cross-head speed used was 5 $mm \cdot min^{-1}$. The tests were performed at 25 °C, and seven determinations were made for each sample.

Differential scanning calorimetry (DSC) was carried out using a Perkin-Elmer Differential Scanning Calorimeter (DSC7) with Pyris software. A sample (~10 mg) was placed on an aluminium pan and sealed. Under nitrogen gas atmosphere, the DSC measurement was performed from -20 to 200 °C at a heating rate of 10 $°C \cdot min^{-1}$ and then cooled quickly to -20 °C. To erase previous thermal history in all samples, re-heating was performed to record glass transition temperature (T_g), crystallization temperature (T_c), heat of crystallization (ΔH_c). melting temperature (T_m), and heat of melting (ΔH_m).

Dynamic mechanical analysis (DMA) was performed on a DMA/SDTA 861 (Mettler-Toledo, USA) to investigate thermo-mechanical properties of the specimens. The measurements were carried out at temperatures ranging from -40 to 130 °C with a heating rate of 10 $°C \cdot min^{-1}$ under a nitrogen flow in tension mode.

Thermogravimetric analysis (TGA) was performed applying a Perkin Elmer Thermogravimetric Analyzer under a nitrogen atmosphere with a 8-10 mg sample for each run. Samples were heated at a heating rate of 20 °C min^{-1} from 50 to 600 °C to record the

thermal stability of films in terms of the initial, maximum, final degradation temperature and % weight loss.

2.4 Properties testing for packaging application

WVP of the films was measured using a humidity detection sensor method though the water vapour permeation tester (Lyssy, L80-4000) at 38 °C and 90 %RH according to ASTM E96-95. The results of permeability determination were expressed in $g \cdot m^2 \cdot day^{-1} \cdot mmHg^{-1}$ for the later calculation of shelf life in this paper.

Oxygen permeability (OP) of films was measured using an Oxygen Permeation Analyzer (Model 8500, Illinois Instruments) according to the ASTM D1434 standard. OP of the films was determined at a constant temperature of 23 ºC, relative humidity of 0 %RH and oxygen gas pressure of 200 kPa. The unit of OP was expressed in $cm^{-3} \cdot m^{-2} \cdot days^{-1}$.

Light permeation through the films was measured using the same UV-visible system as previously described. The transmittance spectra of the films was reported at wavelengths of 400, 500, 600, 700 and 800 nm. The %T could refer to the UV-visible blocking ability of the filler.

Film hydrophobicity was measured using a sessile drop method with water drop of 10 µL. The results were expressed in terms of water contact angle (º, degree) on the film surface.

Ag particle migration from the films to a liquid medium was considered as a simulation of Ag release to food in this paper. Slightly acidified water solutions containing 4 wt.% acetic acid were used as a food stimulant according to European Food Safety Agency, EFSA, (EFSA 2004, 2005, 2006, 2007) and Thai Industrial Standard, TIS, (TIS 1027-2553), which are procedures for the evaluation of the specific migration of substances from plastics coming into contact with foods. The concentration of released Ag ions in the aqueous medium was measured by Atomic Absorption Spectroscopy, AAS, (Model 680, Shimadzu). Film

samples were cut into rectangular pieces of 1 × 2 × 0.01 cm^3 (a total surface area of 27.6 cm^2) and weighed. The samples were washed with milliQ water and immersed in 5 ml acidic media (4 wt.% acetic acid). The solutions were continuously shaken for 1, 4, 8, 12, and 15 days to achieve homogeneity and then centrifuged at 1800 rpm for 2 min to ensure the absence of any particulate matter in the solution. Subsequently, AAS measurements of Ag-ion solutions (1-5 mg·kg^{-1}) in the same acidic medium were conducted to establish a calibration curve for the samples in this work. All the Ag-ion concentrations presented here are the mean values of five AAS measurements.

For antimicrobial activity test, *Escherichia coli* (ATCC 35281), *Staphylococcus aureus* (ATCC 29213), *Salmonella* spp. (Group D), *Candida albicans* (CMU-2813) and *Aspergillus niger* (CMU-NKF-3) were selected from the microorganisms present in all classes of dried longan flesh based on Thai Agricultural Standard for dried longan flesh (TAS 9-2006). The antimicrobial activity of the films was determined using a viable cell count method. Film samples were cut into square pieces (10 × 10 cm^2, 1.5 g) and placed in individual sterile flasks. The bacteria were incubated separately in nutrient broth, NB, (Difco Lab. Inc., USA) at 37 ºC and in potato dextrose broth, PDB, (Difco Lab. Inc., USA) at 30 ºC, respectively, under aerobic condition for 16 h. Fifty ml of each of the prepared inoculums with the 1/10 diluted broth was aseptically added to the flasks containing the test films to obtain inocula of 1.0-4.0×10^4 colony-forming unit (CFU/ml). An inoculum of cell suspension in a flask without any test film was used as a control. The flasks were incubated using an orbital shaker and rotated at 30 rpm and 10 ºC. Cell suspension of 0.1 ml was periodically taken from the flasks, diluted serially, and plated on NB agar to test for the *Escherichia coli, Staphylococcus aureus, Salmonella* spp. and *Candida albicans* cells, or on PBD agar to test for the *Aspergillus niger* cells. The plates were incubated aerobically for 2 days at 37 ºC for

NB agar, and at 30 ºC for PDB agar media. Each experiment was performed in quadruplicate and the results were reported as the mean values in CFU/ml.

2.5 Shelf life prediction of dried longan

Moisture sorption isotherms of the dried longan were determined at 30 °C over an a_w (or RH/100) range of 0.23-0.92 using static moisture gain or loss from test samples. The dried samples in triplicate were equilibrated over saturated salt solutions inside a desiccator at 30 °C for 4-5 weeks. The a_w values of salt solutions were known for CH_3COOK (0.23), $MgCl_2$ (0.32), K_2CO_3 (0.43), $Mg(NO_3)_2$ (0.51), KI (0.67), NaCl (0.75), KCl (0.84) and K_2NO_3 (0.92) [22]. Samples were weighed every day and the equilibria were reached when three consecutive weight measurements showed no significant difference, i.e. less than 0.001 g. Sets of experiments were performed in four replications. The average value of the equilibrium moisture content (*MC*) measured by the oven method at 105 °C overnight can be calculated according to Equation (1) [23], which also refers to moisture content of the product in each RH condition.

$$MC = \frac{M_i - M_{od}}{M_{od}} \times 100 \quad (1)$$

where *MC* is in percent dry basis; M_i is sample weight in the initial condition; and M_{od} is sample weight after being oven dried at 105 °C which was recorded when sample weight remained unchanged. The experimental data on adsorption of dried longan samples were fitted by isotherm equations of BET, Oswin, Smith, Halsey, Henderson, GAB and Peleg. All models were adopted from Al-Muhtaseb et al. [24] as shown later in Table 4. The parameters of the equations were estimated using non-linear least squares fit. Low value of root mean square percentage error (*RMS %*) (Equation (2)) and coefficient of determination (r^2) converging to unity represent good fitting accuracy of predicted *MC* obtained from the used model in association with the experimental results.

$$RMS\% = \sqrt{\frac{1}{n}\left[\sum_{1}^{n}\left(\frac{MC_{\exp} - MC_{pre}}{MC_{\exp}}\right)^2\right]} \times 100 \quad (2)$$

where MC_{exp} and MC_{pre} are MC values, experimentally obtained and predicted by the model, respectively, and n is the number of data points.

For a moisture sensitive product like dried longan, shelf life depending mainly on the uptake of a certain amount of moisture into or loss from the package can be estimated from moisture sorption isotherms using the Equation (3) [1]

$$\ln \frac{MC_e - MC_i}{MC_e - MC_c} = \frac{k}{x}\frac{A}{W_s}\frac{p_v^o}{m}t_{sl} \quad (3)$$

where MC_i is initial moisture content; MC_c is critical moisture content (the moisture content level at which the product appearance becomes unacceptably changed); MC_e is equilibrium moisture content (the moisture content level when the product is in equilibrium with the external RH); k/x ($g \cdot m^2 \cdot days^{-1} \cdot mmHg^{-1}$) is the moisture permeance through the packaging film; A (m^2) is the packaging film area, W_s (g solids) is weight of dry food solids; p^0_v (mm Hg) is the water vapour pressure at the storage temperature; m is the slope of the linearized isotherm portion in the range of interest (i.e., from MC_i to MC_c); and, t_{sl} (days) is the estimated shelf-life [19]. The MC_c and MC_e in the test condition at a given RH can be established from the product sorption isotherm.

2.6 Statistical analysis

Film properties were obtained in triplicate using individually prepared films. The replicated experimental results were provided with mean standard deviation values (± SD). The antimicrobial activity data were analyzed by analysis of variance (ANOVA). Ducan's multiple-range test ($P < 0.05$) was adopted to detect differences among treatment mean values for the film properties. Statistical analysis was conducted using SPSS 17.0 for Windows.

3. Results and discussion

3.1. Physical appearance

Photographs of rolls of different blown films are shown in Fig 2a. Both neat PLA (Fig 2a, A) and PBAT (Fig 2a, B) films with average thickness of 50 µm were optically clear (%T = 90.57±0.37 and 88.60 ± 1.19, respectively). Blending of the neat polymers results in semi-translucent film (Fig 2a, C) (%T = 55.57 ± 4.34) due to immiscibility between the two polymers. Phase boundaries formed from such phase separation hinders transport of UV-visible light through the film. Although addition of TBT into PLA/PBAT blend still causes film semi-translucence, the presence of TBT improves compatibility between the parent polymers which in turn increases %T (68.22 ± 0.92). The variance in %T (SD value) also decreases, indicating more homogeneity of the films which is to be confirmed by SEM study discussed later in this paper.

After the incorporation of AgKT, the yellowish-brown nanocomposite film appears translucent with %T reducing to 42.08 ± 3.70. This is owing to the filler particles that causes light scattering (Fig. 2b) although PBAT phase becomes smaller with TBT incorporated. Thus the blocking effect of light path by AgKT plays a dominant role in delivering translucent manner over better homogeneity between the two polymers and over crystallization effect occurred due to induced PLA crystallization as discussed later herein.

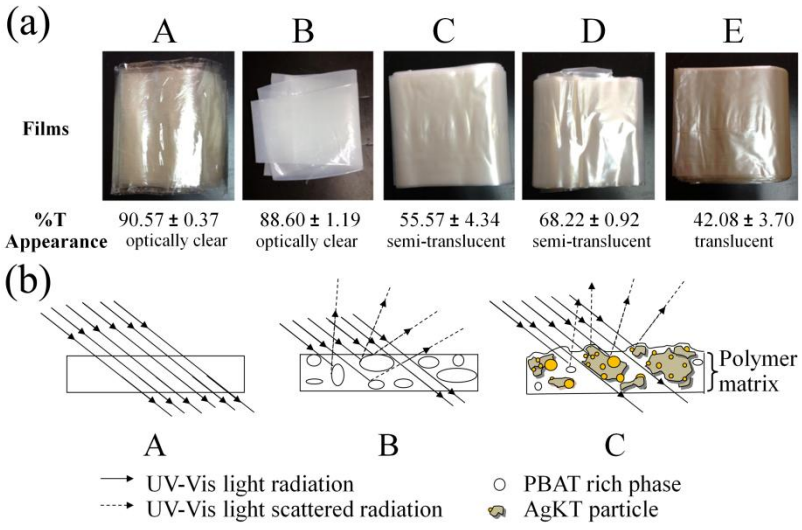

Fig. 2. (a) physical appearance and %T values at 660 nm of (A) neat PLA, (B) neat PBAT, (C) PLA/PBAT blend (D) PLA/PBAT/TBT compatibilized blend and (E) PLA/PBAT/TBT/AgKT nanocomposite films and (b) cross-sectional schematic illustration of UV-visible radiation permeating though (A) the neat polymer, (b) PLA/PBAT blend and (C) PLA/PBAT/TBT/AgKT composite films.

3.2. Morphology evaluation

Fig. 3a-c show the fractural surface morphologies of the films. It can be seen that the compatibilized blend with TBT added (Fig. 3b) demonstrates smoother topography, suggesting more compatibility between PLA and PBAT. Such an observation reflects an effectiveness of TBT as the compatibilizer promoting strong interaction between the two polymer phases during melt-extrusion. Because PLA-*co*-PBAT copolymers are formed through transesterification reactions in the presence of TBT during melt processing [3], the interfacial adhesion between the two phases is enhanced by the PLA-*co*-PBAT copolymers acting as compatibilizers [3-5, 25].

In addition, transesterification between the PLA and PBAT to give PLA-*co*-PBAT for improving the blend compatibility could be induced by changing the torque due to the presence of peroxide TBT-compatibilizer during the melting process in the internal mixer, as reported in previous work [4,5,25]. As a result of the formation of PLA-*co*-PBAT, the torque increased significantly after adding the TBT-compatibilizer and then decreased slightly before becoming stable. Chain scission of the polymer leading to a decrease in molecular weight has also been observed at high concentrations of TBT (0.6 phr) resulting in a decrease in torque [4,5,25].

Moreover, the melt-rheological properties in terms of the melt flow index (MFI) of the polymer (from the twin-screw extruder) could give an indication of the polymer chain mobility and the compatibility enhancement by PLA-*co*-PBAT formation via the role of TBT. Thus, the decrease in MFI from 4.85 (PLA/PABT) to 4.72 (PLA/PBAT/TBT) g/10 min when adding 0.5 phr of TBT indicated an increase in melt viscosity due to PLA-*co*-PBAT formation in the system. Similarly, the addition of AgKT also decreased the MFI from 4.72 of (PLA/PBAT/TBT) to 3.99 (PLA/PBAT/TBT/AgKT) g/10 min due to the formation of a clay network with polymer chains in between the KT platelets resulting in a decrease in melt fluidity. These observed changes in MFI are consistent with linear rheological behavior [26].

The polymer matrix of the nanocomposite films (Fig. 3c) also correspondingly appears to have homogeneity in spite of AgKT embedment. Higher roughness is observed for the nanocomposite sample as a result of the AgKT particles which can be detected by Energy Dispersive Spectroscopy (EDS). EDS spectra of Fig. 3c reveals Ag amount of 0.133 wt.% (supplementary data) corresponding to the calculated Ag amount of approximately 0.132 wt.% for this particular 4 phr AgKT added into the polymer matrix.

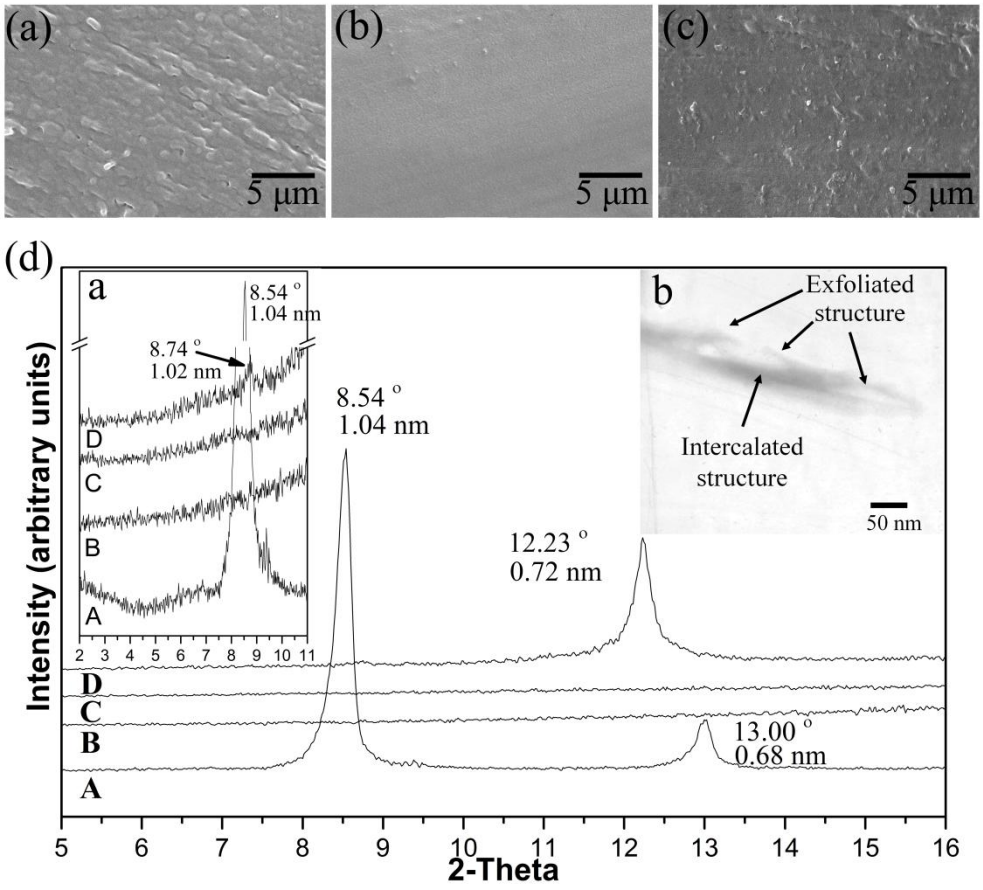

Fig. 3. Fractural surface morphologies of (a) PLA/PBAT blend, (b) PLA/PBAT/TBT compatibilized blend, (c) PLA/PBAT/TBT/AgKT nanocomposite films at 5k magnification and (d) XRD patterns of (A) AgKT nanocomposite powder, (B) PLA/PBAT blend, (C) compatibilized PLA/PBAT/TBT blend and (D) PLA/PBAT/TBT/AgKT nanocomposite films. Inset in (d) shows (a) an XRD plot from 2-11 degrees of 2-Theta and (b) a TEM micrograph of the nanocomposite film at 100k magnification.

The microstructure of the nanocomposite film is revealed by the TEM image (inset b in Fig. 3d) showing dark and bright regions of the AgKT layers as an intercalated and exfoliated structure in the polymer matrix respectively. This is in good agreement with the XRD observations (Fig. 3d). Particularly, the XRD patterns show absence of AgKT peak at 8.54 º (1.04 nm) when incorporated into the compatibilized polymer blend corresponding to

the exfoliated structure of AgKT in the polymer matrix in the TEM results. However, the dispersed-AgKT had only a few intercalated structures in the polymer matrix from the XRD results (inset a in Fig. 3d) which show only a small peak at 8.74 º (1.02 nm). Both TEM and XRD suggest the AgKT dispersion is intercalated-exfoliated in nature. A greater number of AgKT layers of the related plane is thus likely to exfoliate in the matrix. Although the exfoliated nanocomposites have generally been reported to exhibit the best properties, such as good barrier properties due to the optimal interaction between the clay and the polymer [6], an additional advantage in this work which is due to the silver nanoparticles is the long-lasting antibacterial activity as described later.

Moreover, a possible cause of the molecular TBT-compatibilizer structure is that it contains both hydrophobic and hydrophilic groups which help to disperse the AgKT in the polymer matrix. While the hydrophobic part of TBT can interact with the hydrophobic part of clay, the hydrophilic part can interact with the polar components of the polymer. Hence, the probability of clay layer aggregation in the polymer matrix is minimized. Furthermore, clay gallery separation due to polymer chain segment insertion into the clay layers is additionally reflected from an increase of d-spacing from 0.68 nm (13.00 º) to 0.72 nm (12.23 º) as illustrated by the TEM result.

3.3. Mechanical properties

The tensile test results of films in MD and TD (Fig. 4a-b and Table 1) are in almost similar trend. PLA films show hardness and brittleness with high Young's modulus and high tensile strength but low elongation at break. Whereas PBAT films exhibit high toughness and flexibility as demonstrated by high elongation at break but low tensile strength and low Young's modulus. Blending PLA with PBAT at 70/30 ratio decreases these mechanical parameters compared with those of the neat polymers especially PLA. Particularly, the tensile

strength, elongation at break and Young's modulus of PLA/PBAT blend films are lowered. Such inferior characteristics are attributed to poor interaction between the two polymer components because of phase separation and a significant difference in solubility parameters between PLA and PBAT (10.1 $(cal \cdot cm^{-3})^{1/2}$ and 22.95 $(cal \cdot cm^{-3})^{1/2}$, respectively) [27].

The opposite trend of the mechanical properties is observed for the PLA/PBAT/TBT compatibilized blend. TBT acts as an effective compatibilizer that can enhance mechanical parameters, especially tensile strength, elongation at break and Young's modulus. Such an observation demonstrates better compatibility between PLA and PBAT by PLA-*co*-PBAT formation via transesterification during melt extrusion corresponding to SEM results.

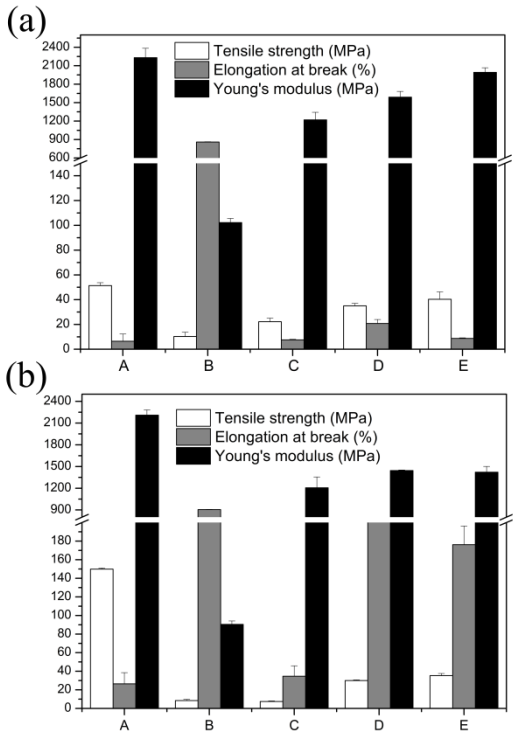

Fig. 4. Mechanical properties in (a) MD and (b) TD of (A) neat PLA , (B) neat PBAT, (C) PLA/PBAT blend (D) PLA/PBAT/TBT compatibilized blend and (E) PLA/PBAT/TBT/AgKT nanocomposite films.

Compared with compatibilized blends' properties, the nanocomposite films comprising AgKT show higher tensile strength and a slight decrease in elongation at break. This result may be a consequence of restriction of polymer chain movement by the filler existence. Furthermore, directional variation of the mechanical properties is the unique behavior of film samples. Typically, tensile strength, elongation at break and Young's modulus in MD are higher than those in TD which may be attributed to the different degree of materials orientation in both directions. During film blowing process, the orientation of polymer chains occurred in melt state as a result of shear stress along with stretching in the die. Due to the tension force in MD, polymer chains are comparatively more extended in MD to cause higher degree of orientation than in TD. Although extended chain crystals occurred in MD from the tension force that caused a higher degree of orientation than in TD, the induced crystals were grown in the vertical direction (TD) by the clay platelets. Consequently, due to the polymer reinforcement by the induced crystals and clay molecular orientation which interacted with the polymer chains in TD, the strength of the samples in TD was higher than in MD.

Table 1 Mechanical properties of neat PLA, neat PBAT, PLA/PBAT blend, PLA/PBAT/TBT compatibilized blend and PLA/PBAT/TBT/AgKT nanocomposite films in MD and TD.

Film	Machine direction (MD)			Transverse direction (TD)		
	Tensile strength (MPa)	Elongation at break (%)	Young's modulus (MPa)	Tensile strength (MPa)	Elongation at break (%)	Young's modulus (MPa)
Neat PLA	149.87 ± 1.18	26.48 ± 11.94	2210.30 ± 71.28	51.35 ± 2.40	6.51 ± 5.79	2231.59 ± 152.27
Neat PBAT	8.41 ± 1.34	904.71 ± 2.34	90.44 ± 3.67	10.33 ± 3.40	859.70 ± 4.47	102.21 ± 3.37
PLA/PBAT	7.48 ± 0.53	34.59 ± 11.27	1206.03 ± 150.41	22.24 ± 2.84	7.57 ± 0.45	1220.47 ± 121.78
PLA/PBAT/TBT	30.05 ± 0.70	224.10 ± 2.43	1444.60 ± 6.75	35.02 ± 2.01	20.85 ± 3.16	1589.44 ± 92.44
PLA/PBAT/TBT/AgKT	35.29 ± 2.33	176.22 ± 20.11	1420.90 ± 79.62	40.33 ± 5.94	8.75 ± 0.45	1992.53 ± 73.28

3.4. Thermal properties

DSC was mainly used to qualitatively evaluate thermal behavior of film specimens and to investigate crystalline phase that occurred in the samples. DSC curves (Fig. 5a and Table 2)

indicate T_g of neat PLA film at ~ 54.9 °C whereas T_g of neat PBAT cannot be observed over test temperature range. Based on Fox equation and typical T_g of neat PBAT [28], predicted T_g of PLA/PBAT blend is 38.0 ºC. However, phase separation between PLA and PBAT plays a vital role in deviating PLA/PBAT blend's T_g to 59.9 °C. In contrast, the films comprising the compatibilizer have their T_g values of 54.8 °C (compatibilized blend) and 54.4 °C (nanocomposite) converging to the calculated blend's T_g due to compatibility improving by transesterification during the melting process.

The T_c and ΔH_c of PLA/PBAT blend, TBT-compatibilized blend and PLA/PBAT/TBT/AgKT nanocomposite film are observed at 117.8 °C (13.4 J g^{-1}), 112.8 °C (15.4 J g^{-1}) and 112.5 °C (16.3 J g^{-1}), respectively, while both neat films do not show their T_c and ΔH_c. It can be assumed that this is a PLA crystallization peak [5]. With such a decrease in T_c and an increase in ΔH_c, both TBT and AgKT therefore tend to facilitate crystallization by acting as nucleating agents. Moreover, endothermic melting peaks are also observed as shoulder with TBT presence, indicating that TBT induces different crystallite sizes of PLA.

Although T_m values of PLA/PBAT blend, TBT compatibilized-blend and PLA/PBAT/TBT/AgKT nanocomposite films are almost identical, ΔH_m of these three different samples are observably different, i.e. 19.4, 19.9 and 21.3 J g^{-1}, respectively. Thus, crystallite amount formed can be ordered in a sequence as in nanocomposite > compatibilized blend > blend. Although T_m values of PLA/PBAT blend, TBT compatibilized-blend and PLA/PBAT/TBT/AgKT nanocomposite films are almost identical, ΔH_m of these three different samples are observably different, i.e. 19.4, 19.9 and 21.3 J g^{-1}, respectively. Thus, crystallite amount formed can be ordered in a sequence as in nanocomposite > compatibilized blend > blend. It should be noted here that both TBT and AgKT are nucleating agents which can influence the crystallization of PLA in a PLA/PBAT blend, with AgKT being a stronger

nucleating agent than TBT. In the case of TBT, chain scission of PLA via TBT-catalyzed transesterification can facilitate molecular rearrangement and the formation of smaller-sized crystallites. In comparison, AgKT gave rise to an even larger increase in crystallinity (higher ΔH_m) than TBT due to the effect of the clay platelets in orienting the PLA chains in such a way as to induce crystallization.

Table 2 Thermal properties of neat PLA, neat PBAT, PLA/PBAT blend, PLA/PBAT/TBT compatibilized blend and PLA/PBAT/TBT/AgKT nanocomposite films characterized by different techniques**.**

Film	DSC					DMA		TGA
	T_g (°C)	T_c (°C)	$\triangle H_c$ (J g^{-1})	T_m (°C)	$\triangle H_m$ (J g^{-1})	Tan δ (peak) (°C)	E' at 30 °C (MPa)	T_d range (°C)
Neat PLA	54.9	-	-	149.3	2.1	74.2	3183.49	316.0 - 402.3
Neat PBAT	n/d	-	-	110.8	11.3	-15.0	100.28	307.4 - 527.3
PLA/PBAT	59.9	117.8	13.4	150.7	19.4	-14.7, 72.1	1774.53	277.3 - 504.2
PLA/PBAT/TBT	54.8	112.8	15.4	148.3	19.9	-14.8, 70.5	2034.31	295.8 - 521.6
PLA/PBAT/TBT/AgKT	54.4	112.5	16.3	148.7	21.3	-15.9, 69.8	2115.52	311.0 - 540.1

DMA analysis was performed to determine storage modulus (E') which relates to thermo-mechanical properties of the films. In addition, Tan δ can be obtained to indicate polymers' T_g which suggests compatibility of the polymer constituents (Fig. 5b-c and Table 2).

At ambient temperature (~ 30.0 °C), E' (Fig. 5b) of PLA decreases from 3,183.49 to 1,774.53 MPa with the presence of PBAT (E' ~ 100.28 MPa). In addition, E' enhancements to 2,034.31 and 2,115.52 MPa are observed when TBT and AgKT were incorporated into the blend, respectively. Such results agree well with the mechanical properties previously mentioned in that PBAT introduces flexibility to the blends while TBT improves polymer compatibility. AgKT also enhances blend stiffness through good reinforcing effects in the

compatibilized blend matrix, leading to probable efficient stress transferred from the polymer matrix to clay layers. These E' increments are additionally attributed to nucleating effect of the TBT and AgKT.

Since DMA possesses higher sensitivity in determining polymers' T_g compared with DSC technique, T_g of the PLA/PBAT blend as obtained from DMA seems to well follow Fox's equation as they diverge to the predicted T_g. Fig. 5c and Table 2 represent Tan δ associated with T_g of the samples. T_g values of neat PLA and PBAT films are revealed at 74.2 and -15.0 °C, respectively. When the PLA/PBAT blend is studied, two T_g values are found at -14.7 and 72.1 °C, being assigned to T_g of PLA and PBAT, respectively. Incorporation of TBT to form the compatibilized blend suppresses PLA's T_g (70.5 °C) closer to the predicted blend's T_g; hence, the compatibilizer is clearly found improving interfacial adhesion between PLA and PBAT. However, the AgKT added does not affect the polymer compatibility as observed from unclear divergent trend of PLA and PBAT's T_g to the predicted T_g.

TGA thermograms of neat polymers, their blends and nanocomposites are shown in Fig. 5d-e. Neat PLA film shows an onset of thermal degradation temperature ($T_{d,onset}$) at 316.0ºC, maximum degradation temperature ($T_{d,max}$) at 381.4 ºC and final degradation temperature ($T_{d,final}$) at 402.3 ºC whereas PBAT film is found higher thermally stable than the PLA with a $T_{d,onset}$ at 307.4 ºC, $T_{d,max}$ at 465.7 ºC and $T_{d,final}$ at 527.3 ºC. The PLA/PBAT blend sample, with a T_d range of 277.3-504.2 ºC, has thermal degradation taking place in two different steps associated with the contribution of the two neat polymers, further suggesting a lack of miscibility between the blend constituents. The first degradation step of $T_{d,max}$ at 381.1 ºC is PLA decomposition, while the one at 425.9 ºC is assigned to PBAT thermal decomposition. The addition of TBT yields a T_d range of 295.8-521.6 ºC which is higher than that in PLA/PBAT blend case. The similar trend of T_d increase is obtained with AgKT incorporation into the compatibilized blend. The T_d range is further shifted up to 311.0-540.1

ºC. Therefore, both TBT and AgKT effectively work as thermal stability enhancers for this particular blend system.

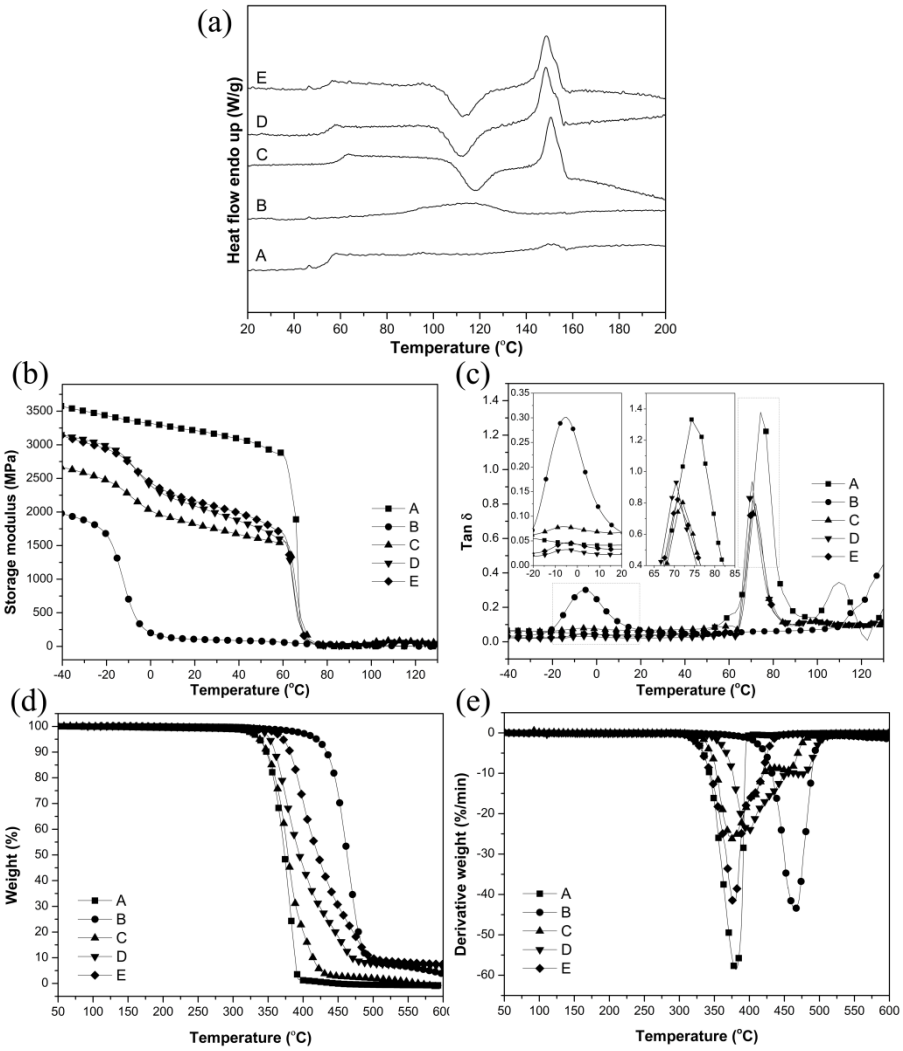

Fig. 5. (a) DSC thermograms, (b) *E'* and (c) Tan δ plots from DMA analysis in tension mode, (d) %weight loss and (e) derivative curves from TGA analysis of (A) neat PLA, (B) neat PBAT, (C) PLA/PBAT blend (D) PLA/PBAT/TBT compatibilized blend and (E) PLA/PBAT/TBT/AgKT nanocomposite films.

3.5. Barrier properties and hydrophobicity

WVP and OP values of neat PLA are lower than those of PBAT film (Fig. 6a and Table 3). From the relative sizes of the repeating units of PLA and PBAT, it is to be expected that that PLA will be more crystalline than PBAT. In addition, comparatively lower WVP of neat PLA film may be attributed to PLA's higher hydrophobicity degree whereas PBAT has a lower contact angle due to its structure comprising more polar repeating units than in PLA. Surprisingly, a significant deviation of contact angle and especially OP values is observed for PLA/PBAT blend film. This could be attributed to incompatibility between the neat polymers, leading to PBAT phase embedded in PLA matrix and, thus, high surface roughness created. Subsequent addition of TBT, nevertheless, smoothens the PLA/PBAT blend surface and in turn brings the deviation back to typical level. Moreover, it can be observed that these three parameters (WVP, OP and contact angle) of the PLA/PBAT/TBT/AgKT nanocomposite film are lower than those of the compatibilized blend films. Such a phenomenon can be described as a preferred orientation of layered silicate along machine direction that is created within the polymer blend matrix, forming longer tortuous paths for water vapour and oxygen molecules to permeate through. Formation of dense crystalline regions induced by TBT and AgKT also lowers WVP and OP. Polymer crystallite nucleation contributes to a decrease in polarity of the polymer chains as well, accordingly, the higher water contact angle and increased surface hydrophobicity resulted. Another reason for the enhanced hydrophobicity of the nanocomposite is an increase in film roughness owing to AgKT embedment and presence at the surface (Fig 2b, C) [29].

Since the dried longan is sensitive to colour change from UV radiation, barrier property of the films to UV light is investigated in terms of %T as shown in Table 3 and Fig. 6b. Compared with PLA, PBAT is more efficient in blocking UV-visible region (400-800 nm). Blending PLA with PBAT yields %T lying between those of the parent polymers (Fig. 2b, B). The TBT-compatibilized blend allows higher UV permeation and lower UV scattering

compared with the incompatible blend. The explanation is that TBT makes PBAT phase smaller and film surface smoother. Regions at which UV rays are scattered are therefore lower in number. Nevertheless, the UV permeability decreases considerably with AgKT presence because of the filler blocking UV radiation passage (Fig. 2b, C) and high roughness created on polymer surface acting as UV scattering areas.

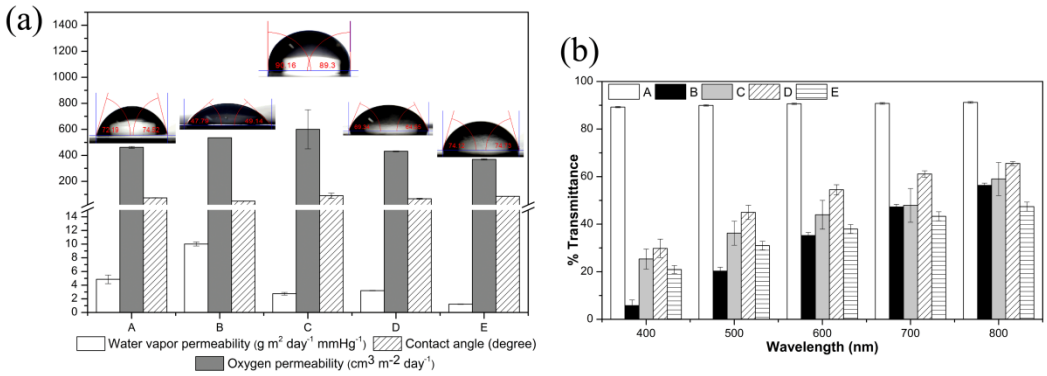

Fig. 6. Film barrier properties and hydrophobicity: (a) WVP, OP and contact angle and (b) %T through various films of (A) neat PLA, (B) neat PBAT, (C) PLA/PBAT blend, (D) PLA/PBAT/TBT compatibilized blend and (E) PLA/PBAT/TBT/AgKT nanocomposite films.

Table 3 Barrier properties and contact angle of neat PLA, neat PBAT, PLA/PBAT blend, PLA/PBAT/TBT compatibilized blend and PLA/PBAT/TBT/AgKT nanocomposite films**.**

Film	**WVP ($g\ m^2\ day^{-1}\ mmHg^{-1}$)**	**OP ($cm^3\ m^{-2}\ day^{-1}$)**	**%T of UV light (at 400 nm)**	**Contact angle (º)**
Neat PLA	4.85 ± 0.64	461.72 ± 7.11	89.23 ± 0.27	73.36 ± 1.65
Neat PBAT	10.02 ± 0.30	535.70 ± 0.00	5.79 ± 2.33	48.47 ± 0.95
PLA/PBAT	2.74 ± 0.20	600.00 ± 150.00	25.33 ± 4.22	90.00 ± 20.00
PLA/PBAT/TBT	3.21 ± 0.04	431.53 ± 3.00	29.82 ± 3.89	66.94 ± 3.39
PLA/PBAT/TBT/AgKT	1.22 ± 0.04	369.35 ± 5.59	20.94 ± 1.66	85.42 ± 0.43

3.6. Silver ion release

Release kinetics of Ag ions is the key property to evaluate the applicability of the polymer nanocomposite films. As shown in Fig. 7a, PLA/PBAT/TBT/AgKT nanocomposite films release Ag ions that sit on the outer surface of KT layers with a rapid initial releasing rate of

0.0036 $mg \cdot kg^{-1} \cdot day^{-1}$within the first 5 days, consistent with previous work [5]. Such an initial Ag release is thus controlled only by the diffusion though polymer matrix. Subsequent Ag release at a decreased rate of 0.0021 $mg \cdot kg^{-1} \cdot day^{-1}$ during day 5-14 is from those sitting in interlamellar space of the KT. The key features manipulating this second releasing stage (day 5-14) are potentially both Ag ion diffusion though the matrix and tortuous paths of KT layers hindering the ion migration. The proposed mechanism of diffusion-controlled release of Ag ions is illustrated as Fig. 7b. Ability of the nanocomposite film to extend Ag release period could benefit antimicrobial activity in the package from the view point of long term food maintenance.

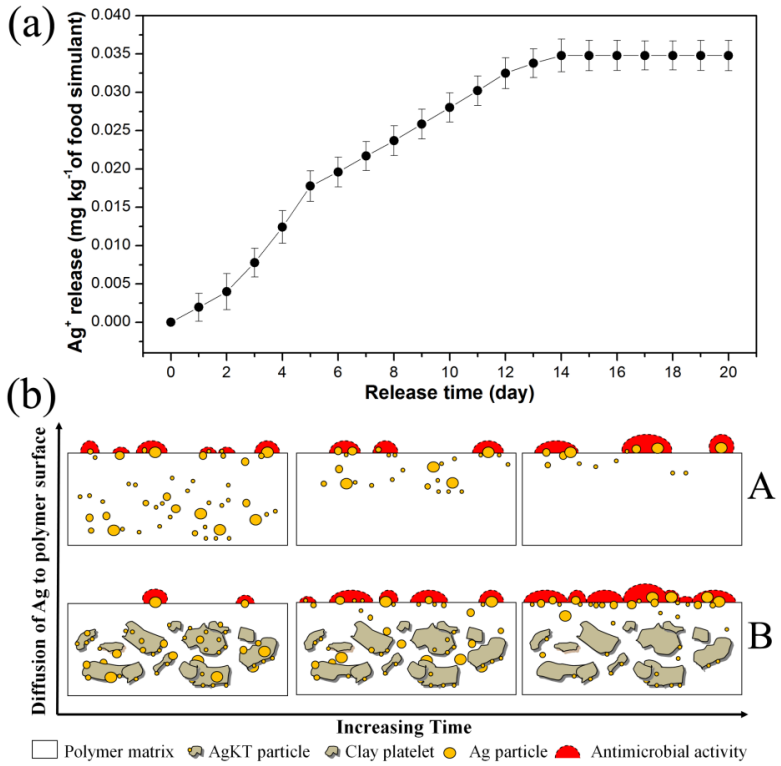

Fig. 7. (a) Ag ion release from the nanocomposite blown film to food simulant as a function of time and (b) graphical drawing of Ag diffusion-controlled release in the polymer matrix: (A) Ag ions without KT presence and (B) Ag ions attached on and inserted between layered KT.

In addition, the concentration of released Ag ions at day 14 onwards is stable at ~ 0.0348 mg kg^{-1}. Such a Ag migration is below the limit of 0.05 mg kg^{-1} as defined by the European Food Safety Authority (EFSA 2004, 2005, 2006, 2007) and the Ag (as lead or cadmium) release limit of 100 mg kg^{-1} as determined by Thai Industrial Standard of plastic bag for food (TIS 1027-2553; ISBN 978-974-292-869-8). Accordingly, the developed nanocomposite film can be used safely as an Ag-based package in contact with food.

3.7. Antimicrobial activity of the films

The antibacterial activity analyses of the films were performed after 7 days (Ag ion release rate = 0.021 mg $kg^{-1}day^{-1}$) in media culture to achieve microbial growth. The PLA/PBAT/TBT compatibilized blend and PLA/PBAT/TBT/AgKT nanocomposite films were tested against five spoilage microorganisms of dried longan: *S. aureus, E. coli, C.albican, Salmonella* spp. and especially *A. niger* as shown in Fig. 8.

As expected, the compatibilized-blend film shows some antimicrobial activity against *S. aureus, C. albican* and *Salmonella* spp. while CFU reductions (Fig. 8) of all microbial species are found mainly due to biocidal activity of AgKT in the nanocomposite films. It can be noticed that the nanocomposite films exhibite ~96% bactericidity against *A.niger*, 92% against *Salmonella* spp, 86% against *S. aureus*, 50% against *C. albican* and 33 % against *E. coli*. In this study, it is postulated that the antimicrobial action of PLA/PBAT/TBT compatibilized film is attributable to the reactive oxygen species (negative electrons generate O^{2-}, and positive electric holes generate hydroxyl radicals) which is able to kill bacteria and viruses [30]. For PLA/PBAT/TBT/AgKT nanocomposite film, Ag ions being released from the layered KT function as the key antimicrobial agent killing the microorganisms and thus able to control the microbial growth. Over all tested microorganisms, the nanocomposite film is most active in killing *A.niger*. Thus, it is promising to adopt Ag as a potential biocidal agent

in dried longan packaging applications. The particular nanocomposite system is also safe for the product as specified by the EFSA and TIS standards.

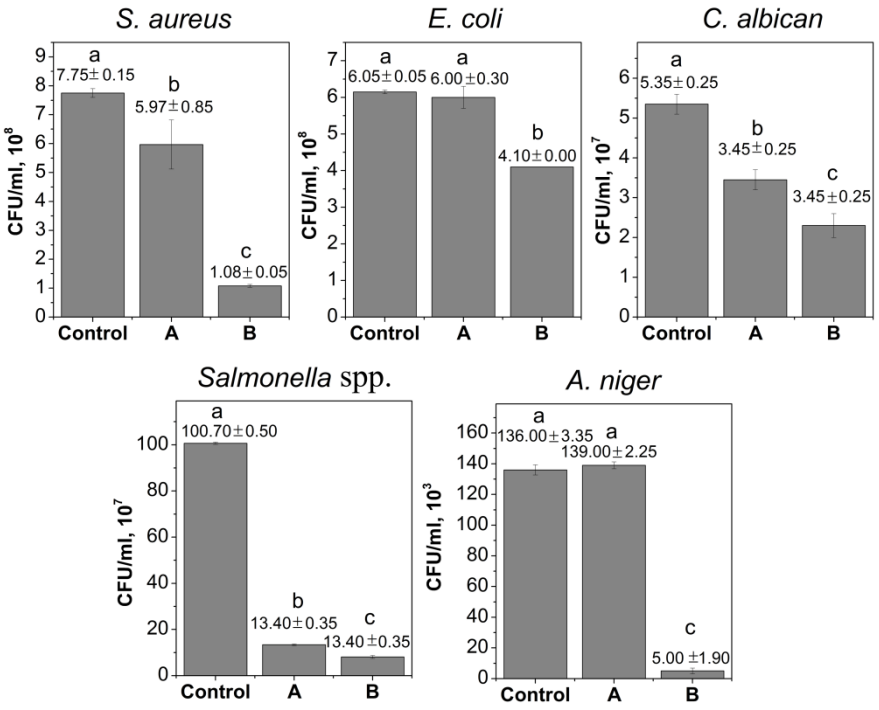

Fig. 8. Antimicrobial activity of (A) PLA/PBAT/TBT compatibilized blend and (B) PLA/PBAT/TBT/AgKT nanocomposite films against five microbe species in comparison with the control after 7 days.

3.8. Hypothesis on the correlation between nanocomposite film properties and shelf life extension of dried longan

Functionality of the PLA/PBAT/TBT/AgKT nanocomposite film (Fig. 9a) can be correlated with its performance in extending dried longan shelf life. Specifically, AgKT improves film barrier properties by its layered structure creating tortuous paths for the gaseous phases (Fig.9a; A and B). The AgKT as well as TBT additionally act as nucleating agents to induce polymer crystallization (Fig. 9b) as discussed in our DSC results. Thus, the formed crystallites significantly hinder passage of moisture and oxygen gas required for microorganism growth in the developed package. The browning reaction of the dried longan flesh is effectively

retarded by the incorporation of AgKT, protecting the longan from UV-visible radiation. The nanolayers finely embedded in the polymer matrix exert a certain UV-visible light blocking action by scattering, reflecting, dispersing the incident light (Fig. 9a; C) and thereby reducing the light absorbance. Such a result is attributed to high film surface roughness and superior insulator to light transport of the solid AgKT.

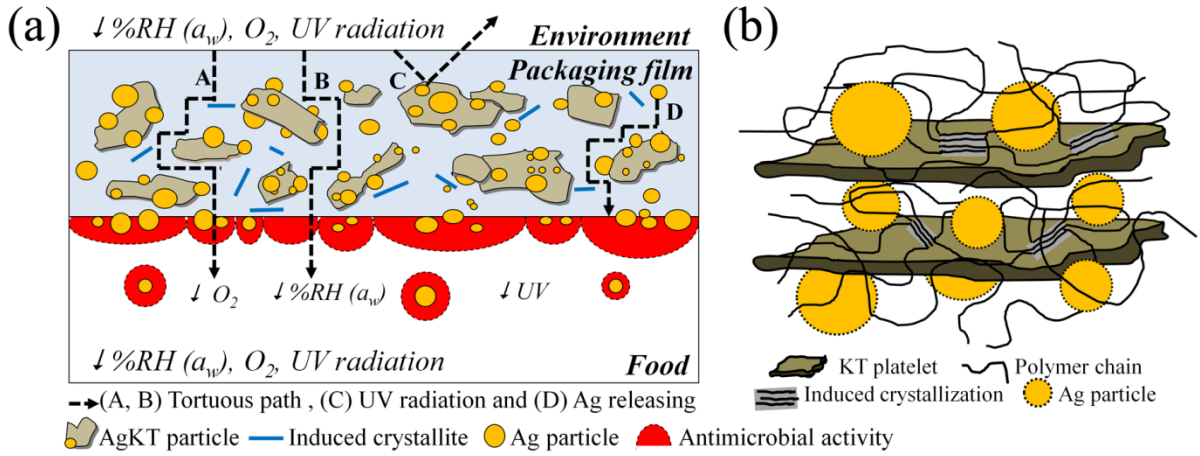

Fig. 9. Graphical illustration of (a) packaging PLA/PBAT/TBT/AgKT nanocomposite film in contact with food and its function as a barrier for water vapour, oxygen molecules and UV radiation. Dashed lines represent (A and B) tortuous paths for water vapour and oxygen molecules, (C) UV-radiation scattering paths and (D) Ag releasing paths and (b) occurrence of induced crystallization in the polymer matrix.

An additional crucial role of the AgKT in extending the shelf life is controlled release of Ag ions from KT substrate in polymer matrix. This longer Ag releasing duration could prolong antimicrobial activity in the longan flesh. The beginning state of Ag release is from those sitting on the KT surface while the prolonged Ag release was from the ions coming out from the KT's interlamellar space. Working in such a manner, the KT functions as Ag-ion releasing agent discussed previously in this report. Furthermore, induced crystallites act as a barrier phase increasing diffusion paths of Ag ions to film surface (Fig. 9a, D), thus controlled release could be achieved.

Based on this hypothesis, the incorporation of Ag KT into the PLA/PBAT/TBT compatibilized blend enables a possible route to fabricate an antimicrobial packaging nanocomposite for dried longan. The particular system could prolong Ag-ion releasing duration, leading to long term benefits to antibacterial activity and hence improved longan preservation while maintaining the quality of the packaged longan.

3.9. Shelf life prediction

3.9.1 Moisture sorption kinetics and isotherm

Moisture sorption kinetics curves of dried longan are provided in Fig. 10a. Initial moisture adsorption is clearly rapid especially at high %RH. Then the curves tend to level off with increasing time and the plateaus are shown, indicating that equilibrium state is reached. At high %RH (> 67.9%), a great amount of moisture is transferred, hence longer adsorption time proceeds to reach equilibrium. The dried longan shows adsorption behaviuor at all studied %RH (21.6-92.5%), because all %RH of the environment is higher than initial moisture content (MC_i) of the dried longan (12.5%). Since market-acceptable moisture content, according to Thai Agricultural Standard (TAS 8-2006), is referenced at 12-18%, critical moisture content (MC_c) here is assigned as 18%.

Equilibria of moisture sorption curves (Fig.10a) at each %RH are plotted against a_w in terms of equilibrium moisture content (*MC)* as shown in Fig. 10b. The moisture sorption isotherm curve of the dried longan as obtained experimentally (dash line, Fig. 10b), can be classified as type II sigmoidal isotherm for soluble materials. This resultant curve is typically asymptotic as its a_w shifts towards 1 [31]. The *MC* is almost linearly proportional to a_w, but it dramatically scales up at $a_w > 0.67$.

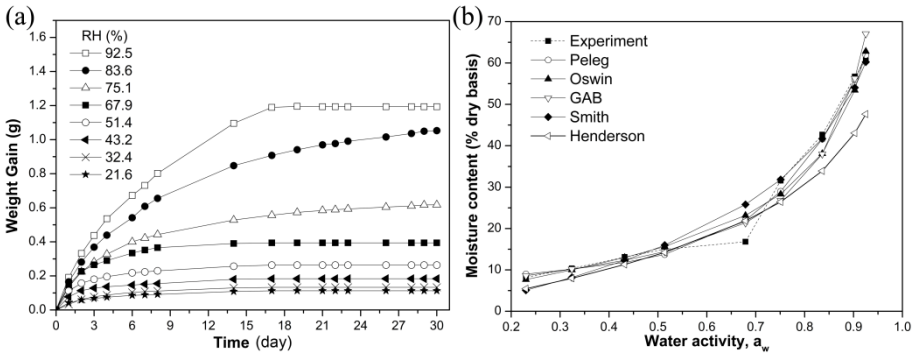

Fig. 10. (a) moisture sorption curves of dried longan at various relative humidities as a function of time and (b) comparative plot between experimentally obtained moisture sorption isotherm and those predicted by other sorption isotherm models for the dried longan.

Measured sorption data are fitted to several model expressions as shown in Table 4. A comparative trend made between experimental moisture sorption isotherm and those predicted by various sorption isotherm models for dried longan is illustrated as Fig. 10b. Calculated model constants, r^2, and %RMS derived from each model for the product are represented in Table 4. Monolayer moisture content (M_o) values of the dried longan are predicted using GAB and BET models. The M_o indicates that the amount of moisture adsorbed on a single layer by binding sites [32] on longan flesh is in an acceptable M_o range of 7.60-7.89 (< 10%) on dry weight basis [32]. Among all models used, the Peleg model shows best fit with respect to highest r^2 (0.9877) and with a minimum %RMS of 2.14. The Peleg model is therefore considered as the best to describe the experimental adsorption data for dried longan in the a_w range of 0.22-0.93 in this work.

Table 4 Sorption isotherm models used herein [24] with relevant calculated constant parameters, coefficient of determination and percentage of root mean square error for dried longan.

Sorption isotherm model	Mathematical expression [24]	Constant parameter	r^2	%RMS
B.E.T.	$MC = \frac{M_o C a_w}{(1-a_w)(1+(C-1)a_w)}$	M_o = 7.8864 C = 15.0952	0.9380	16.87
Oswin	$MC = C(\frac{a_w}{1-a_w})^n$	C = 15.1576 n = 0.5658	0.9743	3.14
Smith	$MC = C_1 + C_2 \ln(1-a_w)$	C_1 = -1.1101 C_2 = -23.6860	0.9684	3.43
Halsey	$MC = (-\frac{C}{\ln a_w})^{\frac{1}{n}}$	C = 15.6923 n = 0.7042	0.8707	8.38
Henderson	$MC = (-\frac{\ln(1-a_w)}{C})^{\frac{1}{n}}$	C = 0.0436 n = 1.1057	0.9650	7.47
G.A.B.	$MC = \frac{M_o C K a_w}{(1-Ka_w)(1-Ka_w+CKa_w)}$	M_o = 7.6002 K = 0.9591 C = 26.3808	0.9704	3.46
Peleg	$MC = C_1 a_w^{c_3} + C_2 a_w^{c_4}$	C_1 = 14.3246 C_2 = 0.3192 C_3 = 72.4413 C_4 = 5.2939	0.9877	2.14

MC = equilibrium moisture content, M_0 = monolayer moisture content, a_w = water activity and C, n, C_1, C_2, C_3, C_4, K = constants specific to individual mathematical expression.

3.9.2. Shelf life simulation of dried longan

Predicted shelf life of dried longan in each package type (0.1524 × 0.1524 m^2) at 30.0 ºC and 65 %RH (a_w = 0.65) storage conditions was calculated using Equation (3). *MC* values obtained from experimental adsorption moisture isotherm in terms of MC_e (16.49% at a_w = 0.65) and MC_c (18% at a_w = 0.50), respectively, were inserted into Equation (3). Moreover, the MC_e and MC_c predicted by Peleg model were obtained by putting C_1, C_2, C_3 and C_4 into Peleg mathematical expression at a_w = 0.65 and 0.50 for MC_e and MC_c calculation, respectively. The resultant shelf lives of the dried longan predicted by experimental adsorption moisture isotherm and Peleg model are tabulated in Table 5.

Table 5 Comparison of experimental and predicted dried longan shelf lives (using Peleg model) of the compatibilized blend and nanocomposite films compared with OPP film.

Shelf life (day)	**PLA/PBAT/TBT film**	**PLA/PBAT/TBT/AgKT film**	**OPP film**
Experiment	117.16	308.27	390.55
Peleg model	117.13	308.20	396.17

WVP of OPP film is ~1.07 $g \cdot m^2 \cdot day^{-1} \cdot mmHg^{-1}$.

It is found that shelf life predicted by the Peleg model and that obtained experimentally are almost identical for both PLA/PBAT/TBT compatibilized blend and PLA/PBAT/TBT/AgKT nanocomposite films. As expected, AgKT interestingly exhibits its performance in enhancing the shelf life of more than two folds (from ~117 to 308 days) due to several reasons as described previously. As the predicted shelf lives here based mainly on WVP, there is a great difference between the shelf life obtained from the nanocomposite and commercial OPP films (~80 days). The actual shelf life of the former case would possibly increase to approach the latter one if antimicrobial effect for the nanocomposite film is taken into account. Since shelf life from the nanocomposite film is rather long (~10 months) for the dried longan, the developed nanocomposite film, as it is, could be extensively applied to several dried food products as environmentally benign polymeric materials to replace conventional non-biodegradable plastics.

4. Conclusions

Biodegradable blown films of nanocomposite based on PLA were successfully prepared in this work. AgKT played a major role in enhancing several properties of compatibilized PLA/PBAT blend including mechanical properties due to fine embedment of the AgKT that caused efficient interaction between polymer matrix and the filler. Thermal stability of the compatibilized blend was also increased with AgKT presence. Moisture barrier property was

essentially improved owing to effective nucleation induced by TBT compatibilizer and AgKT. Controlled release of Ag nanoparticles, and thus antimicrobial activity, was uniquely engineered using nanostructured KT. Particularly, retarded Ag-ion release was achieved by transport of the ions embedded between KT's interlamellar space. Concentration of released Ag ions also complied with the EFSA and TIS standards for plastic bag in contact with food. Such effectiveness in antimicrobial activity of the nanocomposite film was demonstrated in terms of considerable growth inhibition of fungi especially *A. Niger* commonly found in dried longan.

The Peleg model was selected for shelf life prediction since it provided best fit to the moisture sorption isotherm data of the dried longan. Because of the previously mentioned functionality of the AgKT in improving moisture barrier property of the compatibilzed blend film, longan shelf life predicted based on WVP of the AgKT-incorporated nanocomposite film was longer than that of the compatibilized blend film. The nanocomposite film delivered dried longan shelf life of up to 308 days which may cover storage duration of other dried food products. Application of the polymer nanocomposite materials in this paper is believed to extend to other various dried food with its benefit in being environmentally friendly that supports sustainability of polymer material uses.

Acknowledgements

This work was financially supported by the Human Resource Development in Science Project (Science Achievement Scholarship of Thailand, SAST) and the Graduate School, Chiang Mai University (for Sutinee Girdthep), the Thailand Research Fund (TRF) and the Commission on Higher Education (CHE) (Grant No. MRG4780109 for Winita Punyodom), the National Science and Technology Development Agency Northern Region (NSTDA Northern Network) and the "Trade Standard Compliance and Innovations for Agri-Food Supply Chains in

Thailand and Neighbouring Countries Project" under the Science and Technology Research Institute, Chiang Mai University (for Patnarin Worajittiphon and Winita Punyodom).

Appendix A. Supplementary material

Supplementary data associated with this article can be found, in the online version.

References

[1] Escobedo-Avellaneda Z, Velazquez G, Torres JA, Welti-Chanes J. LWT-Food Sci Technol 2012;47:364-70.

[2] Gvozdenović JJ, Ajka AR, Lazic VL, Tepić AN, Svrzić GV. APTEFF 2007;38:21-8.

[3] Lin S, Guo W, Chen C, Ma J, Wang B. Mater Des 2012;36:604-8.

[4] Coltelli M-B, Toncelli C, Ciardelli F, Bronco S. Polym Degrad Stab 2011;96(5):982-90.

[5] Girdthep S, Worajittiphon P, Molloy R, Leejarkpai T, Punyodom W. Polym Int. revision.

[6] Alexandre M, Dubois P. Mat Sci Eng R 2000;28:1-63.

[7] Paul DR, Robeson LM. Polymer 2008;49:3187-204.

[8] Ammala A, Hill AJ, Lawrence KA, Tran T. J Appl Polym Sci 2007;104:1377-81.

[9] Sun D, Li B, Li Y, Yu C, Zhang B, Fei H. Mater Res Bull 2011;46:101-104.

[10] Patakfalvi R, Oszkó A, Dékány I. Colloids Surf A Physicochem Eng Asp 2003;220:45-54.

[11] Patakfalvi R, Dékány I. Appl Clay Sci 2004;25:149-59.

[12] Cabedo Ls, Giménez E, Lagaron JM, Gavara R, Saura JJ. Polymer 2004;45:5233-8.

[13] Matusik J, Stodolak E, Bahranowski K. Appl Clay Sci 2011;51:102-9.

[14] Mbey JA, Hoppe S, Thomas F. Carbohydr Polym 2012;88:213-22.

[15] Aimé Mbey J, Hoppe S, Thomas F. Polym Composite.in press.

[16] Busolo MA, Lagaron JM. Innov Food Sci Emerg Technol 2012;16:211-7.

[17] Qiu X, Wang H, Zhou C, Li D, Liu Y, Yan C. J Taiwan Inst Chem E. in press.

[18] Chen Y, Li Y. Int J Pharm 2003;255:217-25.

[19] Welti-Chanes J, Pérez E, Guerrero-Beltran JA, Alzamora SM, Vergara-Balderas F. Applications of water activity management in the food industry. In Barbosa-Cánovas GV, Fontana A, Schmidt S, Labuza TP (Eds.). Water activity in foods. Oxford, UK: Blackwell Publishing Ltd.;2008. p341-57.

[20] Escobedo-Avellaneda Z, Pérez-Pérez MC, Bárcenas-Pozos ME, Welti-Chanes J. J Food Process Eng 2011;34:1931-45.

[21] Goula AM, Karapantsios TD, Achilias DS, Adamopoulos KG. J Food Eng 2008;85:73-83.

[22] Greenspan L. J Res Nat Bureau Stand 1977;81A:89-102.

[23] AOAC. Official methods of analysis. Washington D.C.: Association of Official Agricultural Chemists;1984.

[24] Al-Muhtaseb AH, McMinn WAM, Magee TRA. J Food Eng 2004;61:297-307.

[25] Coltelli M-B,S Bronco, Chinea C. Polym Degrad Stab 2010;96:332-41.

[26] Wang K, Liang S, D Jinni, Y Hong, Z Qin, F Qiang, D Xia, W Dujin, Han C. C. Polymer 2006;47:7131-44.

[27] Kumar M, Mohanty S, Nayak SK, Rahail Parvaiz M. Bioresour Technol 2010;101:8406-15.

[28] Abdelwahab MA, Flynn A, Chiou B-S, Imam S, Orts W, Chiellini E. Polym Degrad Stab 2012;97:1822-8.

[29] Marmur A. Langmuir 2003;19:8343-8.

[30] Amparo L, Elsa L, Pierre AP, Raul T, Avelina F. Trends Food Sci Technol 2012;24:19-29.

[31] Bell LN, Labuza TP. Moisture sorption: practical aspects of isotherm measurement and use. American Association of Cereal Chemists, St. Paul, MN.;2000. p33-56.

[32] Rosa GS, Moraes MA, Pinto LAA. LWT-Food Sci Technol 2010;43:415-20.

[33] Labuza TP, Kaanane A, Chen JY. J Food Sci 1985;50:385-92.

Figure 1

Click here to download high resolution image

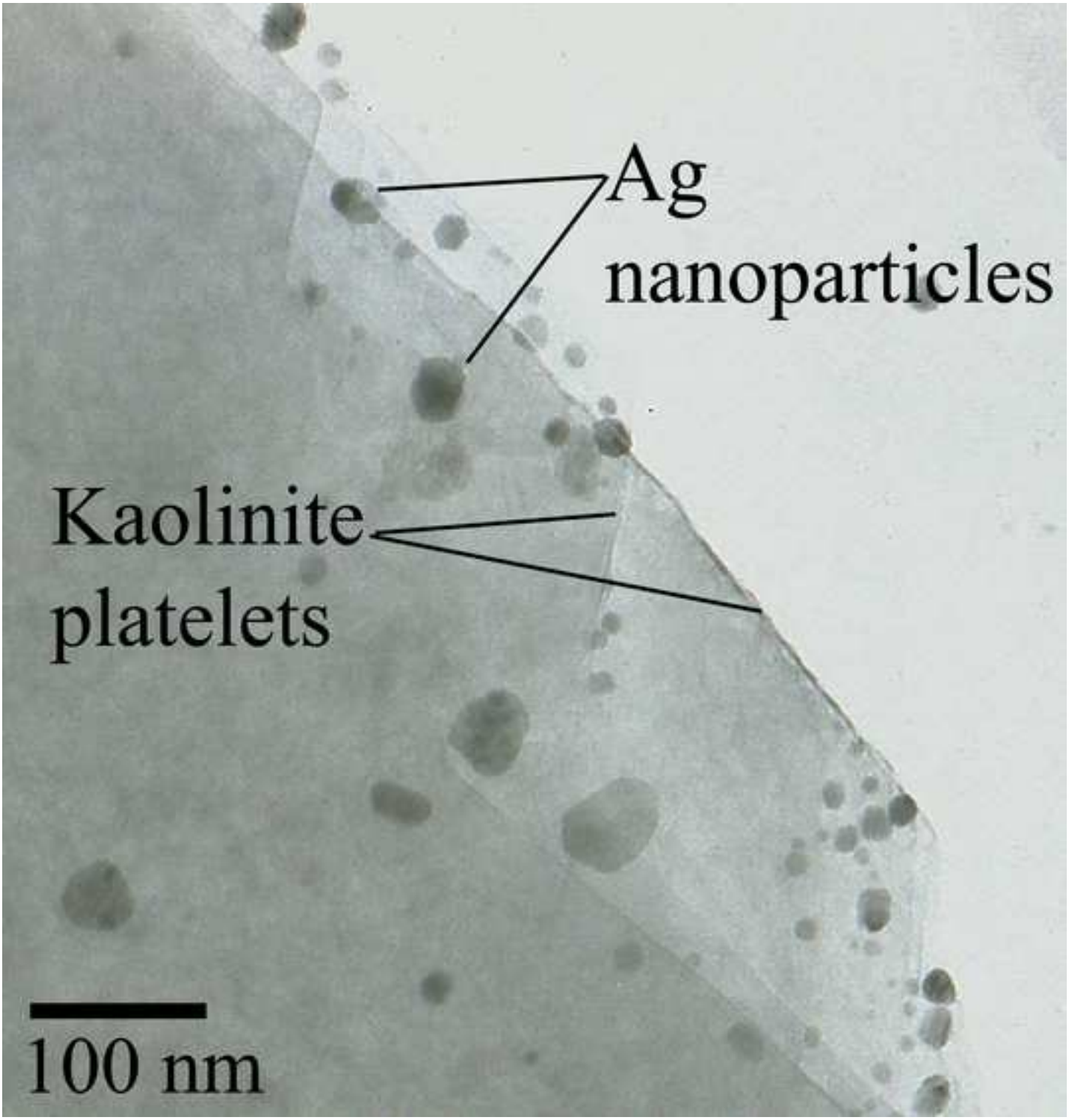

Figure 2
Click here to download high resolution image

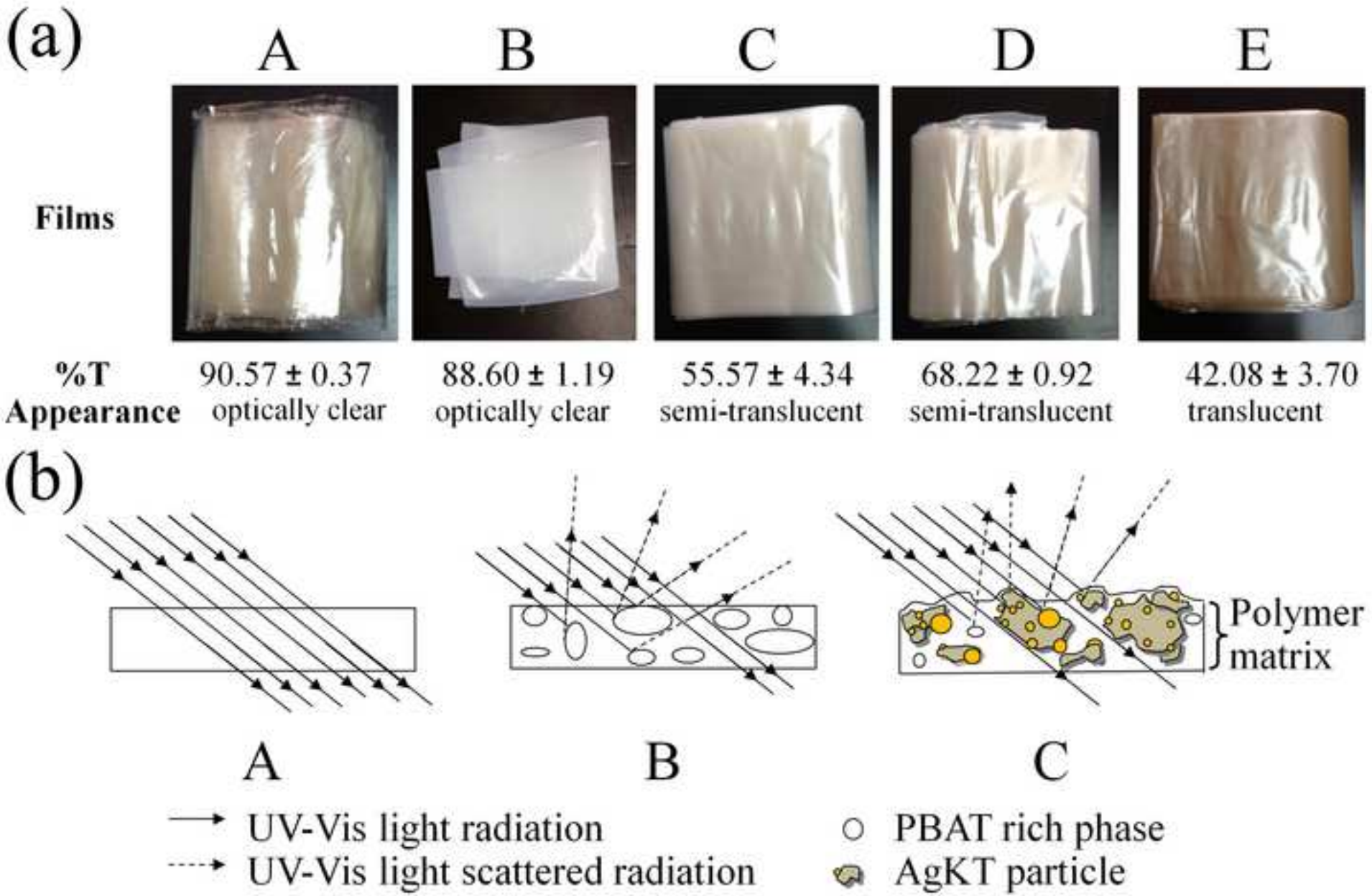

Figure 3

Click here to download high resolution image

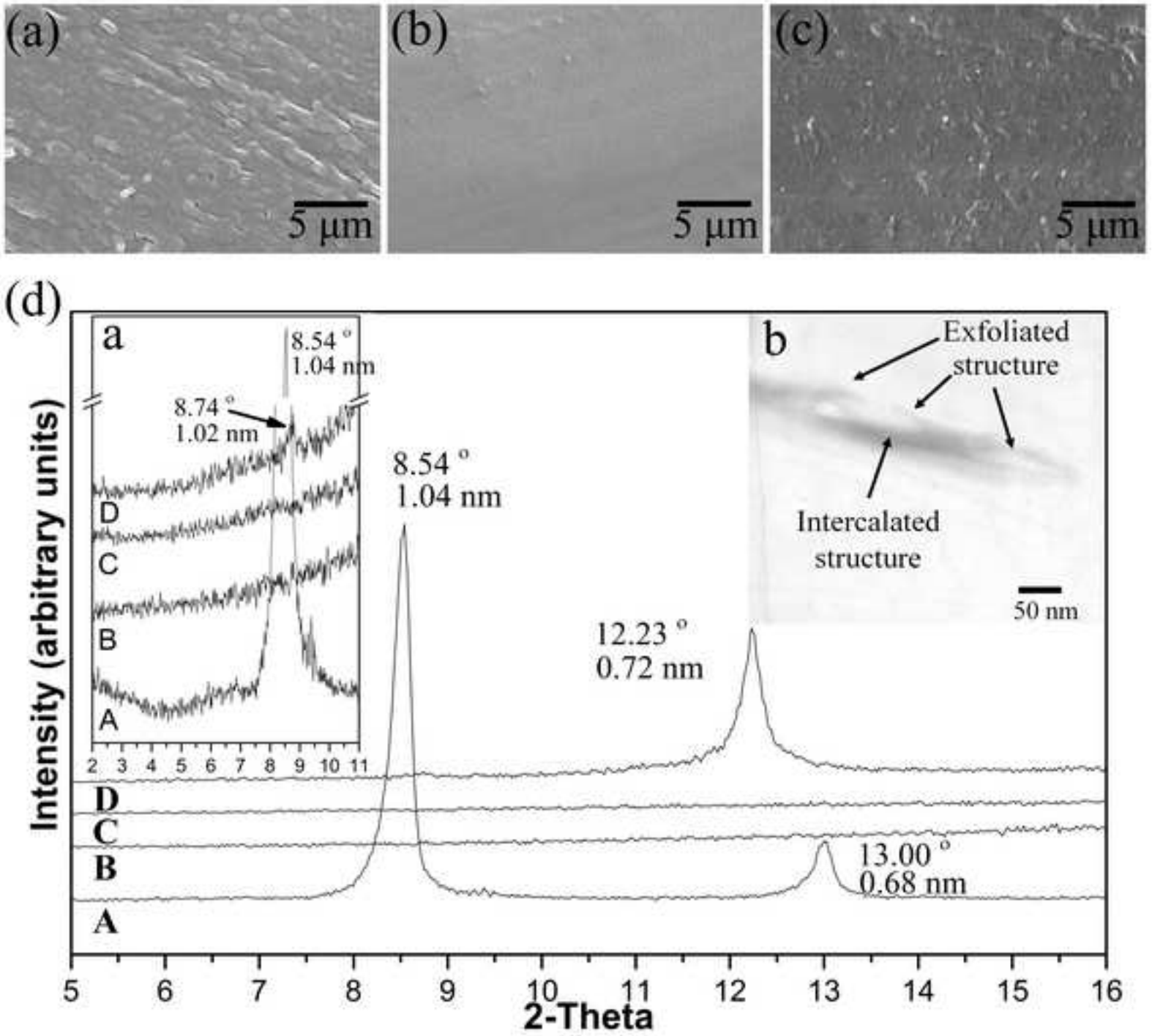

Figure 4

Click here to download high resolution image

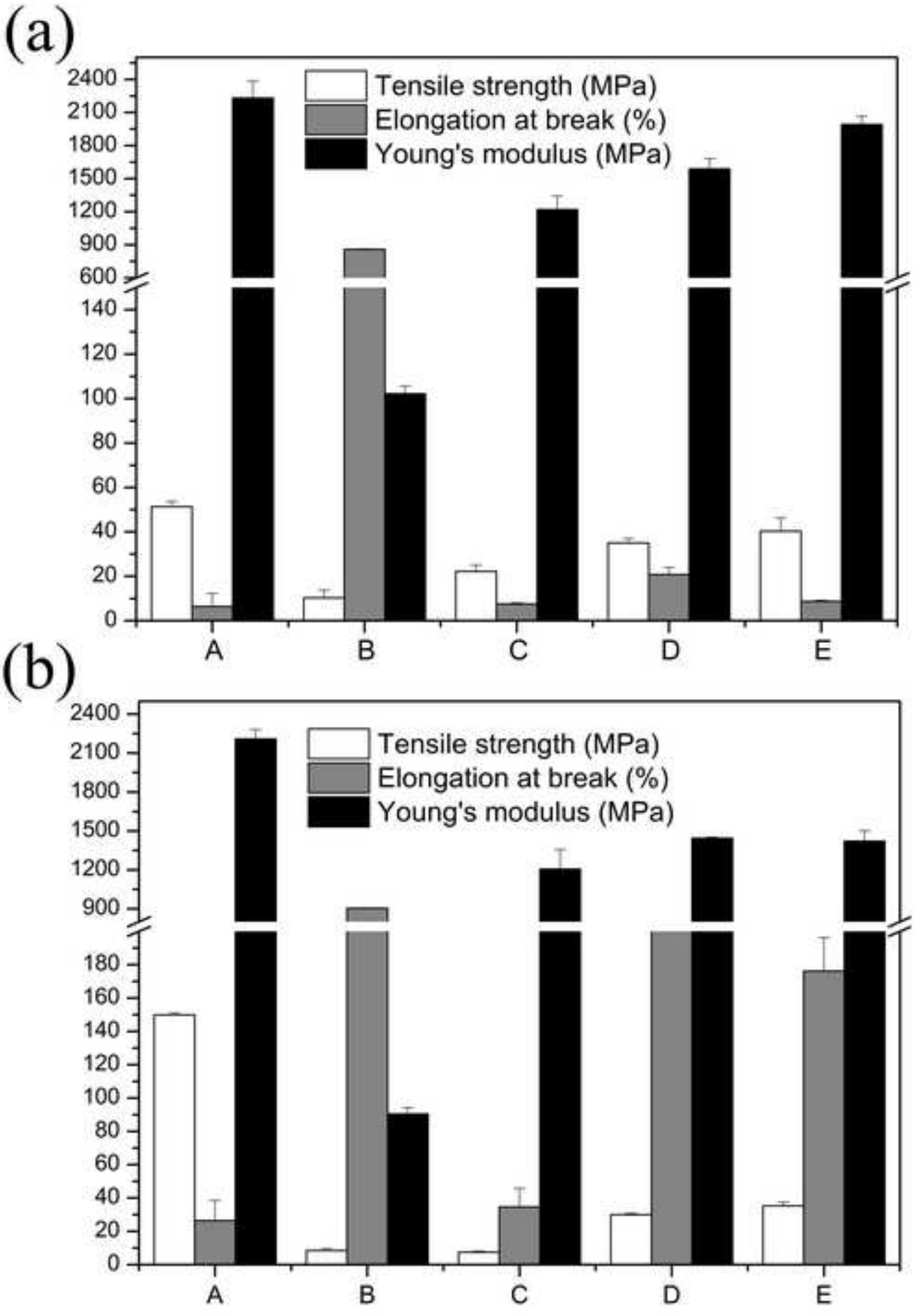

Figure 5

Click here to download high resolution image

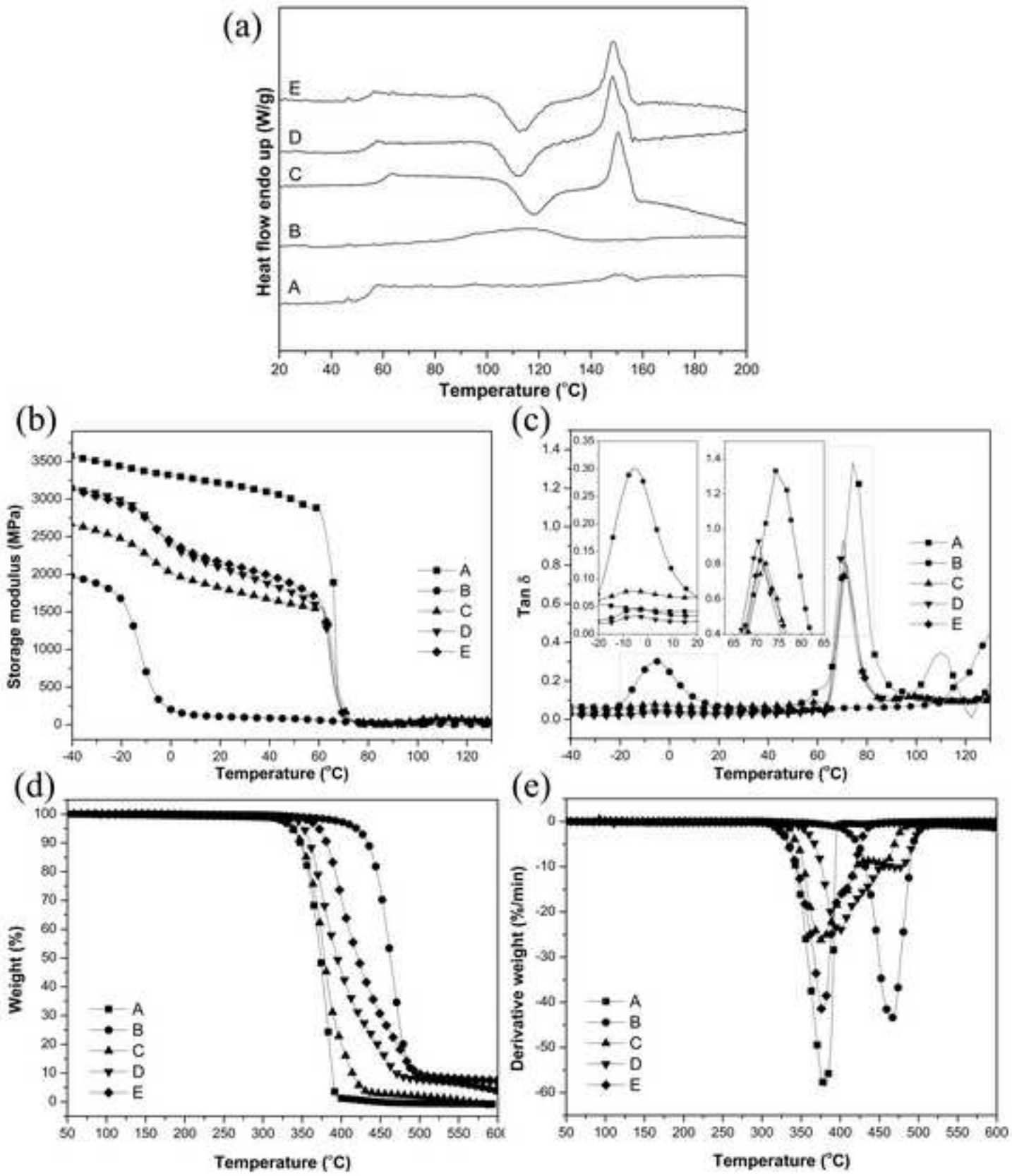

Figure 6

Click here to download high resolution image

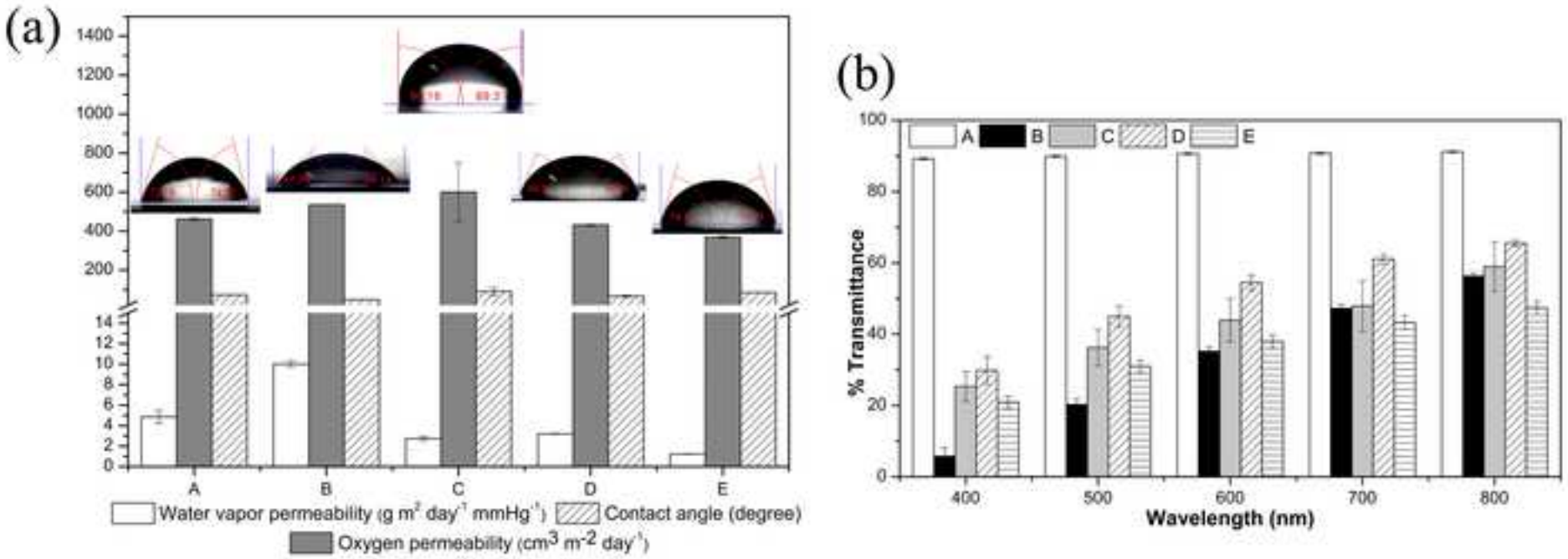

Figure 7

Click here to download high resolution image

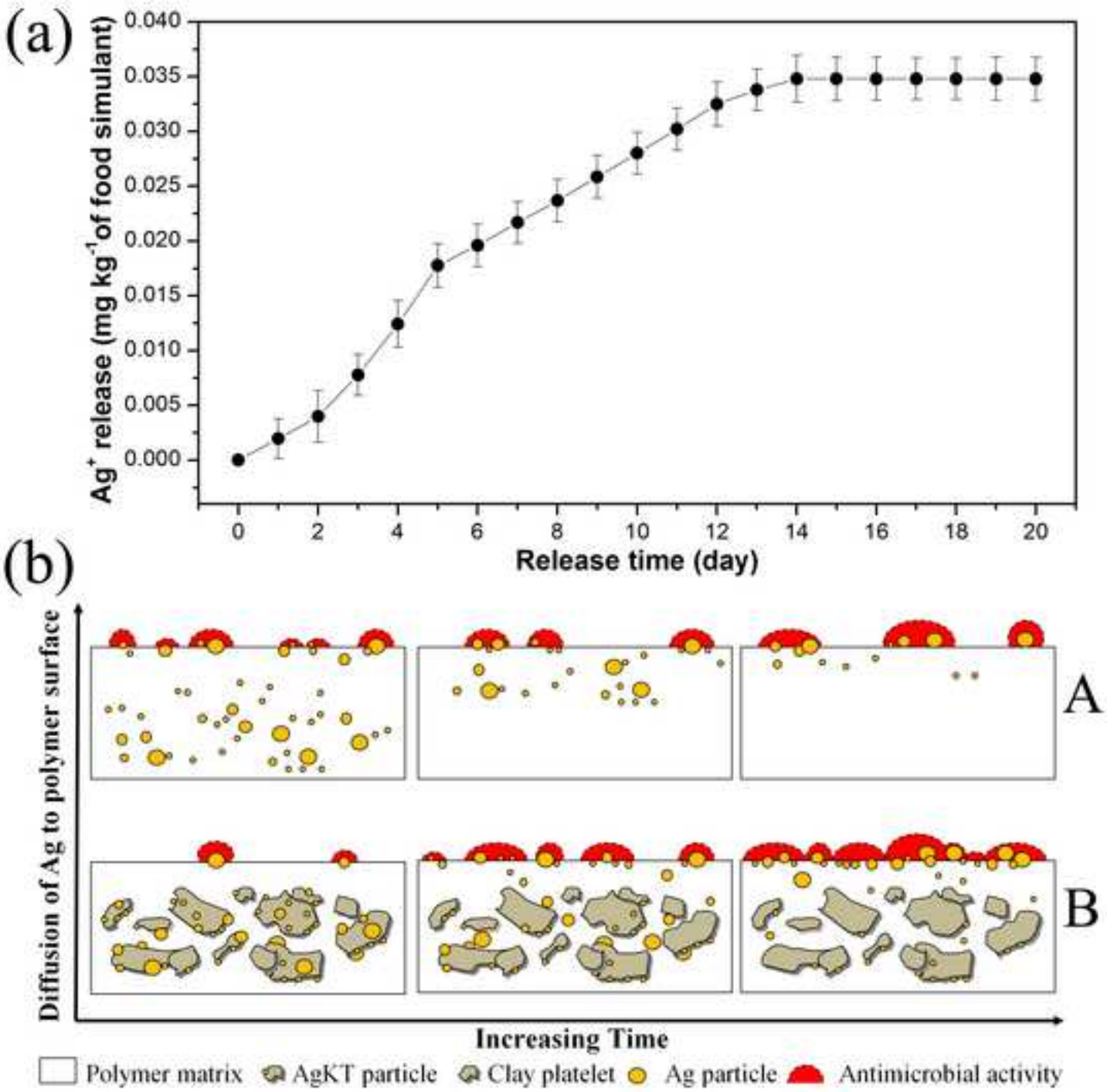

Figure 8

Click here to download high resolution image

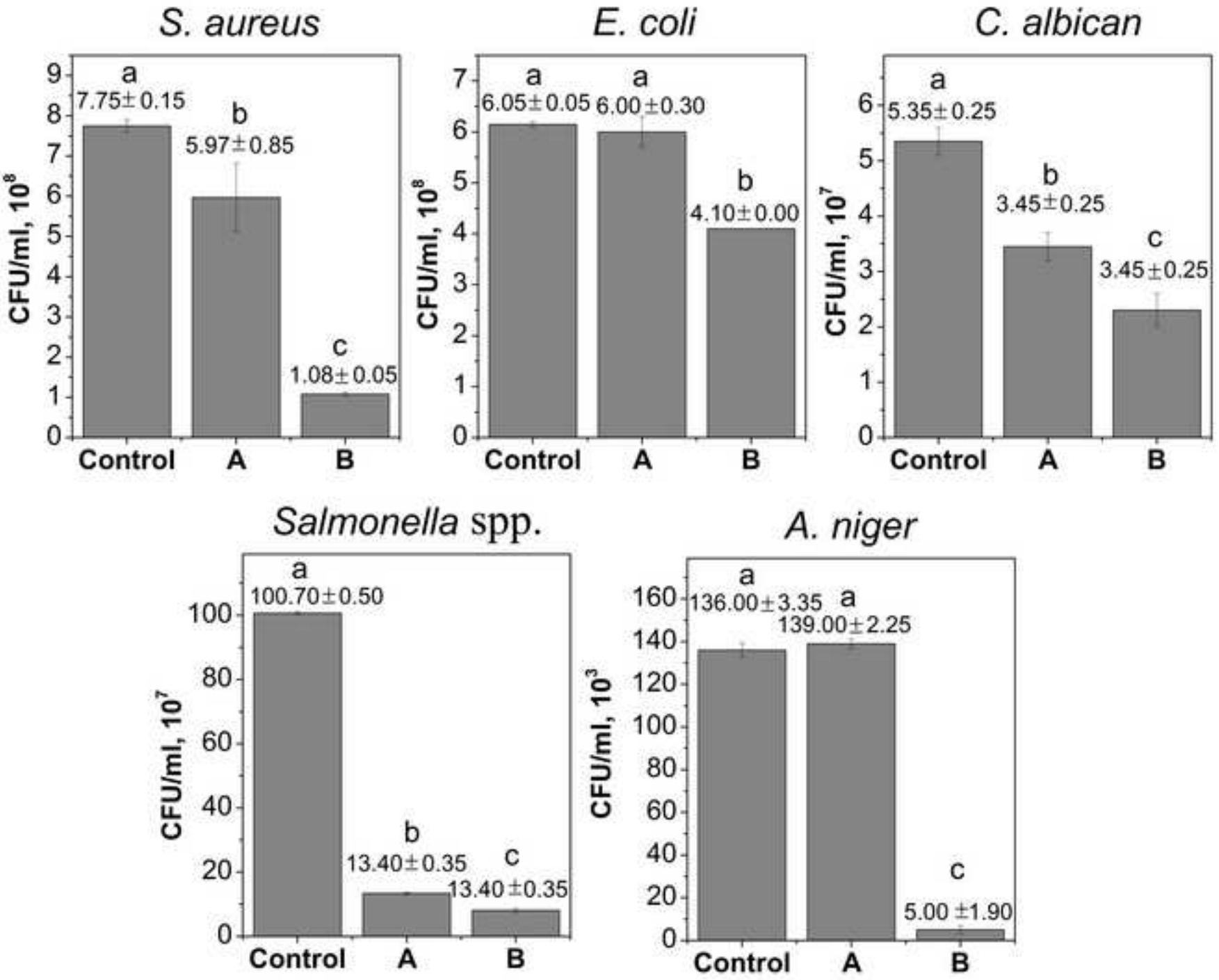

Figure 9

Click here to download high resolution image

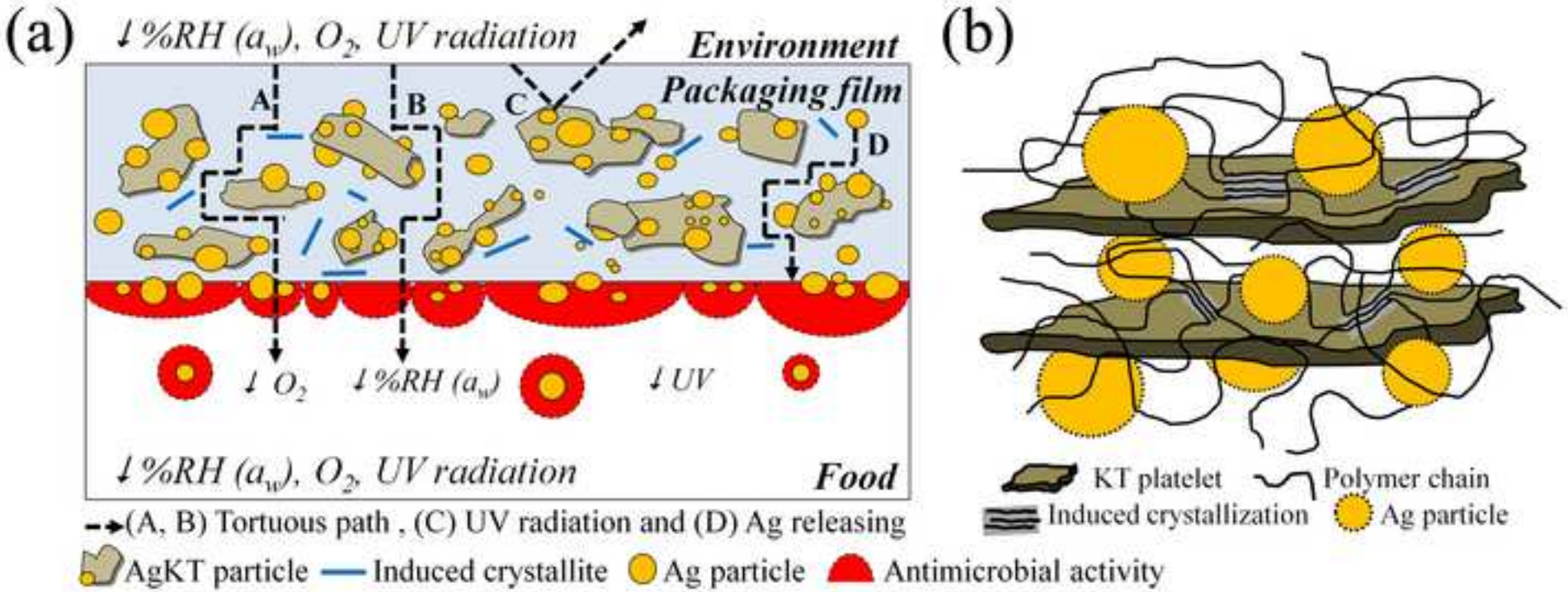

Figure 10

Click here to download high resolution image

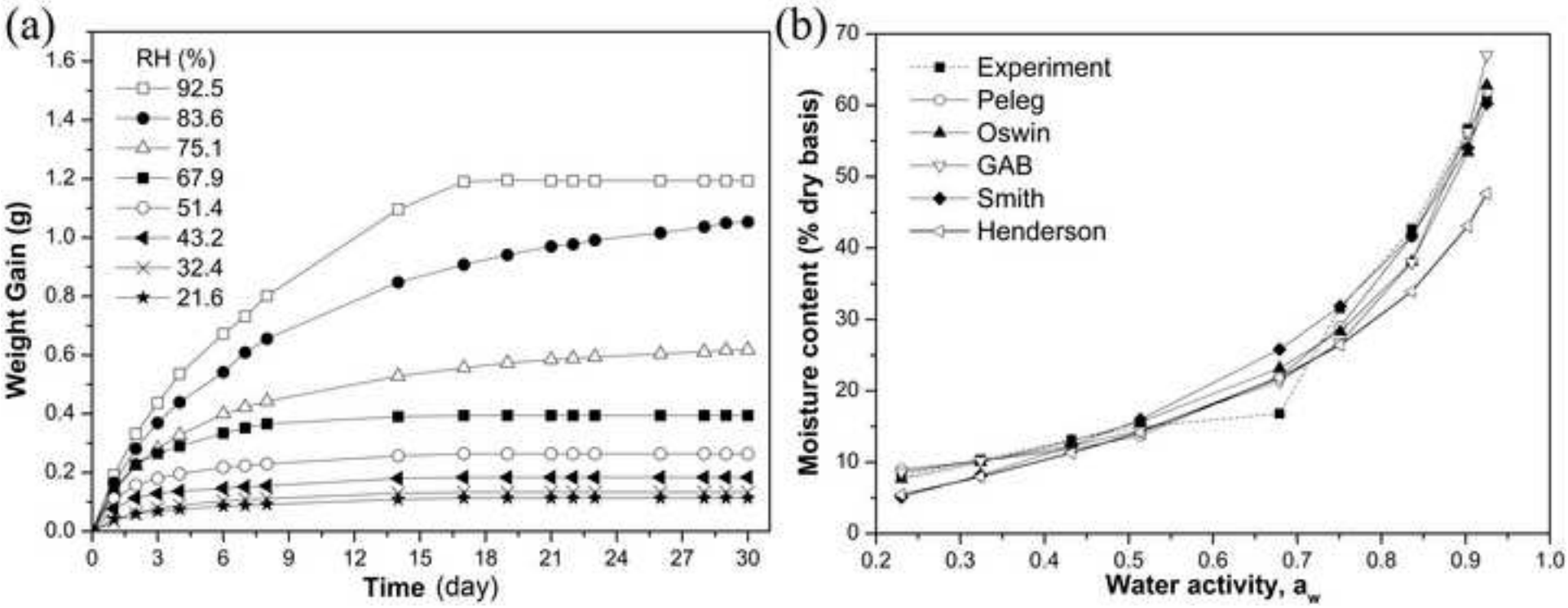

Supplementary Material (online publication)

Click here to download Supplementary Material (online publication): Sutinee et. al. (Supplementary data).docx

Table 1

Table 1 Mechanical properties of neat PLA, neat PBAT, PLA/PBAT blend, PLA/PBAT/TBT compatibilized blend and PLA/PBAT/TBT/AgKT nanocomposite films in MD and TD.

Film	Machine direction (MD)			Transverse direction (TD)		
	Tensile strength (MPa)	Elongation at break (%)	Young's modulus (MPa)	Tensile strength (MPa)	Elongation at break (%)	Young's modulus (MPa)
Neat PLA	149.87 ± 1.18	26.48 ± 11.94	2210.30 ± 71.28	51.35 ± 2.40	6.51 ± 5.79	2231.59 ± 152.27
Neat PBAT	8.41 ± 1.34	904.71 ± 2.34	90.44 ± 3.67	10.33 ± 3.40	859.70 ± 4.47	102.21 ± 3.37
PLA/PBAT	7.48 ± 0.53	34.59 ± 11.27	1206.03 ± 150.41	22.24 ± 2.84	7.57 ± 0.45	1220.47 ± 121.78
PLA/PBAT/TBT	30.05 ± 0.70	224.10 ± 2.43	1444.60 ± 6.75	35.02 ± 2.01	20.85 ± 3.16	1589.44 ± 92.44
PLA/PBAT/TBT/AgKT	35.29 ± 2.33	176.22 ± 20.11	1420.90 ± 79.62	40.33 ± 5.94	8.75 ± 0.45	1992.53 ± 73.28

Table 2

Table 2 Thermal properties of neat PLA, neat PBAT, PLA/PBAT blend, PLA/PBAT/TBT compatibilized blend and PLA/PBAT/TBT/AgKT nanocomposite films characterized by different techniques**.**

Film	DSC					DMA		TGA
	T_g (ºC)	T_c (ºC)	$\triangle H_c$ (J g^{-1})	T_m (ºC)	$\triangle H_m$ (J g^{-1})	Tan δ (peak) (ºC)	E' at 30 ºC (MPa)	T_d range (ºC)
Neat PLA	54.9	-	-	149.3	2.1	74.2	3183.49	316.0 - 402.3
Neat PBAT	n/d	-	-	110.8	11.3	-15.0	100.28	307.4 - 527.3
PLA/PBAT	59.9	117.8	13.4	150.7	19.4	-14.7, 72.1	1774.53	277.3 - 504.2
PLA/PBAT/TBT	54.8	112.8	15.4	148.3	19.9	-14.8, 70.5	2034.31	295.8 - 521.6
PLA/PBAT/TBT/AgKT	54.4	112.5	16.3	148.7	21.3	-15.9, 69.8	2115.52	311.0 - 540.1

Table 3 Barrier properties and contact angle of neat PLA, neat PBAT, PLA/PBAT blend, PLA/PBAT/TBT compatibilized blend and PLA/PBAT/TBT/AgKT nanocomposite films**.**

Film	**WVP** ($g\ m^2\ day^{-1}\ mmHg^{-1}$)	**OP** ($cm^3\ m^{-2}\ day^{-1}$)	**%T of UV light (at 400 nm)**	**Contact angle (º)**
Neat PLA	4.85 ± 0.64	461.72 ± 7.11	89.23 ± 0.27	73.36 ± 1.65
Neat PBAT	10.02 ± 0.30	535.70 ± 0.00	5.79 ± 2.33	48.47 ± 0.95
PLA/PBAT	2.74 ± 0.20	600.00 ± 150.00	25.33 ± 4.22	90.00 ± 20.00
PLA/PBAT/TBT	3.21 ± 0.04	431.53 ± 3.00	29.82 ± 3.89	66.94 ± 3.39
PLA/PBAT/TBT/AgKT	1.22 ± 0.04	369.35 ± 5.59	20.94 ± 1.66	85.42 ± 0.43

Table 4

Table 4 Sorption isotherm models used herein [24] with relevant calculated constant parameters, coefficient of determination and percentage of root mean square error for dried longan.

Sorption isotherm model	Mathematical expression [24]	Constant parameter	r^2	%RMS
B.E.T.	$MC = \frac{M_o C a_w}{(1-a_w)(1+(C-1)a_w)}$	M_o = 7.8864 C = 15.0952	0.9380	16.87
Oswin	$MC = C(\frac{a_w}{1-a_w})^n$	C = 15.1576 n = 0.5658	0.9743	3.14
Smith	$MC = C_1 + C_2 \ln(1-a_w)$	C_1 = -1.1101 C_2 = -23.6860	0.9684	3.43
Halsey	$MC = (-\frac{C}{\ln a_w})^{\frac{1}{n}}$	C = 15.6923 n = 0.7042	0.8707	8.38
Henderson	$MC = (-\frac{\ln(1-a_w)}{C})^{\frac{1}{n}}$	C = 0.0436 n = 1.1057	0.9650	7.47
G.A.B.	$MC = \frac{M_o C K a_w}{(1-Ka_w)(1-Ka_w+CKa_w)}$	M_o = 7.6002 K = 0.9591 C = 26.3808	0.9704	3.46
Peleg	$MC = C_1 a_w^{c_3} + C_2 a_w^{c_4}$	C_1 = 14.3246 C_2 = 0.3192 C_3 = 72.4413 C_4 = 5.2939	0.9877	2.14

MC = equilibrium moisture content, M_0 = monolayer moisture content, a_w = water activity and C, n, C_1, C_2, C_3, C_4, K = constants specific to individual mathematical expression.

Table 5

Table 5 Comparison of experimental and predicted dried longan shelf lives (using Peleg model) of the compatibilized blend and nanocomposite films compared with OPP film.

Shelf life (day)	**PLA/PBAT/TBT film**	**PLA/PBAT/TBT/AgKT film**	**OPP film**
Experiment	117.16	308.27	390.55
Peleg model	117.13	308.20	396.17

WVP of OPP film is ~1.07 $g \cdot m^2 \cdot day^{-1} \cdot mmHg^{-1}$.